Reaction Chemistry & Engineering
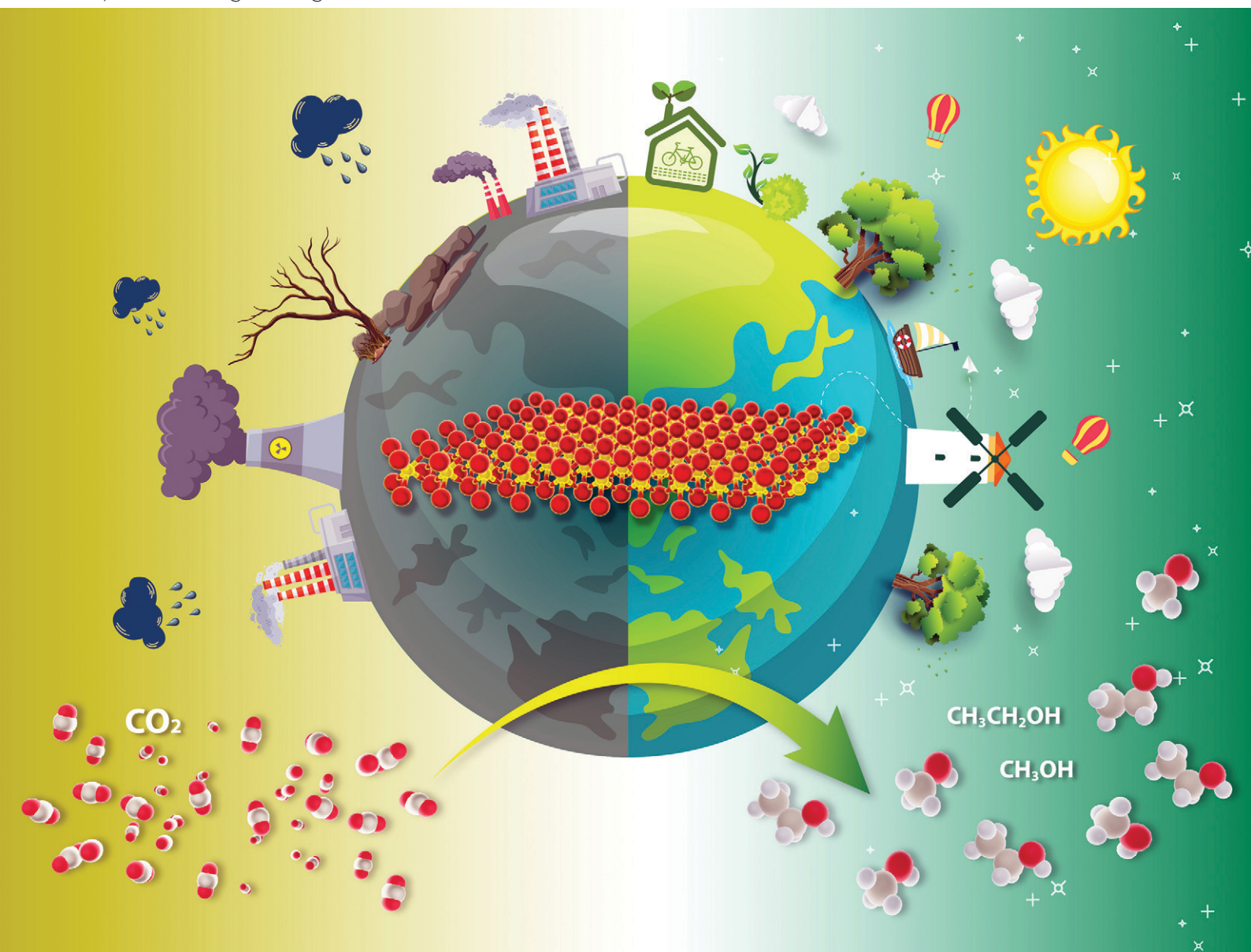
Linking fundamental chemistry and engineering to create scalable, efficient processes

rsc.li/reaction-engineering

ROYAL SOCIETY
OF **CHEMISTRY**

REVIEW ARTICLE
Suresh C. Pillai *et al.*
Impact of structure, doping and defect-engineering
in 2D materials on CO_2 capture and conversion

Check for updates

Impact of structure, doping and defect-engineering in 2D materials on CO_2 capture and conversion

E. J. Jelmy,[a] Nishanth Thomas, (iD)[bc] Dhanu Treasa Mathew,[a] Jesna Louis,[ad] Nisha T. Padmanabhan,[a] Vignesh Kumaravel,[bc] Honey John[ad] and Suresh C. Pillai (iD)*[bc]

The investigations on anthropogenic carbon dioxide (CO_2) capture and conversion play a vital role in eradicating global warming and the energy crisis. In this context, defect-engineered two-dimensional (2D) nanomaterials have received much attention in recent years. Herein, the significance of 2D nanomaterials such as graphene, transition metal dichalcogenides, hexagonal boron nitride, MXenes, graphitic carbon nitride, metal/covalent organic frameworks, nanoclays, borophenes, graphynes and green phosphorenes for CO_2 capture and conversion has been emphasized. Further, the intrinsic mechanism of CO_2 adsorption and conversion is discussed in detail. Theoretical and experimental studies among 2D materials highlight that N-doped porous adsorbents based on graphene and MXenes are more suitable for CO_2 adsorption applications. Also, more emphasis is given to outlining and discussing the role of various 2D nanomaterials and their hybrids as photocatalysts, electrocatalysts, photoelectrocatalysts, and thermocatalysts to transform CO_2 into valuable products. Although immense efforts are deployed in developing 2D catalysts for the conversion of CO_2, challenges such as agglomeration, poor yield, difficulties in analysing the 2D structures for catalytic factors, poor knowledge and in-depth understanding of the reaction mechanisms, high cost, *etc.* limit their large scale production and commercialization. More detailed theoretical and experimental investigations are required to develop 2D nanostructures with optimum properties for large-scale capture and conversion of CO_2.

1. Introduction

Carbon dioxide (CO_2) is a significant integrant, which accounts for around 65% of total greenhouse gas emissions. The major impacts of global warming due to CO_2 emissions include rising sea levels, ozone layer depletion, dip in water supplies, acidification of the ocean, infectious diseases, unpredictable weather conditions, *etc.* In this context, carbon capture and storage (CCS) and carbon capture and utilisation (CCU) effectively abate CO_2 emissions.[1–4] In general, CCS includes various physical and chemical methods and sequestration procedures and so it is implemented *via* different stages such as CO_2 capture, transportation and storage. The standard techniques to capture CO_2 include pre-combustion, oxy-fuel combustion and post-combustion. The captured CO_2 is compressed, transported and stored into geological reservoirs. In capture processes, the capture and separation of CO_2 is carried out through the adsorption using solvents, solid sorbents, pressure/vacuum swing, membrane and cryogenic separation, and chemical looping combustion technologies. In general, CCU includes: 1) direct utilisation of CO_2 in the food and packaging industries as a carbonating, packaging and preservative material, 2) direct utilisation of CO_2 in enhanced oil and coal-bed methane recovery, 3) conversion of CO_2 into chemicals and fuels where CO_2 could be used as a building block for the production of value-added products, 4) mineral carbonation, and 5) utilization of CO_2 for the cultivation of microalgae for biofuel production[5] (Fig. 1).

In general, capture technologies are based on aqueous amine sorbents requiring a high regeneration cost and therefore the capture of CO_2 *via* adsorption using solid adsorbents is preferred.[3] The adequate adsorption energy, easy CO_2 capture/release process, high selectivity, good thermal and mechanical stability and reusability are the essential criteria for a promising adsorbent. Based on this, several types of

[a] *Department of Polymer Science and Rubber Technology, Cochin University of Science and Technology, Kerala, India*

[b] *Nanotechnology and Bio-engineering Research Group, Department of Environmental Science, Institute of Technology Sligo, Sligo, Ireland. E-mail: pillai.suresh@itsligo.ie*

[c] *Centre for Precision Engineering, Materials and Manufacturing Research (PEM), Institute of Technology Sligo, Sligo, Ireland*

[d] *Inter University Centre for Nanomaterials and Devices, Cochin University of Science and Technology, Kerala, India*
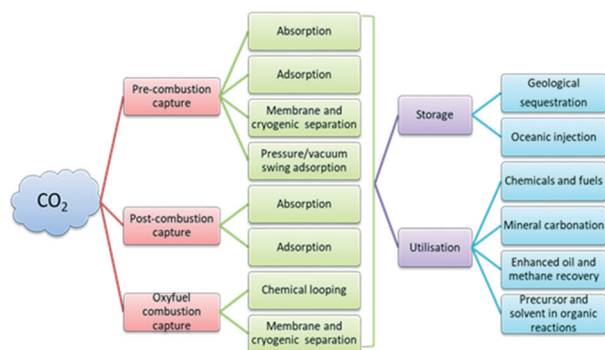
Fig. 1 Schematic of the technologies available for CCS and CCU.

carbonaceous and non-carbonaceous materials such as carbon nanotubes, graphene, activated charcoals, polymeric materials, aerogels, zeolites, metal organic frameworks (MOFs), *etc.* have been proposed to capture CO_2.

The catalytic conversion of CO_2 to valuable products such as methane, carbon monoxide, acetic acid, formic acid, methanol, ethanol, *etc.* is an efficient tool for the effective utilization of the stored CO_2. However, the major hindrance in the conversion of CO_2 to valuable chemicals lies in its thermodynamic inertness and associated high C=O bond dissociation energy (750 kJ mol^{-1}) which is higher than that of C–O, C–C and C–H bonds. The demand for an excessive negative redox potential (E^o_{redox} = −1.90 eV *vs.* NHE) for the electron transfer in CO_2 to deliver active species makes

Jelmy E. J. obtained her Ph.D. in Chemistry from Amrita Vishwa Vidyapeetham University, India, in 2016. She completed her post-graduation in Applied Chemistry at Calicut University, Kerala. Since June 2018, she has worked at Cochin University of Science and Technology as a Post-Doctoral Fellow. Her research interests are in the development of conducting polymer-based nanocomposites for energy and environmental applications. She is currently pursuing her research specifically on supercapacitors, triboelectric nanogenerators, and adsorption of pollutant dyes & CO_2 gas using graphene/conducting polymer aerogels.

E. J. Jelmy

Nishanth Thomas is a Ph.D. candidate in the Nanotechnology and Bio-Engineering Research Group at the Institute of Technology Sligo, Ireland. He completed his BSMS dual degree in Chemistry (major) with a minor in Biology at the Indian Institute of Science Education and Research (IISER) Bhopal, India. During his master's thesis, he investigated the shape-selective synthesis of silver nanostructures by a modified polyol method. Currently, he is working in the EU-Horizon 2020 PANI-WATER Research project for developing Advanced Oxidation Processes (AOPs) for the removal of contaminants of emerging concern (CECs) and antimicrobial-resistant bacteria (ARB) from water. His research interest involves the design of unique nanomaterials for sustainable environment and energy applications.

Nishanth Thomas

Dhanu Treasa Mathew received her Master of Science in Pure Chemistry in 2016 and is currently a Ph.D. scholar in the Department of Polymer Science and Rubber Technology at Cochin University of Science and Technology (CUSAT). Her research interests are focused on the fabrication and development of triboelectric nanogenerators based on eco-friendly materials.

Dhanu Treasa Mathew

Jesna Louis is a fourth year PhD student in the Department of Polymer Science and Rubber Technology, Cochin University of Science and Technology, India. Her research interests center around the opto-electronic application of semiconductor oxides and their organic/inorganic hybrids. She received her bachelor's degree and master's degree in Chemistry from the Indian Institute of Science Education and Research (Bhopal, India).

Jesna Louis

photocatalytic, electrocatalytic and photoelectrocatalytic conversion tough. On the other hand, thermocatalytic CO_2 conversions are carried out at a high temperature and pressure with the catalytic support from alkali and alkaline earth metal-based oxides and hydroxides in order to overcome the thermodynamic stability and inertness of CO_2.[6]

Nisha T. Padmanabhan joined Cochin University of Science and Technology, Kerala, in 2016, for her doctoral studies. Presently as a CSIR-SRF, she is focused on the synthesis of hybrids based on high-energy faceted TiO_2 with transition metal dichalcogenides and other graphitic monolayers for various sustainable & energy applications including self-cleaning, superhydrophilicity, hydrogen evolution reactions, etc. She pursued her post-graduation in chemistry at Mahatma Gandhi University, Kerala.

Nisha T. Padmanabhan

Vignesh Kumaravel obtained his PhD in Chemistry from Madurai Kamaraj University, India in 2013. He has established various research laboratories for doctoral students in energy research. Since March 2018, Vignesh has worked at IT Sligo as a Senior Research Fellow in the EU funded Renewable Engine project. His primary research goals are directed towards the development of nanoparticles for carbon dioxide conversion, water treatment, hydrogen production, antimicrobial food packaging polymers/bio-medical implants, high-temperature stable energy storage devices, super-hydrophobic surfaces, etc. He has completed various research projects as a co-PI/PI, sponsored by Malaysian funding agencies. He is acting as an external examiner for Ph.D thesis evaluation in various Indian universities. He is also acting as a reviewer in evaluating research proposals from the government of Chile (Chilean National Science and Technology Commission) and Poland (National Science Centre). As an expert in the field of materials science, he has peer-reviewed more than 50 research papers in various publications such as Elsevier, ACS, Wiley and Springer Journals. He is currently acting as a guest editor in Catalysts, MDPI journals.

Vignesh Kumaravel

Honey John obtained her Ph.D. from Cochin University of Science and Technology (Kerala, India) in 2004. She joined the Indian Institute of Space Science and Technology (IIST), Trivandrum, in 2007, as a Reader and worked to the grade of Associate Professor. In 2015, she rejoined the Department of PS&RT, CUSAT as a professor. In 2017, she became the honorary Director of Inter University Centre for Nanomaterials and Devices, CUSAT. Her current research areas are triboelectric and piezoelectric nanogenerators, 2D nanoscrolls with magnetic nanoparticles, photocatalytic self-cleaning materials, hydrogen production, aerogels for supercapacitors and pollutant removal, magnetoplasmonics and green tyres.

Honey John

Suresh C. Pillai obtained his Ph. D. from Trinity College Dublin and completed his postdoctoral research at California Institute of Technology (Caltech, USA). He is an elected fellow of the UK's Royal Microscopical Society (FRMS) and the Institute of Materials, Minerals and Mining (FIMMM). He also completed an executive MBA at Dublin City University, in 2009. He joined IT Sligo in 2013 as a Senior Lecturer and currently heads the Nanotechnology and Bio-Engineering Research Group. His research interests include the synthesis of nanomaterials for energy and environmental applications. He is the recipient of several awards including the Boyle-Higgins Award 2019, the Industrial Technologies Award 2011, Hothouse Commercialisation Award 2009, Enterprise Ireland Research Commercialization Award 2009, etc. He is an associate editor for the Chemical Engineering Journal and an editorial board member for Applied Catalysis B.

Suresh C. Pillai

This journal is © The Royal Society of Chemistry 2021

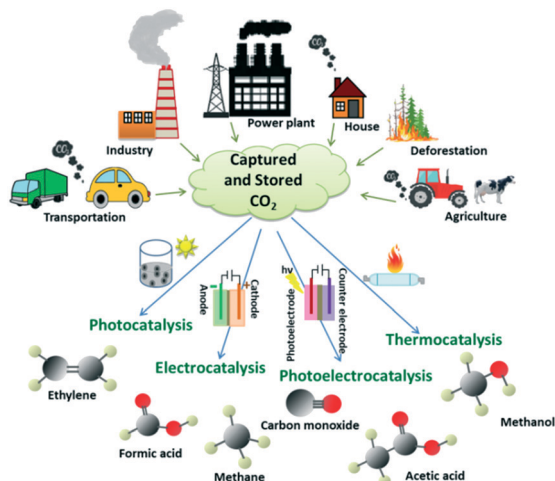*React. Chem. Eng.*, 2021, **6**, 1701–1738 | **1703**

Fig. 2 Different sources of CO_2 emission and the utilisation of captured/stored CO_2 by catalytic conversion to value-added products.

Different sources of CO_2 emission and its effective utilization by various techniques are depicted in Fig. 2.

After the discovery of graphene, the research on 2D nanomaterials has proliferated, and a wide range of materials such as transition metal dichalcogenides (TMDCs), hexagonal boron nitride (h-BN), MXenes, graphitic carbon nitrides (g-C_3N_4), metal/covalent organic frameworks (COFs and MOFs), borophenes, graphynes, green phosphorenes, *etc.*

have been studied. Further, due to the quantum confinement effect in few-layered systems, one can observe exponentially high electronic, optical and mechanical properties when compared to their bulk counterparts. Also, the presence of enduring excitons and trions developed due to the augmented coulombic interactions between charge carriers in semiconducting 2D nanomaterials makes them a prodigious candidate in various disciplines. Further, the enhanced surface area with tuneable physical and chemical properties of 2D materials makes them promising in catalysis, energy storage and optoelectronic applications.[7–10] Few-layered 2D nanosheets with unveiled surface atoms have a tendency to escape from the lattice to form defects which in turn can enhance the catalytic performance due to the reduction in the coordination number of the surface atoms. Therefore, the defect engineering of these materials plays a significant role in improving the catalytic performances.[11] Due to the aforementioned reasons, the research on catalytic conversion and adsorption of CO_2 by 2D materials is considerable.

Several reviews on CO_2 capture & storage[1–5,12–16] and its catalytic conversion into valuable products[17–21] have been published with a prime focus on the technologies. For instance, the recent developments in the use of physisorbents such as carbon nanotubes, graphene, zeolites, silica materials, and MOFs for the removal of CO_2 have been addressed.[3] Recently the significance of nanomaterials such

Table 1 Comparison of CO_2 adsorption capacities of 2D materials and traditional solid adsorbents

| Type of adsorbent | Materials used | Operating conditions | | Adsorption capacity (mmol g^{-1}) | Ref. |
		Pressure (bar)	Temperature (°C)		
2D adsorbents (pristine/doped/defected)	Graphene	11	25	21.6	26
	rGO/N-doped porous carbon composite	5	25	5.77	27
	Fe_3O_4/graphene	11	25	60	28
	PANI/GO	20	27	3.2	29
	PPy/rGO	1	0	6.8	30
	Porous BN	1–20	25	1.68.3	31
	C doped BN	1	0	~5.5	32
	MXene, M_2N	1	727	7.96	33
	$Ti_3C_2T_x$	4	25	5.79	34
	g-C_3N_4 nanosheets functionalized with ionic liquid	15	25	42.93	35
	Octadecylamine modified MMT	50	25	7.16	36
Zeolites	Core–shell zeolite-5A@MOF-74	20	25	13.8	37
	Zeolite NaX	1	25	7.04	38
	Li-LSX zeolite	1	60	4.43	39
	Zeolite SSZ-13	1	25	3.98	40
Activated charcoal	Activated carbon derived from nanocellulose	1	0	5.52	41
	N-Doped activated carbon	1	0	5.12	42
	Catalytically activated carbon	1	0	4.36	43
	Physically activated carbon	1	25	3.52	44
	Activated carbon derived from biomass	1	50	1.1	45
MOFs	Amine-functionalized vanadium-based MOF	1	25	1.9	46
	$Cu_3(NH_2BTC)_2$ MOF	0.1	50	1.41	47
	Aluminum trimesate-based MOF	10	25	10.22	48
	In(III)/Pd(II)-Based MOF	1	0	4.1	49
	MOF/GO composite	1	0	6.8	50
Silica	APTES functionalized SBA-15 silica	1	30	1.2	51
	Silica xerogel	7.5	25	1.8	52
	Amine-grafted mesocellular silica foams	1	60	1.54	53

1704 | *React. Chem. Eng.*, 2021, **6**, 1701–1738

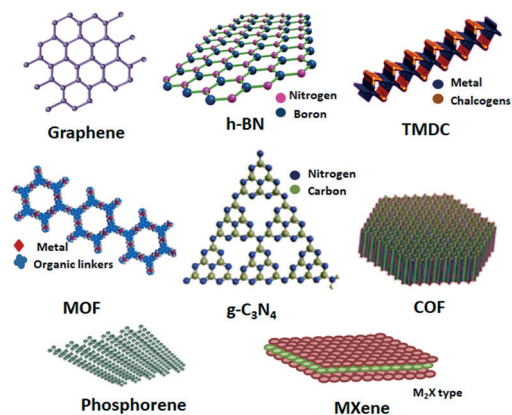This journal is © The Royal Society of Chemistry 2021

Fig. 3 Structures of common 2D materials used for CO_2 adsorption and conversion.

as MOFs, COFs, zeolites, silicon-based materials, porous organic polymers, layered double hydroxide (LDH)-based materials, metal oxides and nanocarbon materials for the adsorption of CO_2 has been reported.[1] Further, an analysis on the engineering aspects of MOFs for enhanced CO_2 capture and conversion has been reported recently.[22] A comparison of CO_2 adsorption capacities of 2D materials with traditional solid adsorbents is given in Table 1. Apart from the CO_2 adsorption analyses, a recent study highlighted the defect engineering, surface modification and hybrid construction strategies to modify 2D nanomaterials for enhanced photocatalytic reduction of CO_2.[17] The structural, electronic, thermodynamic and reactive properties of 2D photoelectrocatalysts were examined by Torrisi *et al.* The major outputs of the study include the investigations on the monolayer phases of selected bulk catalysts and the unconventional chemical behaviour of these materials in CO_2 reduction.[23] It is reported that there are lot of challenges involved in the electrochemical reduction of CO_2 using 2D nanomaterials and the exploration of quantum dots or metal modified porous carbon sheets, heterostructured 2D materials, and inexpensive non-noble 2D metals as electrocatalysts is essential for the future continuation of research in this field.[11] In another study, catalytic conversion of CO_2 using heteroatom-doped carbon materials has been addressed.[24] A comprehensive study on photoelectrochemical
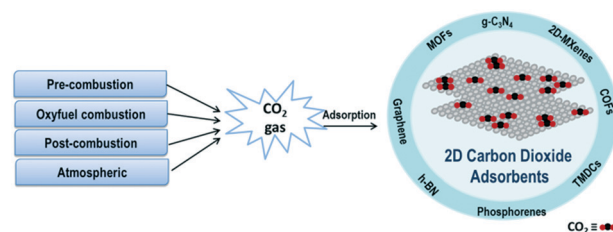

Fig. 4 Schematic of various CO_2 capture processes.

Fig. 5 Schematic of the applications of 2D materials for CO_2 adsorption.

conversion of CO_2 to value-added products was recently reported with special emphasis on the materials for the electrode, mechanisms, and reactor design.[25] Nevertheless, there are no comprehensive reports on the utility of 2D nanomaterials for both CO_2 adsorption and conversion by various techniques. Herein, the recent progress and the prominence of 2D materials for CO_2 capture, photocatalysis, electrocatalysis, photoelectrocatalysis, and thermocatalysis have been summarized. This article starts with an overview of different techniques for CO_2 capture and it is followed by a detailed study of recently suggested 2D nanomaterials and their hybrids such as graphene, TMDCs, h-BN, MXenes, MOFs, COFs, g-C_3N_4, nanoclays, borophenes, graphynes, green phosphorene, *etc.* in CO_2 adsorption/conversion applications. The structures of common 2D materials used for adsorption and conversion of CO_2 are given in Fig. 3.

2. Fundamentals of carbon dioxide capture

The technologies behind CCS in power plants include pre-combustion capture, oxy-fuel combustion capture and post-combustion capture.[2,3,5,15] In pre-combustion capture, as the name indicates, CO_2 is captured and stored before the combustion process of the fossil fuel. It can also be defined as a decarbonisation procedure of traditional fuels such as natural gas or coal before producing energy out of them. The two major events involved in this technology are the formation of synthesis gas (syngas) and steam reforming reactions. In this process, the reaction of the fuel with air or O_2 leads to the formation of syngas comprising CO and H_2.[54] The purified syngas undergoes a water-gas shift reaction (WGSR) where CO is treated with steam to produce CO_2 and H_2. Also, the steam reforming stage delivers H_2 (43%), H_2O (21%), CO (11%) and CO_2 (6%) as major products.[55] By physical or chemical absorption, adsorption or separation methods, CO_2 is captured and stored for its effective utilisation. In general, the high-pressure CO_2 produced in the pre-combustion technique is compressed and liquefied for storage, transportation, and future use. The H_2 from the steam reforming process can be purified for use in fuel cells or it can be used to produce valuable chemicals. In the oxy-fuel combustion process, the fuel is combusted with pure oxygen to produce flue gas rich in CO_2. The main drawback with this process is the requirement of pure oxygen in massive amounts, which abates its commercialization efforts. Except for this
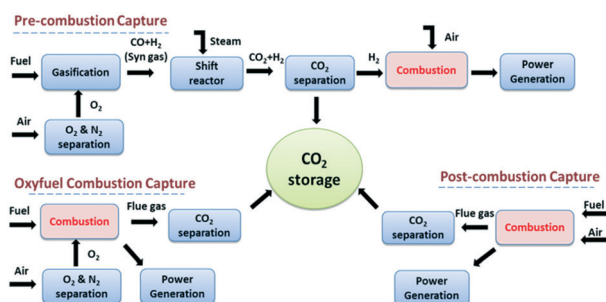
This journal is © The Royal Society of Chemistry 2021

React. Chem. Eng., 2021, **6**, 1701–1738 | **1705**

problem, the oxy-fuel combustion process is an attractive one with easy CO_2 separation, reducing the volume of flue gas and NO_x gases with minimal efficacy penalty.[14,56] Researchers speculated that it would be the best available CO_2-free power generation method once it got commercialized.[56] In post-combustion capture, CO_2 is separated or removed from the flue gas after fuel combustion. The exhaust flue gas is purified before the capture of CO_2 to remove the traces of nitrogen, sulphur, and dust. Out of the different technologies described above, post-combustion carbon dioxide capture is the most significant, especially in power plants since the capture unit can be added to the plant even after constructing the power plant.[57] Fig. 4 represents the different CO_2 capture processes.

Amine-based chemical solvents are used as absorbents to separate H_2 and CO_2 formed in the pre-combustion and post-combustion processes because of their high CO_2 absorption capacity. However, chemical or physical solvents are not encouraged because of their high viscosity, toxicity, flammability, corrosiveness, extensive energy demand especially in the regeneration stage and low H_2–CO_2 selectivity.[2,5,57,58] On the other hand, CO_2 uptake using solid adsorbents such as zeolites,[59] activated carbons,[60,61] and MOFs[62] is attractive due to their high CO_2 adsorption efficiency, selectivity, low energy requirements, easy recovery and stability.[3,63] The curtailed adsorption efficiency of MOFs and activated carbons at elevated temperature is a major issue with the pre-combustion process.[2] Therefore CO_2 adsorbents based on lithium silicate nanosheets[63] and Nd-doped lithium silicate[64] were introduced as adsorbents.

The techniques for CO_2 adsorption using solid materials include pressure swing adsorption (PSA), vacuum swing adsorption (VSA), temperature swing adsorption (TSA), moisture swing adsorption (MSA), electric swing adsorption (ESA) and temperature vacuum pressure swing adsorption (TVPSA) and out of these, the most commonly used techniques are PSA, VSA and TSA.[3] In the PSA technique, pressure higher than 1 bar is used, while in VSA, pressure lower than 1 bar is used and the regeneration of the adsorbent is done by reducing the pressure.[12] In TSA, the
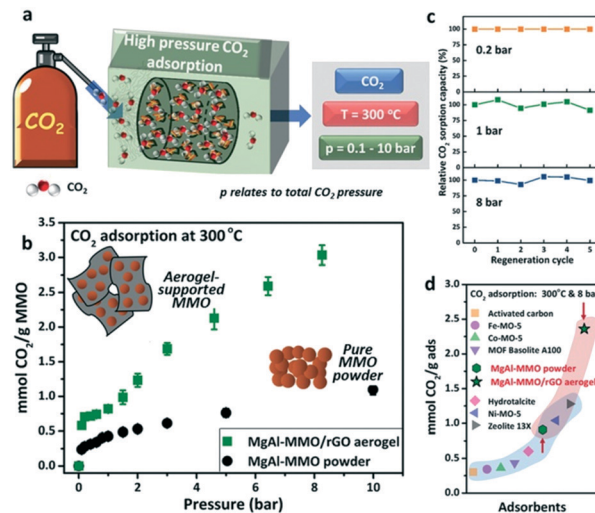
Fig. 7 CO_2 adsorption by MgAl-MMO/rGO aerogels at high pressure and temperature (a); CO_2 adsorption isotherms in a pressure range of 0.2 to 10 bar (b); relative CO_2 adsorption capacities at 0.2, 1, and 8 bar CO_2 pressure (c); comparison of sorption capacities with other reports (d). "Reproduced from ref. 108 with permission from Wiley-VCH, copyright 2020".

adsorbent bed is heated to elevate the adsorption temperature and then cooled for desorption. In general, for the separation of CO_2 from the flue gas, VSA is considered more efficient than PSA because applying pressure to the large area feed is economically not viable.[12] Usually, in CO_2 capture by the adsorption process, a spherical column is packed with the adsorbent and CO_2 containing gas is passed through the column.[1] During the adsorption process, when gas molecules are in the close vicinity of the adsorbent, they got attracted to the electronic environment of the adsorbent surface. The gas molecule–solid surface interaction can result in the reduction of the free energy of the surface, and therefore, more and more gas molecules can be accumulated on the solid surface before adsorption.[3] The adsorption process can be physical or chemical depending on the type of interaction between the adsorbent and adsorbate. Due to the absence of chemical bond formation in physical adsorption, the energy penalty for the regeneration of CO_2 is more diminutive. In physical adsorption, along with the van der Waals attraction of CO_2 and the adsorbent, electric quadrupole moment (EQM)-electric field gradient interactions are also taking place. The value of EQM is the main factor deciding the selectivity of gases and therefore, carbon dioxide molecules with a high EQM value can be adsorbed on the solid surface compared to nitrogen molecules.[3] The necessary criteria to be satisfied by the material for an economical and operational implementation of CO_2 capture include a significant CO_2 adsorption capacity ($\sim$3–4 mmol g^{-1}), high CO_2 selectivity, fast adsorption/desorption kinetics, adequate mechanical strength, low heat of adsorption, and low cost. Nanomaterials are promising candidates for the adsorption and catalysis of CO_2 because of their large surface-to-volume ratio and the presence of a

Fig. 6 Schematic of the synthesis of the N-doped porous rGO composite for CO_2 adsorption and supercapacitor applications. "Reproduced from ref. 27 with permission from Elsevier, copyright 2021".

1706 | *React. Chem. Eng.*, 2021, **6**, 1701–1738

This journal is © The Royal Society of Chemistry 2021

considerable number of reactive sites. Besides, the affinity of nanomaterials towards the target molecules can be enhanced by surface modification,[65,66] making them interesting for CO_2 capture and conversion applications.

3. Two-dimensional nanomaterials for CO_2 adsorption

Recently, 2D materials such as graphene (or reduced graphene oxide (rGO)),[67–72] molybdenum disulphide (MoS_2),[73–76] h-BN,[77–81] MXenes,[33,82] 2D MOFs & COFs,[8,21,83,84] g-C_3N_4,[85] phosphorenes, nanoclays, *etc.* (Fig. 5) have been used as adsorbents for CO_2 capture.[86]

3.1 Graphene

Graphene is an excellent 2D material with unique features such as zero bandgap energy, transparency (97.7%),[87] high concentration of charges (10^{13} cm^{-2}),[88] charge mobility,[89] current density (1.18×10^8 A cm^{-2}),[90] mechanical strength (0.2 TPa)[91] and thermal conductivity ($\sim$5000 W mK^{-1}).[92] The common problem in TSA/VSA/PSA processes for CO_2 capture is the temperature instability of the adsorbent, especially in TSA mode. Mechanical disintegration of the adsorbent due to the tight packing of the adsorbent column and the subsequent reduction in the surface area of the adsorbent is an associated concern. Because of the excellent mechanical strength, thermal conductivity and stability of graphene, the compact packing of the adsorbent column is stable even after repeated or cyclic processes.[93] This makes graphene-based materials a wonderful candidate to substitute for traditional adsorbents. The main factors deciding the gas adsorption efficiency of graphene are its ultra-microporous structure, availability of active sites, high specific surface area, and the presence of functional groups for better interaction between the adsorbate and adsorbent. The gas adsorption capacities of pristine graphene oxide (GO) or reduced graphene oxide (rGO) can be further improved by various physical[94] or chemical activation processes[95–97] in which the porosity of the material can be tuned for CO_2 capture. Therefore, top-down and bottom-up techniques such as the use of electron beams, nanosphere lithography, barrier-guided chemical vapour deposition, catalytic hydrogenation, photocatalytic oxidation, chemical etching, *etc.* can be employed to produce and control the lattice[98] of graphene to improve CO_2 adsorption capacities. Similarly, the removal or introduction of defects in the lattice of graphene can cause an enhancement in CO_2 adsorption capacity[93] by creating pores with suitable radii to accommodate CO_2 gas molecules. In another study, CO_2 adsorption states on monolayer epitaxial graphene grown on a SiC (0001) substrate at 30 K were analysed by temperature-programmed desorption (TPD), X-ray photoelectron spectroscopy (XPS), and density functional theory (DFT).[71] In this, CO_2 gas was introduced onto the sample surface through a pulse gas dosing system. The coverage of CO_2 on graphene was determined by XPS

and TPD. The analysis showed a physisorption behaviour for CO_2 on graphene, confirming the previous results reported.[26,99] From the binding energies of CO_2 in C 1s and O 1s of XPS spectra, they have inferred that the adsorption and desorption of CO_2 on graphene is in the physisorption regime and the nature of interaction between CO_2 and graphene was studied by DFT calculations.[71] Recently, adsorption-induced clustering of CO_2 on graphene nanosheets was studied through computational analysis.[68] The results showed that above a particular amount of surface coverage, the CO_2 gas molecules that are selectively adsorbed tend to form clusters of different sizes with the possible formation of dimers or trimers. The reason for this cluster formation is the quadrupole–quadrupole interaction between CO_2 molecules and this was facilitated by the favourable alignment of atoms on different molecules with opposite partial charges.[68] To model graphene they have selected coronene ($C_{24}H_{12}$) and circumcircumcoronene ($C_{96}H_{24}$), and computational analyses were carried out by DFT (B3LYP-D/6-31+G*) and molecular dynamics (MD).

The gas adsorption properties of carbon-based adsorbents can be further improved by doping with heteroatoms such as nitrogen (N), sulphur (S) or boron (B) to enhance the molecular interactions with CO_2.[100–102] Later, the role of boron moieties in the CO_2 adsorption ability of borane modified rGO was examined *via* experimental and theoretical calculations.[103] Through FTIR analysis, the physisorption of CO_2 on boron doped rGO was evidenced and according to them, by introducing substitutional boron defects, the charge distribution can be altered to yield good selectivity to the nearest carbon, which is adjacent to the defected site. An adsorption capacity of 1.81 mmol g^{-1} was observed at 1 atm and 25 °C. Later, the dual doping of graphene with N and S and theoretical calculations using DFT and *ab initio* thermodynamics were carried out.[104] Superior CO_2 adsorption performance and better selectivity for CO_2 over N_2 were also predicted in their study. CO_2 adsorption in N-doped rGO blended with activated charcoal was examined in another work. The maximum adsorption capacity of 3.81 g g^{-1} at 7 bar and 75 °C was obtained for the combination of activated charcoal and N-doped rGO (50NRGO) in the ratio of 50 : 50, and the CO_2 adsorption capacity was directly correlated with the enhanced surface area (9916.88 m^2 g^{-1}) of the sample.[105] Recently, N-doped few-layer graphene/Pebax mixed matrix membranes (MMMs) were developed for CO_2 capture.[106] The role of N-doping on few-layer graphene in enhanced CO_2 capture, selectivity, diffusivity, solubility, and permeability was analysed through simulation studies and was well correlated with the experimental findings. In a study, a novel rGO/N-doped porous carbon (NPC) composite (surface area of 865 m^2 g^{-1}) was synthesized by a one-pot hydrothermal and KOH activation method with a CO_2 adsorption of 5.77 mmol g^{-1} at 298 K and 500 KPa. The CO_2 adsorption analysis without N-doping resulted in a reduced CO_2 adsorption of 2.07 mmol g^{-1}, and this shows the relevance of N atom doping in the graphene-based system.

This journal is © The Royal Society of Chemistry 2021

React. Chem. Eng., 2021, **6**, 1701–1738 | **1707**

CO_2 adsorption analysis reveals that the adsorption properties of the samples were increased with an increase in activation temperature up to 600 °C and a GO addition of 1%. The kinetic studies revealed that the isotherms were well fitted with the Redlich–Peterson isotherm model, indicating the chemical and physical adsorption of CO_2 in rGO/NPC samples.[27] Fig. 6 shows the schematic for the preparation of the rGO/N-porous composite for CO_2 adsorption and supercapacitor applications. In another work, the collective effects of the availability of pores with suitable size and the presence of functional groups (N, P, S, and O) on graphitic structures on the CO_2 adsorption behaviour were analysed using Grand Canonical Monte Carlo simulation (GCMC) and DFT.[107]

Aerogels are a new class of soft sponge-like materials with a large surface area, high porosity, and low density with excellent environmental applications. In general, graphene-based aerogels were prepared by the wet chemical method from graphene oxide (GO), which enables the formation of a 3D network in aqueous solutions through lyophilization, followed by reduction to form reduced graphene oxide aerogels with partially restored graphitic properties.[108] Metal nanoparticle incorporating hybrid graphene aerogels showed maximum performance in various applications. Recently, a novel mixed metal oxide (MMO)/rGO aerogel was studied for CO_2 at high pressure (8 bar) and high temperature (300 °C). A sorption capacity of 2.36 mmol g^{-1} was observed for MgAl MMO/rGO aerogels, whereas MgAl MMO powder showed a sorption capacity of 0.91 mmol g^{-1}.[108] Fig. 7 shows the CO_2 adsorption at high pressure and temperature of MgAl MMO/rGO aerogels. A novel graphene-based semi-coke-like porous and nitrogen-rich layered sandwich material was examined for CO_2 adsorption. The material with a surface area of 701.53 m^2 g^{-1} and 74% microporosity showed an adsorption capacity of 7.11 mmol g^{-1} at 30 bar and 298 K with probable physisorption of CO_2. A better CO_2/N_2 selectivity was observed because of the presence of N functionalities added into the system and N functionalities were introduced by the nucleophilic substitution of the semi-coke-like material with ethylenediamine (EDA).[109] A polyethylenimine modified GO (GEPM) sheet with high porosity, surface area and 3D structure was reported. The material showed a CO_2 adsorption capacity of around 11.2 wt% at 1.0 bar and 273 K, which was higher when compared to GO and hydrothermally reduced graphene (HTG). The high CO_2 adsorption capacity of GEPM was mainly due to the presence of basic sites since the effect of the surface area on the CO_2 adsorption was not correlated through their study. For instance, the BET surface area of GEPM, HTG, and GO was 476 m^2 g^{-1}, 876 m^2 g^{-1} and 31 m^2 g^{-1}, respectively, and the corresponding CO_2 uptake of these materials was 11 wt%, 8.1 wt% and 7.5 wt%. Even though HTG possesses a high surface area, the CO_2 adsorption capacity of HTG was comparable with GO. However, the CO_2 intake of GO was justified by the presence of oxygen-containing functional groups and surface heterogeneity associated with GO.[110] In another work,

heterostructures containing BN(OH)$_x$ nanosheets with B and N co-doped graphene aerogels (BN-GA) were proposed for CO_2 adsorption.[111] BN(OH)$_x$ nanosheets were added as a swelling agent and to prevent the restacking of GO during the solvothermal synthesis, whereas the doping with B and N imparts more adsorptive sites by destroying the electrical neutrality of C. BN-GAs with mesoporous structures and a surface area of 169.9 m^2 g^{-1} showed a CO_2 adsorption of 2.1–2.9 mmol g^{-1} at 273 K and 1.0 bar.

As discussed earlier, N doping of graphene can enhance the CO_2 adsorption due to the chemical interaction of CO_2 gas molecules with N doped adsorbents. Highly efficient traditional sorbents are only amine systems, and so the introduction of the conducting polymer polyaniline (PANI) to graphene is of interest because of the presence of primary and secondary amine moieties.[29,112]

The preliminary investigation on CO_2 adsorption using PANI/HEG (hydrogen exfoliated graphene) was reported by Mishra *et al.*, and they have achieved adsorption capacities of 75, 47 and 31 mmol g^{-1} at 11 bar pressure and at 25, 50 and 100 °C, respectively. The physical and chemical adsorptions of CO_2 were evidenced by FTIR spectroscopy. The PANI/HEG sorbent showed good cyclability; the capacity of the reused sorbents was only 2–3% lower than that of the fresh sorbent.[82] Later, physicochemical adsorption of CO_2 on the Fe$_3$O$_4$/HEG hybrid was reported by the same group.[28] Similar to their previous results, CO_2 adsorption capacities of 60, 35, and 24 mmol g^{-1} were observed at 11 bar pressure and at 25, 50, and 100 °C, respectively, and the physicochemical adsorption of CO_2 on the solid adsorbent was identified using FTIR spectra. Though the surface area of Fe$_3$O$_4$/HEG (98.2 m^2 g^{-1}) is lower when compared to that of HEG (443 m^2 g^{-1}), the enhanced CO_2 adsorption in Fe$_3$O$_4$/HEG was attributed to the chemical interaction between Fe$_3$O$_4$ and CO_2, as evidenced from FTIR analysis. Later, research on the CO_2 adsorption ability of graphene oxide (GO) hybridized
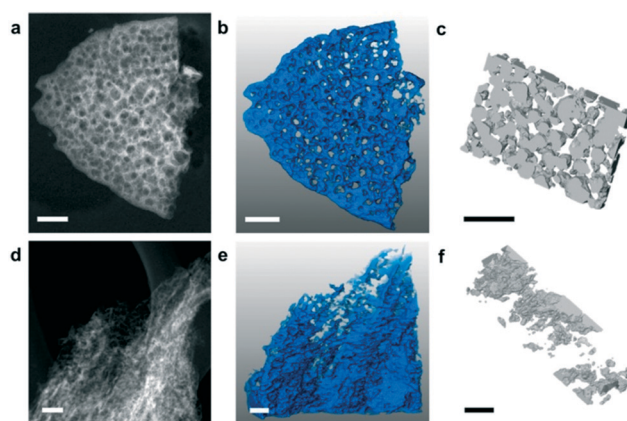

Fig. 8 STEM images of BN synthesized using urea (BN-U5) (a) and BN synthesized using urea and melamine (BN-MU1:5) (d); 3D tomography of BN-U5 (b) and BN-MU1:5 (e); 3D reconstruction of pores of BN-U5 (c) and BN-MU1:5 (f). "Reproduced from ref. 31 with permission from American Chemical Society, copyright 2017".

1708 | *React. Chem. Eng.*, 2021, **6**, 1701–1738

This journal is © The Royal Society of Chemistry 2021

with Fe_3O_4 and PANI was carried out and it showed an increment in adsorption capacity of GO from 0.25 mmol g^{-1} to 2.3 mmol g^{-1} by the incorporation of Fe_3O_4 and then to 3.2 mmol g^{-1} after the introduction of PANI to the binary system of Fe_3O_4 and GO. The improved CO_2 adsorption capacity of the ternary system is mainly attributed to the increased porosity and micropore volume of graphene oxide due to the functionalization with Fe_3O_4 and PANI. The low adsorption energy of the hybrid hints at the physisorption of CO_2 (ref. 29), while chemisorption of CO_2 on the adsorbent was not evidenced through their study. Similar to PANI, polypyrrole (PPy) was also introduced to graphene for CO_2 adsorption. N-Doped porous carbon obtained *via* chemical activation of PPy/graphene composites using potassium hydroxide solution is reported in a study. The chemical activation led to the N-doping of porous carbon in PPy, while the graphene units remain intact. PPy/graphene adsorbents with different weight percentages of GO were synthesised by *in situ* chemical polymerisation of pyrrole in the presence of GO using ammonium persulphate as an oxidant and the subsequent reduction of GO hybrids with hydrazine yielded PPy/graphene hybrids. The chemical activation using KOH solution was carried out at different temperatures (400, 500, 600, and 700 °C). The maximum CO_2 adsorption capacity of 4.3 mmol g^{-1} was observed for the adsorbents activated around 600 °C, and this is due to the formation of microporous structures with a pore size of 1.72 nm, which in turn can lead to a better adsorption and adsorbate–adsorbent interaction.[113] In a similar study, a chemically activated porous PPy/rGO was reported. Potassium citrate was used as an activation agent at 700 °C and the porous PPy/rGO material with a BET surface area of 1650 m^2 g^{-1} and 92% microporosity showed an adsorption capacity of 6.8 mmol g^{-1} at 0 °C and 760 mm Hg.[30]

3.2 Transition metal dichalcogenides

Transition metal dichalcogenides (TMDCs) are semiconductors of the type MX_2, where M is the transition metal atom such as Mo or W and X is a chalcogenide atom like S, Se or Te. TMDCs are a promising alternative to graphene because of their direct bandgap, robustness, and atomic level thickness with 2D characteristics.[114] Recently, various strategies are adopted for the synthesis of TMDs such as plasma-assisted synthesis,[115] mechanical exfoliation,[116] ion intercalation assisted liquid exfoliation,[117] wet chemical synthesis, chemical vapor deposition (CVD),[118] *etc.* Among TMDCs, MoS_2 has been widely used in various environmental applications such as gas adsorption and subsequent reduction to valuable chemicals. The initial attempt on CO_2 capture based on a 2D MoS_2 membrane was carried out by Shen *et al.* and they have reported MoS_2 incorporating Pebax polymer mixed matrix membranes with good CO_2 permeability and selectivity. MoS_2 with stronger adsorption energy for CO_2 (205 meV) than N_2 (137meV) easily got adsorbed. The diffusion or permeation through the

membrane occurs because of the dissolution of the adsorbed gas in the membrane.[119] In a similar way, studies on a defect-free Pebax-MoS_2 membrane obtained by solution casting with different amounts of MoS_2 loading from 0 wt% to 5.66 wt% were explored. The highest CO_2 permeability of 67.05 Barrer and CO_2/N_2 selectivity of 90.61 were observed for the 4.67 wt% MoS_2 incorporating Pebax membrane. Further, the molecular simulation studies proved that the CO_2 solubility and selectivity of the mixed matrix membrane were significantly improved after the addition of MoS_2 due to its high affinity towards CO_2.[120] Later, the influence of the electric field on the adsorption behaviour of CO_2 on the MoS_2 monolayer was analysed[121] by carrying out a systematic investigation using DFT calculations on various parameters such as interactions of CO_2 with MoS_2 in the absence/ presence of an electric field, reaction mechanisms of adsorption, optimization of electric fields for CO_2 capture and finally a comparison with N_2 adsorption by the adsorbent. The DFT calculation showed that an electric field can alter the interaction levels between the adsorbate and adsorbent. For instance, by applying of an electric field of 0.004 a.u., CO_2 showed strong interaction with MoS_2. However, this interaction was least in the absence of an electric field and this was evidenced by the easy release of CO_2 once the electric field was turned off. In contrast, the presence or absence of an electric field did not affect the capture of N_2, and this indicates that MoS_2 can act as a selective adsorbent for CO_2, especially in the presence of an electric field during the post-combustion process where CO_2 and N_2 are the major components of the combustion gas.[121] In another study, Cu nanoparticle incorporating MoS_2 for CO_2 adsorption and catalytic reduction reactions was analysed. The hybrid made at a particular concentration of Cu and MoS_2 (Cu/MoS_2-1) showed better adsorption performance (0.44 cm^3 g^{-1}) than other hybrids [Cu/MoS_2-2 (0.41 cm^3 g^{-1}), Cu/MoS_2-3 (0.27 cm^3 g^{-1})] and bare MoS_2 (0.22 cm^3 g^{-1}). The enhanced CO_2 adsorption in the hybrids was explained by the additional adsorption of CO_2 molecules on the surface of Cu nanoparticles.[122] Further, a theoretical approach for the CO_2 adsorption on the MoS_2 monolayer was made and the DFT calculations reveal the different occupancies of CO_2 molecules on the 2D monolayer surface with low energy cost (ΔE = −57.9 ± 2.5 kJ mol^{-1}) and this points to the adsorbate's physisorption on the adsorbent. The interaction energies calculated for MoS_2 were larger when compared to graphene, which hints at the suitability of MoS_2 nanosheets over graphene for greenhouse gas adsorption applications. Also, from simulation studies, they have inferred that the adsorption process is controlled by van der Waals interactions where CO_2 molecules were arranged parallel to the monolayers of the MoS_2 surface.[76] Cho *et al.* have compared the NO_2 gas adsorption on MoS_2 which is aligned in three different ways such as horizontally aligned MoS_2 with an exposed basal plane, vertically aligned MoS_2 with exposed edges and a mixture of horizontally & vertically aligned MoS_2 layers (exposed basal plane and edges)
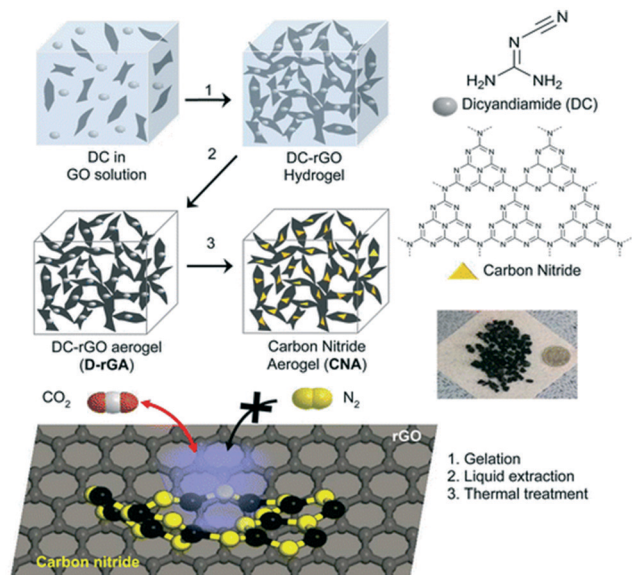
This journal is © The Royal Society of Chemistry 2021

React. Chem. Eng., 2021, **6**, 1701–1738 | **1709**

Fig. 9 The preparation of carbon nitride aerogels for the selective adsorption of CO_2 over N_2. "Reproduced from ref. 135 with permission from American Chemical Society, copyright 2015".

synthesized using a CVD process. They reported that gas adsorption is highly dependent on the alignment of MoS_2 layers, and a significantly higher gas adsorption was observed in edge sites of vertically aligned MoS_2 compared to MoS_2 with an exposed basal plane. The experimental results were well correlated with DFT calculations, where strong NO_2 binding energies near the edge sites of MoS_2 were observed.[123] Based on these results, researchers had concluded that the presence of S-vacancies or defects on the MoS_2 surface is desirable for the adsorption of non-polar gases. Also, they stated the importance of tuning the surface of the adsorbent to obtain reactive edge sites on MoS_2 flakes to target a specific gas of interest.[73] For this, they have investigated the effect of nitrogen doping on defective and non-defective MoS_2 surfaces for CO_2 adsorption properties. MoS_2 with 1S vacancy and MoS_2 with ternary N doped 1Mo vacancy samples showed strong CO_2 binding energies (0.908 eV and 1.818 eV) and this reveals that the defective and N doped MoS_2 can have enhanced CO_2 adsorption due to the covalent and electrostatic interactions with the gas molecule. Conversely, the defect-free MoS_2 showed weak van der Waals interactions with CO_2 leading to poor adsorption characteristics. Moreover, the selective adsorption of CO_2 over N_2 was identified for the defective and N-doped MoS_2, and so the importance of heteroatom-doping and defects in the structure of MoS_2 for the enhanced molecular adsorption of CO_2 was pointed out.[73] A theoretical investigation of the gas adsorption behaviour on $MoSe_2$ was examined using DFT calculations. The results indicated the poor adsorption of CO_2 and CO gases by $MoSe_2$ monolayers, whereas the material was found to be more sensitive towards the adsorption of NO_2 and NO. The high selectivity of $MoSe_2$ towards NO_2 and NO was attributed to the distinct charge

transfer between the adsorbate and adsorbent[124] and this indicates the inability of $MoSe_2$ for CO_2 adsorption applications.

3.3 Hexagonal boron nitride

Hexagonal boron nitride (h-BN) nanosheets are 2D structures and have excellent electrical, thermal, and optical properties with broad applications. A few layered h-BN synthesised from boric acid and urea through a chemical route with a high surface area (927 m^2 g^{-1}) was found beneficial for CO_2 capture applications.[125] Porous and few layered h-BN nanosheet adsorbents from MgB_2 and NH_4Cl with a good micropore volume showed a CO_2 adsorption of ~10 cc g^{-1} with a CO_2/N_2 selectivity of 26.3.[126] The BN adsorbent with a surface area of 235 m^2 g^{-1} showed the maximum CO_2 adsorption at 760 Torr at 298 K. Marchesini *et al.* have investigated the CO_2 adsorption capacity of BN synthesized by using single and multiple N precursors. For instance, BN synthesized using urea showed a microsponge-like structure with the existence of nanometre ranging mesopores, whereas BN synthesized using urea and melamine showed the presence of a crumbled nanosheet with inhomogeneous small mesopores. The scanning transmission electron microscopy (STEM) tomography images of the BN samples are shown in Fig. 8. The high surface area (1900 m^2 g^{-1}) BN sample prepared by using multiple N precursors showed a CO_2 adsorption of 1.6 mmol g^{-1} at 1 bar, 25 °C and 8.3 mmol g^{-1} at 20 bar, 25 °C. They have also evaluated the CO_2 sorption capacity of pelletized and non-pelletized BN samples and it was about 1.1 mmol g^{-1} and 1.6 mmol g^{-1}, respectively, at 1 bar and 25 °C.[31] Further, the effect of C doping on BN sheets was demonstrated by the preparation of a novel C-doped BN with significant CO_2 adsorption properties. A CO_2 uptake of ~2.9 mmol g^{-1} was observed for BN while C-doped BN showed an adsorption of ~5.5 mmol g^{-1} at 273 K and 1 bar.[32] The effect of charge on the BN nanomaterial on CO_2 adsorption was investigated by DFT calculations. BN with a negative charge showed strong interaction with CO_2 while spontaneous desorption of CO_2 from the BN surface was evidenced once the electrons were removed from the system. The charged BN showed high selectivity for CO_2 capture from a gas mixture containing $CO_2/CH_4/H_2$.[81] Similarly, the effect of an electric field on CO_2 adsorption and selectivity was analysed using DFT calculations. The application of a vertical electric field increases the binding energy of CO_2 on h-BN sheets and it was inferred that the h-BN is a suitable candidate for CO_2 adsorption from the gas mixture containing H_2, CH_4, N_2, CO, and H_2O, especially in the presence of an electric field.[80] In a study, the incorporation of the BN nanomaterial in PVA, and subsequent foam formation by freeze drying for CO_2 adsorption was demonstrated. The high gas adsorption of 340% was ascribed to N functional groups and high surface area associated with the BN-PVA foam.[78] In another study, the interactions between the gas and the adsorbent surface

1710 | *React. Chem. Eng.*, 2021, **6**, 1701–1738

This journal is © The Royal Society of Chemistry 2021

and the mechanism of CO_2 adsorption on h-BN nanosheets were analysed using DFT and MD calculations.[77] The report claims the physisorption of CO_2 gas molecules on h-BN nanosheets. The significance of tuning and functionalising the pores of the adsorbent to improve the CO_2 adsorption is highlighted in their study.

3.4 MXenes

MXenes are another class of 2D materials that have received significant attention beyond graphene, TMDCs, and h-BN. They are early transition metal carbides and carbon nitrides such as Ti_2AlC, Ti_3AlC_2, Ti_3C_2, Ti_2C, Nb_2C, V_2C, Ti_3CN, etc. with metallic conductivity and strong ionic, covalent and metallic bonds.[127] The general formula for MXene is $M_{n+1}X_n$-T_x (n = 1, 2, 3), where M is the early transition metal, X is carbon or nitrogen, and T represents terminal functional groups. MXenes are produced by selective etching of group III A or IV A elements using hydrofluoric acid. Due to the toxic nature of HF, other environmentally friendly methods adopted are alkali treatment,[128] electrochemical etching,[129] Lewis acid etching,[130] etc. The CO_2 uptake by 2D MXene carbides (M_2N) was analysed by DFT calculations, and a gas loading capacity of ~2.3 to 7.96 mol kg^{-1} at low CO_2 partial pressure and high temperature was achieved and this hints at its practical utility for CO_2 adsorption directly from the atmosphere.[33] The relation between the microstructure of carbide MXenes ($Ti_3C_2T_x$, V_2CT_x) and the CO_2 adsorption properties was analysed.[34] DMSO intercalated $Ti_3C_2T_x$ with a surface area of 66 m^2 g^{-1} and high volume capacity of 502 Vv^{-1} showed a CO_2 adsorption capacity of 5.79 mmol g^{-1} at 298 K and 0–4 MPa. Similarly, the effect of the thickness of carbide MXenes was analysed by DFT calculations, and the results confirmed the efficiency of these materials for CO_2 capture with a minor influence from the thickness of the

material. Also, the surface of different carbide MXenes (M_{n+}-C_n: n = 1 to 3, M = Ti, Zr, Hf, V, Nb, Ta, Mo, and W) was analysed and the largest adsorption energy was observed for the system with a d^2 electronic configuration and then for d^3 and d^4 systems.[82] A similar type of DFT calculation on CO_2 adsorption and conversion based on M_2C type MXene was carried out and the results indicate that the presence of a surface lone pair of electrons is the driving force for the adsorbate–adsorbent interactions.[131] In another study, the adsorption/desorption rate of CO_2 on 2D M_2N materials (M = Ti, Zr, Hf, V, Nb, Ta, Cr, Mo, W) was analysed using DFT calculations. The study evidenced the existence of adsorbed anionic $CO_2^{\delta-}$ species with significant MXene to CO_2 charge transfer. The considerable adsorption energy (−3.13 eV) makes M_2N more suitable than M_2C for efficient CO_2 capture and storage. Due to the high electronegativity N layer, M_2N can withdraw a higher charge density from the metal than the C layer in M_2C, and this implies a reduction in the charge transfer from the metallic layer of MXene to CO_2 in M_2C type MXene.[132] In a study, effective adsorption of CO_2 gas (≈12 mol kg^{-1}) on individual sheets of 2D $Ti_3C_2T_x$ carbides was reported.[133] Recently, the CO_2 separation capacity of the Ti_3-C_2T_x incorporating Pebax mixed matrix membrane was compared with a GO filled membrane. Around 20 wt% of Ti_3-C_2T_x was able to disperse in the matrix due to the good level of interfacial interactions arising from the presence of polar groups present in MXene. In contrast, only 5 wt% of GO was able to be incorporated in the Pebax matrix. The high level loading of MXenes was found to be beneficial especially under humid reaction conditions, but it was not promising under dry conditions.[134]

3.5 Carbon nitride

Graphitic carbon nitride (g-C_3N_4) has received tremendous attention because of its excellent properties and similarities with 2D graphene and it consists of hexagonally organized heptazine (tri-s-triazine) units linked through tertiary amines. The conventional exfoliation of carbon nitride is of less interest because of the tightly packed heptazine units.[135] However, the synthesis of g-C_3N_4 through the direct pyrolysis of N-rich precursors like urea makes it more approachable.[85] Since the nitrogen species in g-C_3N_4 is of low alkalinity, the interaction between g-C_3N_4 and CO_2 is weak, and the use of pristine g-C_3N_4 for CO_2 adsorption application is limited. However, amine functionalization via chemical grafting or physical impregnation can lead to more adsorbent–adsorbate interactions. For instance, the physical impregnation of polyethyleneimine (PEI) with g-C_3N_4 was analysed for CO_2 adsorption applications. A CO_2 adsorption capacity of 3.77 mmol g^{-1} was observed for PEI-C_3N_4 composites at 100 °C and ambient pressure, which was superior to pristine g-C_3N_4. The study inferred that the presence of amine groups on the composite surface, not the surface area, plays a major role in deciding the CO_2 adsorption capacity.[85] Reduced graphene oxide aerogel was reported as a template platform for the
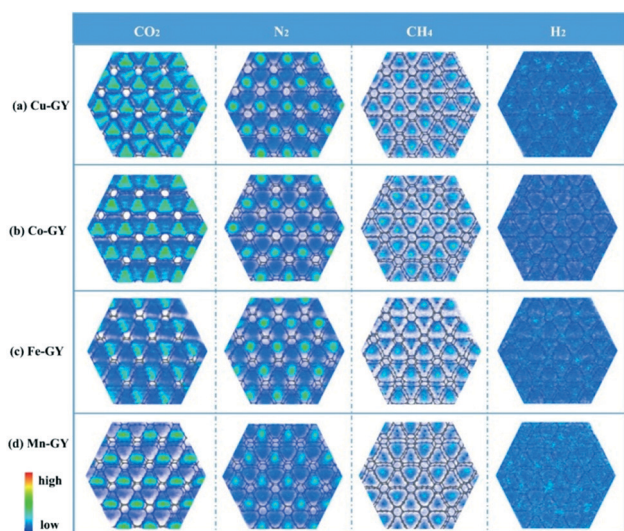

Fig. 10 CO_2, N_2 CH_4 and H_2 gas distributions on TM-GY. "Reproduced from ref. 147 with permission from Elsevier, copyright 2021".

This journal is © The Royal Society of Chemistry 2021

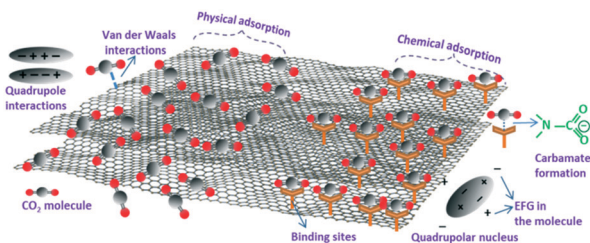React. Chem. Eng., 2021, **6**, 1701–1738 | **1711**

Fig. 11 Interaction between CO_2 and the adsorbent during physical and chemical adsorption.

growth of porous carbon nitride with a good surface area for CO_2 adsorption applications. The gelation of the carbon nitride precursor (dicyandiamide) incorporating graphene oxide solution, and the subsequent solvent exchange, liquid extraction and thermal treatment resulted in the formation of carbon nitride–graphene oxide aerogels. The schematic of the synthesis of carbon nitride aerogels for selective CO_2 capture is shown in Fig. 9. A CO_2 adsorption capacity of 0.43 mmol g^{-1} at 0.1 bar and 300 K was observed for these aerogels with excellent regeneration capability (R = 97.6%) and high CO_2 selectivity.[135] In another study, a high-pressure investigation of ionic functionalized graphitic carbon nitride for CO_2 adsorption was analysed. CO_2 adsorption of g-C_3N_4 nanosheets functionalized with an ionic liquid (1-butyl-3-methylimidazolium bis(trifluoromethyl sulfonyl)imide ([BMIM][TFSI])) was analysed at 15 bar pressure and 25 °C showing a sorption capacity of 42.93 mmol g^{-1} which was higher as compared to g-C_3N_4 nanosheets (19.78 mmol g^{-1}) and bulk g-C_3N_4 (8.54 mmol g^{-1}). Due to the combined effects of physisorption and chemisorption, an enhanced interaction between CO_2 and ([BMIM][TFSI]) functionalized g-C_3N_4 nanosheets was achieved and this led to a high CO_2

uptake.[35] The non-noble metal single-atom catalysts of Fe, Co, Ni and Cu supported on g-C_3N_4 were recently explored for CO_2 adsorption. DFT calculations revealed that the CO_2 adsorption energies of Fe-g-C_3N_4, Co-g-C_3N_4, Ni-g-C_3N_4, and Cu-g-C_3N_4 were −0.40, −0.16, −0.21, and −0.17 eV, respectively.[136]

3.6 Other 2D materials

MOFs and COFs have been reported for gas adsorption applications. An ultrathin mixed matrix membrane containing a 2D MOF was prepared, and the addition of lamellar 2D copper 1,4-benzenedicarboxylate (MOF) nanosheets led to the formation of dense membranes with good CO_2 selectivity (15.6), and high CO_2 permeance (407 GPU) was reported.[137] MOFs are linked by unstable coordination bonds, particularly under heat and humid conditions, and this structural instability is a significant problem, especially for CO_2 capture in pre or post-combustion processes. However, COFs are linked by covalent bonds and are structurally stable to use under drastic conditions of CO_2 capture. Further, the introduction of N functionalities and the pore size tuning of COFs make them interesting for gas adsorption applications.[138] 2D COFs are mainly used in the preparation of membranes for the capture and separation of CO_2 gas.[137–140] Water-soluble COFs with 2D characteristics and porosity were prepared and blended with commercial polymers to form mixed matrix membranes (MMMs). The defect-free and mechanically stable COF incorporating MMMs showed better selectivity and gas permeability when compared to the pristine polymer membrane.[140] In another work, DFT and MD calculations under thermodynamic conditions of a post combustion

Table 2 Adsorption capacities of various 2D nanomaterials and their hybrids

Adsorbent	BET surface area (m² g⁻¹)	Operating conditions		Type of adsorption	Adsorption capacity (mmol g⁻¹)	Ref.
		Pressure (bar)	Temperature (°C)			
Graphene	42.87	11	25	Physisorption	21.6	26
Borane modified rGO	514	1	25	Physisorption	1.81	103
rGO/N-doped porous carbon composite	865.1	5	25	Chemisorption and physisorption	5.77	27
MgAl MMO/rGO	96.8	8	300	—	2.36	108
N-Rich graphene based semi-coke-like material	701.53	30	25	Physisorption	7.11	109
B and N co-doped graphene aerogels (BN-GA)	169.9	1	0	—	2.1–2.9	111
PANI decorated graphene	—	11	25	Chemisorption and physisorption	75	82
Fe_3O_4/graphene	98.2	11	25	Chemisorption and physisorption	60	28
PANI/GO	5	20	27	Physisorption	3.2	29
PPy/rGO	1650	1	0	—	6.8	30
N-Doped MoS_2	—	—		Chemisorption and physisorption	—	73
Porous BN	1900	1–20	25	Chemisorption and physisorption	1.68.3	31
C doped BN	—	1	0	Physisorption	~5.5	32
MXene, M2N	—	1	727	Physisorption	7.96	33
$Ti_3C_2T_x$	66	4	25	Physisorption	5.79	34
Polyethyleneimine/g-C_3N_4	1.2	1	100	Physisorption	3.77	85
C_3N_4 functionalized porous rGO aerogel	450	0.1	27	Physisorption	0.43	135
g-C_3N_4 nanosheets functionalized with ionic liquid	182.9	15	25	Chemisorption and physisorption	42.93	35
Cu doped graphyne	—	1	25	Chemisorption	8.46	147
Polyphosphoric acid modified MMT/rGO hybrid	50.77	1	25	Physisorption	0.5	150
Octadecylamine modified MMT	11.82	50	25	Chemisorption	7.16	36

process were applied on a diamine linked 2D COF membrane for CO_2 gas adsorption. The results hint at the physisorption and better selectivity for CO_2 gas molecules over N_2 by the 2D COF.[138] An ultrathin membrane was fabricated in a recent study by layering two intrinsically charged ionic covalent organic nanosheets. The layered ultrathin hybrid membrane showed better gas separation properties compared to their counterparts. The overall H_2/CO_2 separation performance was excellent compared to literature results.[141] Recently, a 2D COF and 3D MOF dual layered membrane was reported for H_2/CO_2 separation. A 3D MOF film with vertical binding sites to accommodate a 2D COF producing a 2D COF composite membrane with superior H_2/CO_2 selectivity (32.9) and high permeability was reported.[139]

Borophene is a new type of 2D material and it is a single-layered boron-based material with all four different phases being metallic.[142] DFT calculations demonstrated the utility of conductive borophene nanosheets for gas adsorption applications. The binding strength of CO_2 molecules on the adsorbent can be enhanced by introducing an extra electron to it, which leads to a CO_2 capture capacity of up to 6.73×10^{14} cm^{-2}.[143] Later, the gas (CO, NO, CO_2, NO_2, H_2S, and NH_3) adsorption properties of borophene were analysed relative to the adsorption energies. The negative values of adsorption energy indicated the strong adsorption characteristics of the gases on the adsorbent. Further, the introduction of a transition metal into borophene reduced the adsorption energy, and this indicates the advantages of transition metal doping on borophene for enhanced CO_2 adsorption.[144] The adsorption of gas molecules (CO, CO_2, NH_3, NO, NO_2 and CH_4) on borophene was analysed by DFT calculations, and the studies revealed the chemisorption of all gases except CH_4 on borophene.[145]

Another new type of 2D nanomaterial is green phosphorus and its monolayer variant green phosphorene. The CO_2 adsorption properties of the phosphorene slit pores were studied using DFT and GCMC calculations, and the adsorption of natural gas was analysed at 300 K and pressure up to 3 MPa. The simulation results indicate the better selectivity for CO_2 over CH_4 in a binary mixture of CO_2/CH_4 with an enhanced adsorbate–adsorbent interaction, especially at a high mole ratio of CO_2 in the gas phase.[84] Recently, the strong adsorption of NO, NO_2, CO, and CO_2 gases on green phosphorene was analysed using theoretical calculations.[146] Another 2D material included in the C family is graphyne, which is one atom thick and consists of sp and sp^2 carbon atoms. Very recently, first row transition metal doped graphynes for enhanced CO_2 adsorption with good selectivity using grand canonical Monte Carlo (GCMC) and DFT techniques were investigated by researchers. The transition metals (TM) like Cu, Co, Fe and Mn were selected for doping with graphyne and the most stable Cu doped graphyne (Cu-GY) exhibited a high CO_2 uptake of 8.46 mmol g^{-1} at 298 K and 1 bar. The enhanced stability of Cu-GY is due to the high cohesion and formation energies, and the Cu-GY adsorbent showed good selectivity for CO_2 over methane

($\sim$330.61), nitrogen ($\sim$912.68), and hydrogen ($\sim$2640.94) gases. The high CO_2 adsorption capacity and selectivity of Cu-GY are due to its high isosteric heat (40 kJ mol^{-1}), which was higher than other TM-GY adsorbents. The 2D density of different gases on the TM-GY adsorbent was analysed using Monte Carlo configurations at 298 K and 1 bar (Fig. 10). The green areas in the plot represent the high density of gases while the blue area shows the low density of gases. Fig. 10 shows the CO_2 adsorption abilities of TM-GY with low H_2 adsorbing properties. The strong interaction of gas molecules with metal doped graphyne and the multilayer adsorption on the adsorbent make graphyne a promising material for CO_2 separation and capture applications.[147]

Nanoclays are another class of 2D materials of layered mineral silicate with a few nanometer thickness and exceptionally high mechanical properties. Since they are based on a mineral, nanoclays are one of the most economical and abundant solid adsorbents used for pollutant removal. Montmorillonite (MMT) clay is widely used, and it is under the smectite group. Layers of MMT contain an octahedral sheet with an Al cation sandwiched by two tetrahedral sheets with the main silicon cation.[148] The major drawback of clay-based materials for CO_2 adsorption is their low efficiency CO_2 uptake under moist conditions and this was due to the diffused water molecules that prevent the capture of gas molecules. In the absence of water molecules (dry conditions), one can expect high CO_2 uptake due to nano-channels in the clay for the intercalation of CO_2 molecules. An analysis of variance (ANOVA) study was carried out to predict the major process variable on CO_2 adsorption. The results indicated the importance of temperature and pressure on the adsorption process. Under optimum conditions of temperature and pressure of 25 °C and 9 bar, a CO_2 adsorption of 100.67 mg g^{-1} was achieved and a good agreement between theoretical and predicted (104 mg g^{-1}) values of gas adsorption was observed.[148] Like the above-mentioned study, an ANOVA treatment was tried on NaOH modified MMT by the same research group. Under optimum conditions of temperature (65 °C), pressure (1 bar), acid concentration (5.99 M) and wt% NaOH (39.76%), a CO_2
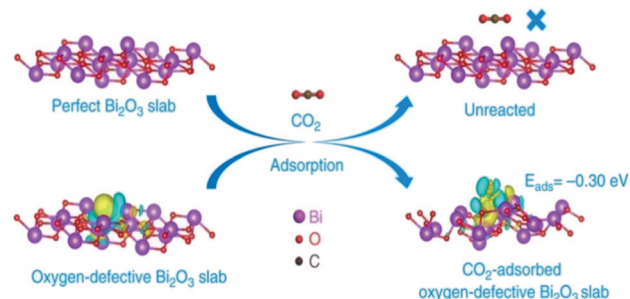

Fig. 12 Schematic of the DFT studies showing selective adsorption and conversion of CO_2 on oxygen defective Bi_2O_3 nanosheets. "Reproduced from ref. 172 with permission from Nature, copyright 2019".

adsorption of 105.55 mg g^{-1} was observed with a desirability index of 0.996, which reveals the good correlation between experimental and predicted gas adsorption values.[149] In another study, the effect of surface modification of MMT with polyphosphoric acid and hybridization with rGO for CO_2 adsorption at 25 °C and 1 bar was analysed and the modified MMT/rGO hybrid showed a CO_2 adsorption of ~0.5 mmol g^{-1} at low pressure.[150] Another method to improve the gas adsorption properties of pristine MMT is the functionalization or grafting nitrogen functionalities to MMT. Therefore, octadecylamine modified MMT was prepared, and showed a CO_2 uptake of 7.16 mmol g^{-1} at room temperature and high pressure of 50 bar while the pristine MMT showed only 3.47 mmol g^{-1} under similar conditions.[36]

To summarize, a greater amount of CO_2 adsorption was evidenced by nitrogen doping or by introducing nitrogen functionalities in the system and this is due to the chemisorption of the CO_2 adsorbate on the solid adsorbents. The chemisorption of CO_2 on N doped adsorbents was explained through the Lewis acid–base interactions, in which CO_2 is a weak Lewis acid due to the presence of electron deficient C and negatively charged nitrogen sites act as Lewis bases. Further, in N-doped systems, the interactions between EQM of the CO_2 molecule and local polarization in nitrogen-doped adsorbents enhance the CO_2 adsorption energy, leading to selective and higher CO_2 adsorption from the flue gases.[6] However, in amine functionalized adsorbents,

surfaces exhibit a different type of interaction with CO_2 molecules. The primary, secondary or tertiary amine functionalized adsorbents interact with CO_2 via the formation of the zwitterion intermediate to form carbamates. In the absence of water, which is an additional free base required for the formation carbamate from the intermediate, another mole of amine is utilized. Thus, in the absence of water molecules, two moles of amine are required to capture one mole of CO_2.[151] Nonetheless, due to reduced thermal stability of amine functionalised adsorbents, N doped adsorbents are preferred for CO_2 capture. On the other hand, during physical adsorption, along with the van der Waals attraction of CO_2 and the adsorbent, EQM–electric field gradient interactions are also taking place. The value of EQM is the main factor deciding the selectivity for gases and therefore, carbon dioxide molecules with a high EQM value will be attracted and adsorbed on the solid surface when compared to low EQM N_2 gas. Fig. 11 represents the possible types of interactions taking place during the adsorption of CO_2 on the adsorbent. Another strategy to improve the adsorption capacity is developing porous adsorbents with an adequate surface area and varied morphology. Therefore, we can conclude that high surface area adsorbents with N doping could deliver enhanced CO_2 adsorption characteristics. The CO_2 adsorption capacities of various 2D nanomaterials and their hybrids are summarized in Table 2. It showed that high adsorption capacities have been achieved for 2D nanomaterials by implementing high CO_2 pressure (10 to 30 bars) which hints at their utility for CO_2 capture during post and pre-combustion capture processes. However, the developments of 2D nanomaterial-based adsorbents which can adsorb an adequate amount of CO_2 from the atmosphere make them more attractive due to the possibility of direct removal of CO_2 from the atmosphere. From the data described in Table 2, we can infer that N-doped porous or aerogel materials based on graphene or MXenes are expected to have future advances in low-pressure CO_2 adsorption applications.
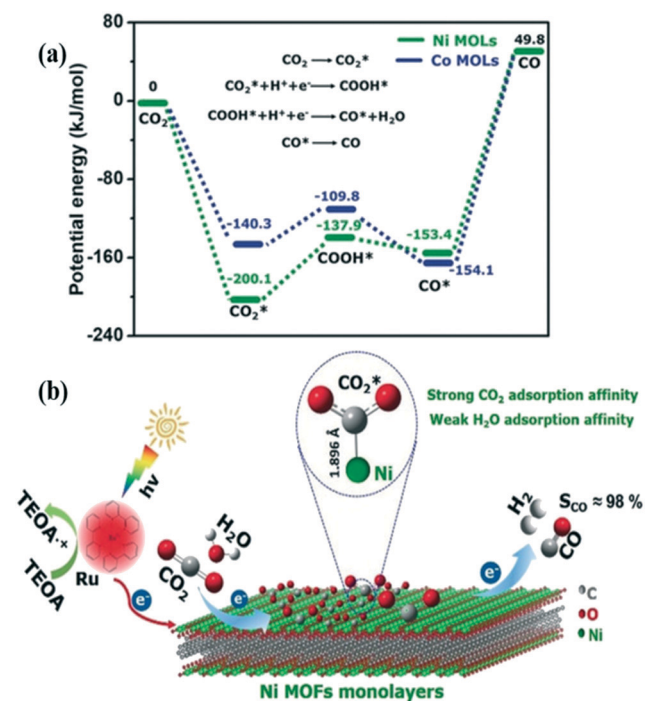

Fig. 13 (a) The potential energy diagram calculated by the DFT studies explaining the energy barriers associated with the conversion of CO_2 to CO. (b) Schematic illustration of CO_2 reduction over Ni-MOFs. $[Ru(bpy)_3]^{2+}$ acts as a photosensitizer, and triethanolamine (TEOA) is used as a sacrificial electron donor. "Reproduced from ref. 174 with permission from Wiley-VCH, copyright 2018".

3.7 Impact of defect engineering on CO_2 adsorption

Structural disorders or defects are vital features that can affect the physical and chemical properties of solid materials. These defective sites can serve as active points during various chemical and physical reactions. In 2D materials, common defects such as vacancies, dopants, substitution, edges and grain boundaries have been observed, leading to enhanced material properties. Apart from these, defect engineering in 2D nanomaterials can be triggered by plasma, electron beam, ozone, and chemical treatments. Defect engineering can be exploited for increased CO_2 gas adsorption capacities of 2D solid adsorbents. For instance, the defect engineering of sp^2 carbon of graphitic structures of graphene was analyzed using a van der Waals-corrected DFT calculation for improved CO_2 capture and separation. The topological defects on graphene such as vacancies (mono, di), Stone–Wales defects,
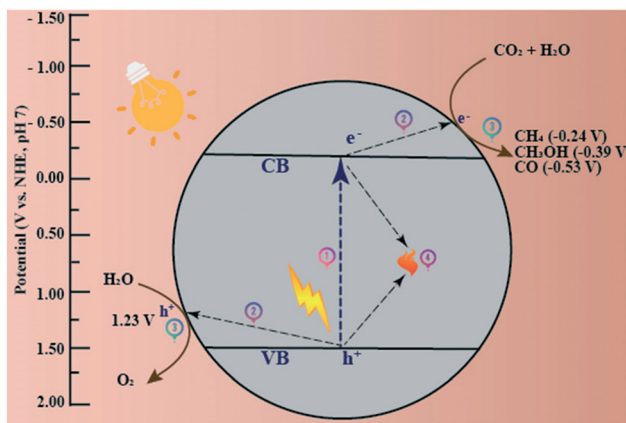
1714 | *React. Chem. Eng.*, 2021, **6**, 1701–1738

This journal is © The Royal Society of Chemistry 2021

Fig. 14 Schematic of the four different steps involved in the photocatalytic CO_2 reduction by a heterogeneous catalyst. (1) Light absorption, (2) migration of charge carriers to the photocatalytic surface, (3) water oxidation and CO_2 reduction, and (4) recombination of electrons and holes. Thermodynamic potential values associated with water oxidation and CO_2 reduction into CO, CH_4 and CH_3OH are also reported.

strained graphene (by compression and tensile forces), and graphene folds were considered for the evaluation of the binding energy of gases (CO_2 and CH_4). Their study reveals that the concave sites in rippled graphene geometries and SW defect sites can enhance the sorption/binding properties.[152] In another study, DFT calculations of CO_2 adsorption on a defected graphene sheet hint at the physisorption of the gas molecule on the top of the vacancy. Later, the surrounding vacancy can lead to lactone formation and subsequent chemisorption of CO_2. The model suggested a reaction pathway that ends up in the desorption of O_2 with a minimum energy penalty.[153] The defect engineering of MoS_2 for better CO_2 gas adsorption was analyzed using DFT calculations. The results highlighted the importance of Mo, S vacancies, and N doping for improved CO_2 gas adsorption compared to defect-free MoS_2. According to their study, MoS_2 with one sulfur-vacancy and tertiary nitrogen-doped one Mo-vacancy led to enhanced gas adsorption.[73] Similarly, the gas adsorption properties of MOFs can be improved by defect engineering by influencing the factors such as the density of co-coordinatively unsaturated sites, pore size, and specific surface area. As an example, mesopores can be created with vacancy defects, or one can make a porous coordination network compound from a dense coordination network system through defect engineering.[154] The CO_2 adsorption and sensing properties of a pristine and defected black phosphorene were analyzed using DFT calculations. A significant change in the bandgap was observed after vacancy doping, and the initial CO_2 sensitivity was markedly improved by a factor of 50 upon the defect engineering of black phosphorene.[155] In a study, defect engineering of a 2D ferromagnet, Fe_3GeTe_2, was carried out using DFT calculations to suggest an adsorbent with enhanced gas adsorption properties. The Te-deficient Fe_3GeTe_2 monolayer can adsorb CO_2 and H_2O covalently on the surface of the

adsorbent. However, physisorption of gases was observed with the defect-free ferromagnet. Also, the estimated adsorption ability of defected Fe_3GeTe_2 was higher than MoS_2 and MXenes.[156] Even though there are a few reports on the theoretical aspects of defect engineering in 2D materials for enhanced CO_2 adsorption, research focusing on experimentation in this area should be well explored for future developments.

4. Catalytic conversion of CO_2

The conversion of CO_2 to valuable chemical feedstocks is of paramount importance to the chemical industries.[25] Many of the existing technologies for converting CO_2 to value-added products are not cost-effective. So, the research community is keen to identify catalytic materials able to perform CO_2 reduction with lower energy input. Among the various materials currently researched, 2D materials are of particular interest because of their high selectivity and mild reaction conditions.[7,11,157,158]

4.1 Thermodynamics and kinetics of CO_2 reduction

The CO_2 molecule has a low electron affinity, and its transformation is a thermodynamically uphill process.[159] The CO_2 transformation occurs by a nucleophilic attack at the carbon atom, and C=O bond dissociation requires a relatively high energy of 750 kJ mol^{-1}.[11] A single electron transfer to the CO_2 molecule to generate the $CO_2^{\cdot-}$ radical is considered the first step in the CO_2 reduction mechanism.

$$CO_2 + e^- \rightarrow CO_2^{\cdot-} \ (-1.9 \text{ V } vs. \text{ NHE at pH} = 0)$$
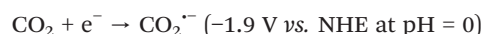
$CO_2^{\cdot-}$ radical generation is associated with a highly negative reduction potential value of −1.9 V (vs. NHE), and therefore CO_2 reduction processes need higher overpotential values.[160] The single-electron transfer step (first step) turns out to be the rate-limiting step of CO_2 reduction owing to the higher reorganisation energy between the linear CO_2 molecule and bent $CO_2^{\cdot-}$ radical.[161] Hence the thermodynamic barrier linked to the CO_2 activation step eventually decreases the efficiency of CO_2 reduction processes.

Another mechanism for CO_2 reduction involves the multiple proton-coupled electron transfer (PCET) processes.[162,163] PCET is necessary to avoid the activation barriers and excludes the formation of unstable intermediates.[164] As the name suggests, the PCET mechanism kinetically relies on the concentration of protons available in the system. CO_2 reduction to methanol and methane requires the transfer of six and eight protons, respectively.[165,166] As the number of protons and electrons involved in the PCET reaction increases, it escalates the complexity of the reaction.[161] Therefore, various reports of CO_2 conversion to valuable products like methanol and methane reveal drawbacks such as poor selectivity and low conversion efficiency.[167,168] The hydrogen evolution reaction (HER) from water is kinetically more favourable than CO_2

This journal is © The Royal Society of Chemistry 2021

React. Chem. Eng., 2021, **6**, 1701–1738 | **1715**

reduction. Consequently, proton reduction competes with CO_2 reduction and decreases the efficiency of CO_2 transformation.[169] The readers are redirected to previous reviews for a detailed understanding of the thermodynamic and kinetic aspects of CO_2 reduction reactions.[161,170]

4.2 Structure function relationship in CO_2 reduction catalysts

Correlating the structural features of the 2D catalyst with the catalytic performance is an exciting area to be explored. An in-depth analysis of the specific structural features and understanding their role in the catalytic mechanism help researchers in modulating the catalyst for obtaining the desired products. Fine-tuning the oxygen vacancies and single atoms present on the catalytic surface can help achieve the selectivity to the product.[171,172]

In a recent study, Bi_2O_3 nanosheets with oxygen vacancies were demonstrated to fix CO_2 to dimethyl carbonate.[172] The oxygen vacancies present on the atomic layers decreased the adsorption energy of CO_2 on the surface and enhanced the generation of the $CO_2^{\cdot-}$ radical by a single-electron transfer. The difference in the charge density observed between non-defective Bi_2O_3 nanosheets and oxygen defective Bi_2O_3 nanosheets provided insights into the possibility of electron localisation around the oxygen vacancies. DFT calculations arrived at a negative adsorption energy of -0.30 eV for the CO_2 adsorbed on oxygen defective Bi_2O_3 nanosheets (Fig. 12). On the contrary CO_2 chemisorption was not observed on the non-defective Bi_2O_3 nanosheets owing to their weak interaction with CO_2. In a similar study, atomic layers of SnS_2 with varying oxidation degrees were synthesized to understand the correlation of oxidized sulfides and their efficiency for CO_2 to CO conversion.[173] DFT calculations concluded that electron localization occurring at the oxidized domains of SnS_2 was stabilizing the COOH* intermediate formation resulting in a decreased CO_2 activation energy. The mildly oxidized SnS_2 layers were reported to have a CO_2 to CO conversion rate 2.6 times higher than the pristine SnS_2 atomic layers.

Fig. 15 SEM and TEM images of (a and d) pristine g-C_3N_4; (b and e) bare NH_2-MIL-101(Fe); (c and f) MCN-3 heterostructure. "Reproduced from ref. 203 with the permission from American Chemical Society, copyright 2020".

In another study, the CO_2 to CO conversion performances of Ni-MOFs and Co-MOFs were compared.[174] In the presence of 10% diluted CO_2, Ni-MOFs showed a 96.8% CO selectivity with a quantum yield of 1.96%. But the CO_2 to CO conversion efficiency of Co-MOFs was negligible in the diluted CO_2.

Experimental and theoretical investigations demonstrated the specific adsorption affinity of CO_2 molecules over the Ni-MOFs and the resulting formation of Ni–CO_2 adducts (Fig. 13, schematic representation). The CO_2 to CO reduction pathway proceeds through a COOH* intermediate. The DFT calculations revealed the potential energy barrier associated with CO_2^* to COOH* conversion to be 62.2 kJ mol^{-1} for the Ni-MOFs (Fig. 13). But the CO_2^* to COOH* energy barrier for the Co-MOFs was 30.5 kJ mol^{-1}, suggesting that the COOH* formation is kinetically favorable on the Co-MOFs compared to the Ni-MOFs. DFT studies, along with the experimental findings, concluded that the initial adsorption of CO_2 over the Ni-MOFs is the rate-determining step of CO_2 to CO conversion, rather than the electron transfer process.

The role of single atoms (palladium and platinum) anchored on g-C_3N_4 (Pd/g-C_3N_4 and Pt/g-C_3N_4) in the CO_2 reduction reaction was investigated by DFT calculations.[175] Introducing Pd and Pt single atoms on the g-C_3N_4 surface enhanced the visible light absorption capacity. Here g-C_3N_4 was the source of hydrogen (H*) *via* the HER, and the single atoms (Pd and Pt) were the active sites responsible for CO_2 reduction. DFT studies concluded that the Pd/g-C_3N_4 catalyst is efficient in transforming CO_2 to HCOOH with a barrier of 0.66 eV, whereas the Pt/g-C_3N_4 catalyst was suitable for selectively reducing CO_2 to CH_4 with a barrier of 1.16 eV. In another study, surface alkalinisation of Ti_3C_2 MXenes was reported to have improved the selectivity for CO_2 reduction to CH_4.[176] Similarly, a ruthenium nanoparticle incorporating layered double hydroxide (LDH) was efficient in reducing CO_2 to CH_4.[177]

4.3 Photocatalytic reduction of CO_2

The reduction of CO_2 to renewable chemicals/fuels in the presence of sunlight and semiconductors is called photocatalytic CO_2 reduction (PCCR).[178,179] This multistep process is possible under both UV and visible light irradiation, yielding hydrocarbons and alcohols with respect to the distinct potentials exhibited by photocatalysts.[180,181] Nevertheless, PCCR is remunerative in the case of economic and environmental terms but inferior in terms of efficiency and selectivity, as the conventional photocatalysts are overwhelmed with the high charge carrier recombination rate and inept reactor design, apart from poor light harvesting ability leading to low yield.[182] To ease these shortcomings, among many suggested ameliorating efforts such as bandgap engineering, co-catalyst loading, non-metal doping, and construction of heterojunctions, choosing a low-dimensional photocatalyst should be the fundamental and baseline norm for designing a flawless photocatalyst.
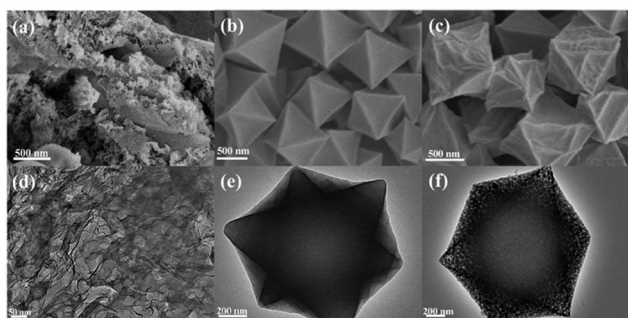
1716 | *React. Chem. Eng.*, 2021, **6**, 1701–1738

This journal is © The Royal Society of Chemistry 2021

4.3.1. Mechanism of photocatalytic CO_2 reduction. The adsorption of CO_2 molecules on the surface of the photocatalyst is a critical step in reducing CO_2 to valuable chemicals. A detailed description with schematic diagrams on the possible modes of CO_2 adsorption on the photocatalyst surface can be found in previous reviews.[25,167,183] The adsorbed CO_2 molecule on the surface loses its linear structure, resulting in the lowering of the LUMO levels of CO_2.[184,185] Now the CO_2 molecule accepts the photogenerated electrons from the photocatalyst, and various reduced products are formed. Different strategies such as incorporating surface defects, introducing a co-catalyst, and increasing the surface area are reported to improve the surface adsorption ability of the CO_2 molecule on the photocatalyst.[186–188]

The crucial processes involved in PCCR are summarized in Fig. 14.[183] At first (1), light radiation with energy higher than the bandgap of the photocatalytic material leads to the generation of electron–hole pairs in the photocatalyst. Then (2), the electrons and holes migrate to the photocatalyst surface. Later the photogenerated electrons reduce the CO_2 molecules into valuable products, and the holes convert H_2O to O_2 (3). The recombination of electron–hole pairs in PCCR reactions takes place (4). The first two steps in photocatalytic CO_2 reduction are the same as those of water splitting. The surface interactions that occur on the photocatalyst determine the fate of the reaction: CO_2 reduction or proton reduction.

4.3.2. 2D material assisted photocatalytic reduction of CO_2. 2D nanosheets are superior in photocatalysis to 1D and 0D due to their large surface area, ample surface active sites, augmented electron mobility, better electron transfer platform, and outstanding photocatalyst support.[189] 2D photocatalysts include graphene,[190] g-C_3N_4,[191] TMCDs,[192] metal oxides,[193] LDHs,[194] MXenes,[195] h-BN,[196] etc. The allure lies beneath their innate advantage of having refined light absorption properties besides a reduced electron–hole migration distance to the photocatalyst surface enriched with defects that render bandgap modulation and charge transfer to the adsorbate. The photocatalytic process can be identified by a series of reactions comprising adsorption of CO_2 onto the surface, photo-generation, separation, and subsequent transportation of charge carriers, and the chemical reactions between adsorbed CO_2 and charge carriers.

A practical tactic to improve the photocatalytic performance of the GO nanosheets was devised recently by increasing the defect density on the GO surface. When defects are created, more active sites could trap the photo-excited charge carriers and suppress the recombination process, reliable enough to advance without any hole scavengers like water and providing a result three times better than non-irradiated GO.[197] This conventional notion conflicting study revealed the role of defect density in the photocatalytic activity. The less defective graphene decorated TiO_2 exhibited up to a seven-fold rise in CH_4 formation with respect to pristine TiO_2. Compared to rGO with higher defect density, graphene facilitates the smooth diffusion of photo-generated electrons to the reactive sites, triggering the electrical mobility following the photo-reduction process.[198] The fabrication of Cu_2O/rGO composites was conducted by a one-step microwave method, where the CO_2 reduction activity of Cu_2O spotted to have risen dramatically, apparently six times higher than Cu_2O and fifty times higher than the Cu_2O/RuO_x junction, pinpoints the significance of rGO in the process. Together with the enhanced stability of Cu_2O, the proficiency in charge separation and mobility can be ascribed to rGO and its protection function providing an economically viable photoreduction of CO_2, which can thus exclude expensive and rare noble metals like Pt, Pd, Au, Ag, etc.[199] Generally, CO_2 reduction and water splitting are two rival reaction processes that co-occur during the CO_2 reduction process in water resulting in poor yield due to the sheer competition for reactive sites. A manipulated rGO nanosheet, which created more individual reactive sites, was explored, effectively separating and distributing the excess excitons generated by quantum-sized photocatalysts. Here, they fabricated a rGO composite of bismuth monoxide quantum dots (rGO-BiO QDs) furnished with an exclusive charge transfer pathway by a typical hydrothermal method. The synergistic effect resulted in the formation of H_2 and CH_4 yielding up to 102.5 and 21.75 µmol g^{-1} h^{-1}, respectively, in the absence of any noble metals or sacrificial agent, beating the direct water splitting production rate, to date.[200]

Unlike graphene, g-C_3N_4 is a conjugated polymeric visible-light-driven photocatalyst with many hallmark features, including band structure, thermal and chemical stability, etc. In g-C_3N_4 the conduction band (CB) edge is necessarily negative for CO_2 reduction, and it can proceed without any co-catalysts. In a study, g-C_3N_4 with two different precursors was fabricated with a large surface area mesoporous flake-like structure from urea with enhanced
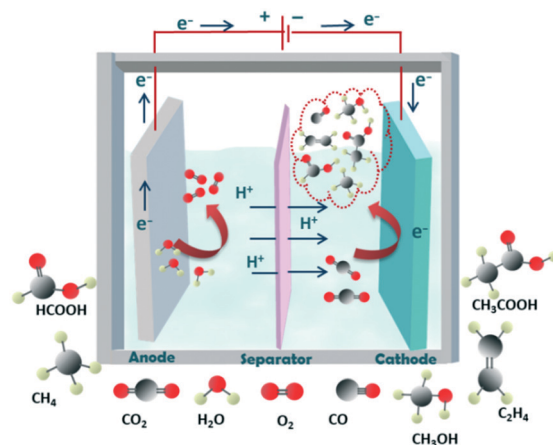

Fig. 16 Schematic diagram representing the formation of various valuable products via the electrochemical CO_2 reduction method.

This journal is © The Royal Society of Chemistry 2021

React. Chem. Eng., 2021, **6**, 1701–1738 | **1717**

photocatalytic activity compared with the non-porous flaky photocatalyst derived from the melamine precursor. However, the latter exhibited a selective formation of C_2H_5OH.[201] Still, a high recombination rate of the photogenerated charge carriers is an everlasting challenge to an efficient photocatalyst. The progress in the photocatalytic applications of g-C_3N_4-based semiconductors for CO_2 reduction was summarised in which they suggested a few modifications which can bring about a hike in adsorption and charge separation rates such as structural tuning, elemental doping, co-catalyst addition, and so on.[202]

Doping a non-polar element like carbon quantum dots on g-C_3N_4 offers many benefits, such as bandgap tapering and electron-withdrawing effects, which facilitate light absorption and separation of charge carriers. The doping activates the photoreduction with advanced reaction kinetics on the non-polar modified surface, presenting six times the yield (CO and CH_4) devoid of any detectable H_2 relative to the bare g-C_3N_4 under similar conditions. This is because of the facile adsorption of the non-polar adsorbate on the modified adsorbent.[204]

Forming heterojunctions with other photocatalysts is a widely applied strategy to encourage charge separation and thus improve the overall catalytic performance. For instance, the MOF-based/g-C_3N_4 photocatalytic system is a versatile and promising means of promoting photocatalytic efficiency for CO_2 reduction owing to its large surface area and unique porous structure.[205] In a recent study, the NH_2-MIL-101(Fe)/g-C_3N_4-X (MCN-3) heterosystem bearing coordinated unsaturated metal sites and an amino functional group was developed where a solid–gas interfacial route emerges in between the adsorbate and photocatalyst, which boosts the CO_2 adsorption ability besides selectivity, generating CO 6.9 times higher than pristine g-C_3N_4 under visible light irradiation.[203] Fig. 15 shows the morphology of bare g-C_3N_4 with a sheet-like agglomerated architecture. The TEM image (Fig. 15d) exhibits a wrinkled lamellar structure with cured layers composed of pores, whereas NH_2-MIL-101(Fe) (Fig. 15b and e) gives an octahedral morphology with a smooth surface. There is not much distinct morphological change that occurs after the formation of heterostructures indicating the uniform dispersion of g-C_3N_4 particles into the octahedral crystals (Fig. 15c and f).

Carving metal oxides such as TiO_2, ZnO, Fe_2O_3, SnO_2, and WO_3 into thin atomic layers unveils a new arena of hidden exotic properties, including rich reactive sites with a better charge carrier transport and efficient light absorption besides natural resistance to oxidation.[206,207] Among these promising 2D materials, ZnO sheets are benign and highly stable, becoming a non-polar graphene-like structure (g-ZnO) when the thickness gets reduced into a few layers in which the electronic structure is immensely dependent on the number of layers. In a study, the concept of steering the quantum confinement effect in the out-of-plane direction by engineering the interlayer coupling and surface activity of ultrathin films was examined to discover the film thickness

of materials. In their study, the effect of thickness from the bulk to a monolayer on photocatalytic reduction of CO_2 by ZnO was studied through DFT calculations.[208] One of the most chemically stable, environmentally sound and highly recognized photocatalysts is TiO_2, challenged with limited redox ability and a short light response range that can be tackled by forming vastly recommended heterojunctions. Recently He et al. came up with a Ti_3C_2 MXene quantum dot decorated 2D/2D TiO_2/C_3N_4 core–shell photocatalyst with a boosted CO_2 reduction activity generating CO and CH_4 as products with thrice the CO evolution rate compared to its pristine forms. Here, Ti_3C_2, usually a renowned 2D layered MXene featuring a fascinating work function and reduced activation energy for CO_2 reduction, acts as a potent co-catalyst in 0D form, with most of the properties similar to its 2D counterparts.[209] Lately, the potential of 2D MXenes as co-catalysts for an efficient photocatalytic CO_2 reduction was verified, which has been attributed to their smooth conductivity, rich active sites, and enlarged specific surface area.[210]

2D metal chalcogenides such as MoS_2, WS_2, $MoSe_2$, WSe_2, SnS_2, etc. are versatile materials that can be candidates for photocatalysts and non-noble metal co-catalysts considering their catalytic activity, availability, and affordability. They are generally utilized in H_2 production but are now starting to be applied in the field of CO_2 photoreduction.[179,211,212] The superior photocatalytic activity is claimed by MoS_2 nanosheet-covered TiO_2 fibers with a narrow bandgap and tuneable conduction band. The proposed material has an excellent photosensitizing effect originating from the presence of MoS_2 nanosheets, which generated a better yield of methane and methanol products.[213] Correspondingly, a WSe_2–graphene–TiO_2 ternary system was fabricated via a simple ultrasonic technique and the influence of WSe_2 and graphene nanosheets on the bandgap of TiO_2 was found, enhancing its photocatalytic performance under UV/Vis light.[214] In a similar study, a SnS_2/TiO_2 based 2D–2D heterojunction photocatalyst was prepared hydrothermally by depositing ultrathin SnS_2 nanosheets onto titania nanosheets. The so-formed photocatalyst produced methane with a yield of 23 $\mu mol^{-1}\ g^{-1}\ h^{-1}$, which is 20, 10, and 9 times higher than pristine titania, titania nanosheets, SnS_2 nanosheets, respectively, indicating the importance of metal chalcogenides as co-catalysts in photocatalysis.[215]

A developing category of anionic clays, namely, layered double hydroxides (LDHs), are reliable CO_2 reduction photocatalysts with a high sorption capacity for adsorbates between the layered space and flexible catalytic properties with respect to the chosen metal cations.[216,217] Amidst quite a few LDHs, Zn–Al LDH reduces CO_2 to CO, while Cu-containing LDH promotes an efficient reduction to produce methanol. More incredible performance is evident with the collaboration of another 2D material like g-C_3N_4. For instance, a heterojunction between NiAl-layered double hydroxide (NiAl-LDH) and g-C_3N_4 nanosheets was engineered via a simple in situ hydrothermal method.[218] The system exhibited the highest CO evolution rate of 8.2

1718 | React. Chem. Eng., 2021, 6, 1701–1738

This journal is © The Royal Society of Chemistry 2021

μmol h^{-1} g^{-1}, which is five times better than pristine g-C$_3$N$_4$ and nine times better than the pure NiAl-LDH without the presence of any sacrificial agents owing to the synergic effect between the two nanosheets. Besides the effective interfacial contact due to the 2D/2D architecture the catalyst showed arrested recombination, prominent charge carrier transport to the surface and CO$_2$ adsorption rate. Recently a study highlighted the capability of LDH-based photocatalysts in the arena of photocatalytic CO$_2$ conversion, projecting their excellent physicochemical and electrical properties. Due to the favourable redox chemistry ascribed to its 2D structure, the LDH material enriched with surface hydroxyl groups providing basicity, better visible-light harvesting ability, and reliable stability, becomes a suitable choice for coupling with other 2D materials for an innovative photocatalysis.[194]

Besides the photocatalysts mentioned above, a few more developing 2D materials are yet to be explored more for CO$_2$ reduction. For instance, h-BN nanosheets; covalent triazines having better stability, abundant nitrogen content,[219] efficient visible light harvesting, and a tuneable bandgap;[220] and black phosphorus with a flexible bandgap, high exciton mobility, *etc.*,[221] are examples. Unlike typically used catalysts such as graphene and g-C$_3$N$_4$, hexagonal boron nitride (h-BN), a honeycomb-like 2D material, exhibits ionic properties endorsing directional transfer of electrons to the adsorbate, promoting the active carbon species. An oxygen atom-tailored ultrathin BN nanosheet was engineered to improve the optical absorption and adsorption efficiency of the photocatalyst. Contrary to the normal adsorption process, CO$_2$ is chemisorbed onto the catalyst surface, enabling a continuous electron delivery, CO$_2$ activation, and interfacial interaction which helps to decrease the activation energy of the transformation process. The reported rates of the products (H$_2$ and CO) were 3.3 and 12.5 μmol g^{-1} h^{-1}, respectively, which can be considered a pioneering work in the rational design of metal-free photocatalysts.[196] Likewise, in a recent study, black phosphorus and a covalent triazine framework (CTF) have been devised *via* self-assembly, which enhanced the selectivity for CO$_2$ reduction to methane over CO. A strong interaction between CO and the catalyst surface prevents the desorption of CO, which helps in the further reduction to methane, and this is a novel strategy for selective and efficient catalysis.[222] To conclude, among many challenges, a key obstacle in developing an ideal and efficient photocatalyst is that only a single electron is excited by a photon aside from deficient solar light harvest. It invokes a dire need for attention and action in the coherent architecture of a perfect photocatalyst which can be viewed as the most reliable and economic approach in reducing the globally threatening CO$_2$ and producing green fuels.

4.4 Electrochemical CO$_2$ conversion

The electrochemical process has gained substantial attention in converting CO$_2$ to useful and value-added fuels and commodity chemicals (methane, CO, formic acid, methanol, ethylene, and ethanol) utilising electricity from renewable sources to resolve the energy and environmental problems and to maintain a healthy balance between energy supply and global carbon content. A large amount of activation energy is required for one-electron reduction of CO$_2$ and HER in protic media, which limits the selectivity of the electrochemical CO$_2$ reduction (ECR) process.[223,224] In addition, a well-matched equilibrium potential for the formation of CHO, CO, and COOH results in poor selectivity by inhibiting the tuning of the intermediates to the precise product.[225] Moreover, the poor solubility of CO$_2$ in aqueous solutions led to low current density. These limitations like poor selectivity,[226] high over-potential,[227] low current density,[228] and poor energy efficiency of ECR limit the industrialisation of the process.

4.4.1. Basics of electrochemical reduction of CO$_2$. The electrochemical CO$_2$ reduction process is of particular interest because of the possibility of coupling the electrochemical reaction with renewable energy resources such as solar energy and wind power.[229] Electrochemical CO$_2$ reduction reactions can be performed at normal temperature and pressure. In addition, electrochemical reactions can be easily controlled by varying the parameters such as external voltage and electrolyte.[230,231] The electrochemical CO$_2$ reduction processes are achieved *via* multiple PCET mechanisms.[232] A schematic illustration showing the production of various value-added products in an electrochemical cell *via* CO$_2$ reduction is presented in Fig. 16.

Some of the key parameters that are used to measure the performance of an electrocatalyst include the (a) overpotential (η), (b) current density, (c) faradaic efficiency, (d) energetic efficiency, (e) turnover frequency and (f) Tafel slope.[11] Overpotential is defined as the difference between the thermodynamically determined reduction potential of a reaction and the actual reduction potential value in which the reaction is experimentally observed.[233]

Faradaic efficiency is defined as

$$E_{\text{Faradaic}} = \frac{\alpha nF}{Q}$$

where α is the number of electrons transferred, n is the number of moles of the products formed, F is Faraday's constant, and Q is the charge passed.[234] Turnover frequency (TOF) represents the activity of the material per catalytic site. The value of the Tafel slope provides an idea of the rate-determining step (RDS) and suggests the reaction pathway involved.[235] According to practical scenarios, an overpotential of around 100 mV is required to achieve sufficient reaction rates. Consequently, cell voltages usually surpass the formal reduction potential values of the overall reaction.[233]

4.4.2. Recent progress in ECR of CO$_2$ using 2D materials. In recent years, research work has been keenly pursued to develop stable, energy-efficient, and low-cost electrocatalysts to promote the kinetically sluggish ECR process.[236–238] In

This journal is © The Royal Society of Chemistry 2021

React. Chem. Eng., 2021, **6**, 1701–1738 | **1719**

view of this, a wide variety of catalysts including TMDCs,[239,240] MXenes,[241] carbon-based materials,[242] MOFs,[243,244] metal-based complexes,[245] single atom catalysts,[246] etc. have been developed, and in this section, we will focus on the ECR process using 2D nanomaterials. The layered 2D materials with stronger in-plane chemical bonding interactions possess abundant active sites and more exposed active edge sites, which paves the way to achieve highly efficient catalysts. An atomic level investigation of catalytic mechanisms can be analysed based on the well-defined structure of the 2D nanosheets.[211] Homogeneous as well as heterogeneous catalysts have been used for the activation of the reduction process in ECR processes.[247] Even though good product selectivity and high efficiency can be achieved by homogeneous catalysis through controlling the active site of the catalyst, these systems suffer from drawbacks of high cost, toxicity, low stability and a difficult post-separation process.[248] On the other hand, heterogeneous nanocatalysts have gained a significant level of attention for their high activity and stability with a large active surface area.[249] The catalytic activity can be evaluated by parameters including current density, onset potential, overpotential faradaic efficiency and turnover frequency. The homogeneous electron transfer between the electrode and electrolyte is the main principle behind electrocatalysis. So, current density (amount of current per unit area) is a necessary parameter in the electrocatalysis process. The onset potential is the voltage required to reach a current at which the reaction starts. An efficient catalyst reduces the onset potential and power consumption. The overpotential is the difference between the actual reaction potential and thermodynamic potential that is the additional voltage required to overcome the resistance due to collisions between ions during the transfer of ions from the bulk to the electrode surface. The selectivity and efficiency of an ECR process can be analysed by faradaic efficiency.[250]

Recently, 2D graphene has gained much attention as a promising candidate for CO_2 ECR due to its excellent physical, electronic, and mechanical properties.[24,25,251] The studies on graphene-based materials reveal that doping of graphene with heteroatoms like boron, phosphorous, nitrogen, etc. shows better ECR efficiency than pristine graphene. As we already discussed, during the process the selectivity of CO_2 ECR over the hydrogen evolution reaction (HER) is a significant concern. In a study the development of porous Zn NPs wrapped with thin rGO layers for selective CO_2 ECR over HER was reported. They found that the current density for the CO production of the pristine ZnO catalyst remains unchanged while the current density for the HER process selectivity is suppressed upon the incorporation of rGO layers. The suppression is tuned by varying the amount of rGO in the catalyst and 94% FE is achieved. The decoupling of the HER from CO_2 ECR is due to the fast proton consumption and low bulk concentration of protons upon increased rGO coverage in the catalyst.[252] Later, the achievement of better activity and selectivity towards CO_2

reduction on metal and nitrogen co-doped graphene via first-principles calculations was reported. The Co and N co-doped graphene with a nitrogen coordination number of one to three possess poor selectivity towards CO_2 reduction over the HER. When the coordination number reaches five, the selectivity is found to be higher for CO_2 reduction to CO than the HER. This result implies that the coordinative environment of metal atoms significantly influences the activity of the catalyst for both CO_2 reduction and the HER.[253] These first principles calculations provide useful information to engineer active and selective catalysts for CO_2 reduction to CO. The stability of the electrocatalyst is another concern for the ECR processes. A highly stable dual-atom Ag_2/graphene catalyst was developed with a CO faradic efficiency of up to 93.4% with a current density of 11.87 mA cm^{-2} at −0.7 V and exhibited excellent stability for more than 36 h. The interaction of Ag atoms with carbon and oxygen atoms of CO_2 stabilises the CO_2 adsorption intermediate and thus reduces the barrier for the formation of the *COOH intermediate.[254] Immobilisation of Ni^{2+} ions on N-doped graphene via a facile ion adsorption process was carried out. The metal immobilization on N-doped graphene creates cyclam-like moieties, enhancing the electrocatalyst's selectivity and activity for CO_2 reduction. The catalyst achieves 92% CO production faradaic efficiency at 0.68 V with a current density of 10.2 mA cm^2.[255] In another study, the effect of bismuth (Bi) nanoparticle support interaction in rGO nanosheets on ECR of CO_2 to formate has been studied. The Bi/rGO synthesised by the hydrothermal method shows two times higher faradaic efficiency for value-added formate generation when compared to physically mixed Bi/rGO samples. This reveals that the Bi support interactions boost the CO_2 reduction by altering the electronic structure and interfacial electron transfer between Bi and graphene.[256] Recently, many publications related to graphene-based electrocatalysts have been reported, revealing that graphene-based materials may shed new light on engineering efficient electrocatalysts for CO_2 reduction.

Ultrathin 2D TMDCs have been widely used for energy related electrocatalysis including H_2 evolution, CO_2 reduction, O_2 reduction/evolution, etc. due to their exceptional electronic and chemical properties. TMDCs provide a good platform for the study of the structure–performance relationship at the atomic level.[257] The CO_2 reduction performed using WSe_2 starts at an extremely low overpotential of 54 mV with a current density of 18.95 mA cm^{-2} and CO reduction faradaic efficiency of 24%. On comparing the results with bulk Ag and Ag nanoparticles, the TMDC possesses higher performance for ECR of CO_2. The DFT calculations show that COOH* intermediate formation using WSe_2 is exergonic due to the strong binding interactions with the metal edge sites of the TMDC which is absent in Ag nanoparticles (endergonic). So the formation of CO is kinetically more favourable in WSe_2 compared to Ag nanoparticles.[258] Ultrathin $MoTe_2$ layers have been fabricated for the ECR of CO_2 to methane with an FE of 83% and a

1720 | React. Chem. Eng., 2021, **6**, 1701–1738

This journal is © The Royal Society of Chemistry 2021

durable activity for greater than 45 h at a relatively high current density of 25.6 mA cm^{-2} at an applied potential of −1.0 V. This result reflects more exposed active sites in the MoTe$_2$ layers, which help to achieve improved efficiency for ECR.[259] Doping the edge atoms of TMDCs with suitable dopants can alter the electronic properties to enhance the electrocatalytic performance. Abbasi et al. synthesised Nb and Ta doped MoS$_2$ and the prepared Mo$_{0.95}$Nb$_{0.05}$S$_2$ structure showed the lowest onset potential and highest CO$_2$ reduction activity. This can be attributed to a decrease in binding strength of Mo edge atoms to CO with Nb doping.[260] The kinetically slow CO desorption process can be promoted by doping with V, Zr, and Hf. The factor that influences the catalytic activity is the closeness of the dopant to the active Mo site rather than the concentration of the dopant used. DFT calculations suggest that the d-band center energy from the Fermi level controls the electronic properties and the CO desorption mechanism. The closer the d-band to the Fermi level, the weaker the CO adsorption. Doping of MoS$_2$ with V, Zr and Hf leads to shifting of d-band centers to the Fermi level and makes CO desorption easier.[261] Undoubtedly, these results show the attractive effect of TMDs for electrocatalysis applications.

MXenes, 2D transition metal carbides, and nitrides provide an active platform for selective CO$_2$ ECR owing to the presence of mixed surface terminations.[262,263] Analyses on −OH and −F terminated MXenes for CO$_2$ ECR were carried out. It was reported that the H atom of the −OH functional group present in Sc$_2$C(OH)$_2$ and Y$_2$C(OH)$_2$ assists in forming stable intermediate structures, thus lowering the overpotential.[264] They also analysed Ti and Mo-based MXene catalysts by combining theoretical and experimental methods for CO$_2$ reduction with an −F terminal functional group. The CO$_2$ reduction of Ti$_2$CT$_x$ and Mo$_2$CT$_x$ MXene results in formic

acid production with an FE of 56% at −1.8 V on Ti$_2$CT$_x$.[264] The terminal functional group plays a vital role in the selectivity of the reduction process. DFT simulations predict that the −F termination destabilises COOH* leading to a more negative limiting potential for CO$_2$ reduction. Ti$_2$CT$_x$ (HF) with large −F terminal groups shows inadequate CO$_2$ reduction, while Ti$_2$CT$_x$ (KF-HCl) with smaller −F terminal groups shows higher selectivity for CO$_2$ reduction and better efficiency. Chen et al. have investigated M$_2$XO$_2$ MXenes with carbon/nitrogen and transition metal vacancies. The vacancies present in the catalyst influence the CO$_2$ reduction by favouring a strong binding interaction of fragment type intermediates (e.g. *COOH, *CHO), allowing the tuning of overpotential.[265] More research works are ongoing in this area to develop MXenes with acceptable cost for energy generation and conversion applications.

MOFs are another class of materials assembled by metal clusters/ions as nodes and ligands as linkers that have gained much attention for ECR to value-added chemicals. Permanent porosity, adjustable pore size, coordinatively
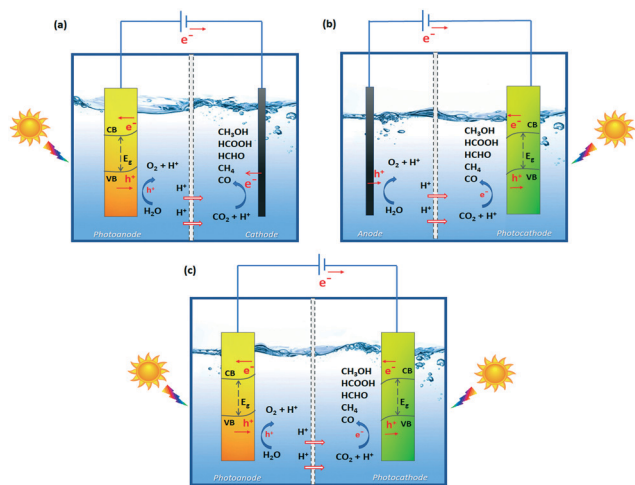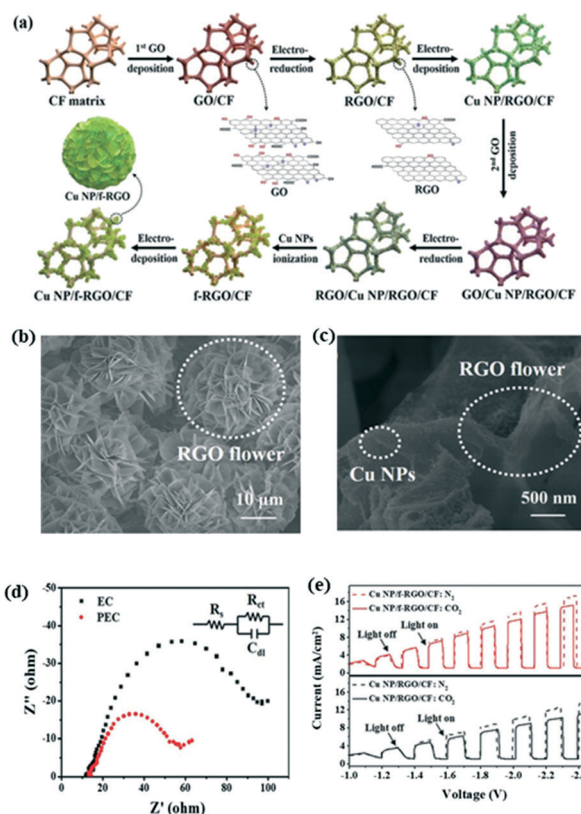

Fig. 18 PEC electrode based on graphene. (a) Schematic of the preparation of 3D flower-like reduced graphene oxide (f-rGO) modified with Cu NPs and deposited on Cu foam (Cu NP/f-rGO/CF electrode); SEM images of (b) f-rGO/CF and (c) Cu NP/f-rGO/CF electrodes; (d) EIS – Nyquist plots under PC, EC, or PEC conditions for the Cu NP/f-rGO/CF electrode in the Pt-TNT photoanode-driven PEC cell (inset shows the scheme for the circuit followed for fitting EIS); (e) linear sweep voltammetry curves of Cu NP/f-rGO/CF and Cu NP/rGO/CF. "Reproduced from ref. 304 with permission from Wiley-VCH, copyright 2020".

Fig. 17 Schematic representation of a PEC cell with a two-electrode system separated by an exchange membrane converting CO$_2$ to chemical fuels (a) with an illuminated photoanode and cathode, (b) with an anode and illuminated photocathode, and (c) when both the photocathode and photoanode are illuminated.

This journal is © The Royal Society of Chemistry 2021

React. Chem. Eng., 2021, 6, 1701–1738 | 1721

unsaturated metal sites, high surface area, *etc.* help to achieve free diffusion of reactants through MOF channels and readily facilitate the reaction over the open metal active sites. The efficiency of electrochemical reactions can be determined by the electron coupling interfacial interactions provided by the highly accessible metal–ligand junctions of MOFs.[266] The possibility of electrochemical conversion of CO_2 to methanol using DFT combined with the computational hydrogen electrode model for the 2D Fe–hexaaminobenzene MOF was explored. They found that $Fe_3(HAB)_2$ containing Fe–N_4 sites is the most promising candidate for catalysing CO_2 into hydrocarbons through CO_2 → *COOH → *CO → *CHO → *CHOH → *CH_2OH with a free energy change of 0.69 eV, and the activation energy barrier is 1.36 eV.[267] In a study, a bismuth-based metal–organic framework as a pre-catalyst, which undergoes structural changes to form bismuth-based nanoparticles for highly active and selective CO_2 reduction towards formate formation, was reported.[268] The efficiency of CO_2 reduction can be enhanced by ligand doping. Zn-based MOFs of zeolitic imidazolate framework-8 (ZIF-8) are doped with a strong electron donating molecule, 1,10-phenanthroline. The electron-donating nature of the dopant enables the transfer of electrons from phenanthroline to the sp^2 C atoms of the imidazole ligand, and facilitates the formation of the COOH* intermediate, thus enhancing the faradaic efficiency.[269] Cobalt porphyrin was anchored into the Zr-BTB MOF to increase the utilisation of active sites for CO_2 reduction and the catalyst shows ultrahigh turnover frequency. The post-modified electrocatalyst with *p*-(aminomethyl) benzoic acid (PABA), *p*-sulfobenzoic acid potassium (PSBA), and *p*-sulfamidobenzoic acid (PSABA) induces the steric effect and thereby reduces the activity of the HER. The modifiers attached to unsaturated Zr_6 sites with good coverage are responsible for the steric effect.[270] A bimetallic layered MOF with copper-phthalocyanine as a ligand (CuN_4) and zinc-bis(dihydroxy) complex (ZnO_4) as a linkage (PcCu-O_8-Zn) was developed with a faradaic efficiency of 88% and high selectivity towards CO. Both experimental and theoretical calculations reveal that CuN_4 facilitates the protonation of adsorbed CO_2 while zinc-bis(dihydroxy) complexes act as the catalytic sites for the ECR process.[271] Overall, MOF-derived materials with a highly active metal site and good electrical conductivity are a good platform for electrocatalytic CO_2 reduction in the near future. COFs with tuneable catalytic centers provide a highly exposed surface area and active sites suitable for the CO_2 reduction reaction. A 2D layered structure with eclipsed stacking leads to insufficient use of active sites, thus leading to reduced activity towards CO_2 reduction. This problem can be avoided by exfoliating of the layered structure to a large surface area with high accessibility to more active sites. Zhu *et al.* designed covalent organic frameworks by the Schiff-base condensation reaction of metalloporphyrin and TTF. Remarkably, the FE was found to be 91.3% at −0.7 V and after exfoliation, the nanosheets with 5 nm thickness exhibit 100% FE at −0.8 V.[272]

Researchers have been focused on the development of non-noble earth-abundant catalysts for CO_2 reduction. In this regard, tin, lead, and bismuth have gained much attention due to their high stability and selectivity. Among these, bismuth possesses a wide bandgap, good electrical conductivity, rich valence electrons, and large theoretical capacity. Bismuth catalysts were developed by *in situ* restructuring of 2D bismuth oxyhalides. The electrocatalyst shows an FE of 90% for formate formation with a current density of 200 mA cm^2.[273] Yang *et al.* synthesised a stable free-standing Bi monolayer (bismuthene) to demonstrate high electrocatalytic CO_2 reduction activity towards formate formation. The thin monolayer of Bi (111) has a unique compressive strain that shows better catalysis activity than thicker nanosheets. The more exposed (011) facet of thicker Bi nanosheets strongly binds to intermediates and results in poisoning; this lowers the activity of the thick nanosheets of Bi.[274] Another 2D material, black phosphorous, is used for electrocatalytic reduction of CO_2 to formic acid. The catalyst shows a FE of 25.8% at −1.3 V. The activity is enhanced to 92% at a lower potential of −1.0 V by loading Bi metal. The black phosphorous provides a large surface area and improves the kinetic activity for CO_2 reduction.[275] Hexagonal boron nitride is a structural analogue of graphene widely used for oxygen reduction reactions due to its magnetic properties and wide and tuneable semiconducting band gaps. DFT calculations were carried out to investigate the reduction process of C-doped boron nitride nanoribbons (BNNRs) and line-defect (Ld)-embedded zigzag BNNRs with C_2 (Ld-C) and B_2 (Ld-B) dimers. Both boron and carbon atoms provide highly active sites for CO_2 reduction.[276] In a study, the synthesis of Cu(I) supported BN sheets for CO_2 ECR to acetic acid was reported. The catalyst shows an FE of 80.3% with a current density of 1.39 mA cm^{-2}. The high activity can be attributed to the synergistic effect of BN, the copper metal centre and the N-based ligand.[277] Pd catalysts are widely used for CO_2 reduction due to their distinguishable capability of converting CO_2 selectively into formate or CO. The selectivity depends on their surface binding abilities towards CO* or COOH*. The pristine Pd nanosheets possess a more exposed (111) facet, while reconstruction into a crumpled sheet-like structure results in a more exposed (100) facet with good electrocatalytic activity. The (100) facet exhibits a lower binding affinity to CO, facilitating the CO_2 reduction to CO.[278] Metal oxides such as ZnO, TiO_2, RuO_2, Co_3O_4, SnO_x, *etc.* have been used as active electrocatalysts for CO_2 reduction. Among these, SnO_x is considered to be active in the reduction of CO_2 to HCOOH. Nanoflakes of amorphous SnO_x were fabricated by a mass production method from liquid metals. These nanoflakes were further modified with single atoms of Bi and show high selectivity of more than 90% towards HCOOH production.[279]

4.5 Photoelectrochemical conversion of CO_2

Conversion of CO_2 by photoelectrochemical (PEC) methods is a combination of photocatalytic and electrocatalytic conversions. This approach minimized the disadvantages of

1722 | *React. Chem. Eng.*, 2021, **6**, 1701–1738

This journal is © The Royal Society of Chemistry 2021

both technologies, combined their advantages, and widened the range of catalysts. Compared to the particle suspension methodology in photocatalytic conversion, PEC reduction based on photoelectrodes has enhanced the charge separation and provided high solar conversion efficiency. Different research groups have proposed several hypotheses regarding PEC conversion of CO_2 that include complex multistep reaction pathways and shared intermediates.[280–285] On excitation of the photoelectrode with photons of suitable energy ($E_g \leq h\nu$), electron–hole pairs are generated which independently migrate to the cathode and anode to undergo redox reactions. Photogenerated electrons at the cathode are engaged in the reduction and conversion of CO_2 to solar fuels, while holes take part in the oxidative splitting of water (converting H_2O to O_2). A typical 2-e$^-$ reduction pathway initiates with the formation of the carbon dioxide anion radical ($CO_2^{\cdot-}$) which gets adsorbed onto the electrode. H$^+$ in the aqueous medium then reacts easily with the O atom of the adsorbed $CO_2^{\cdot-}$, as the C atom is bonded to the electrode surface, leading to the formation of CO_2H_{ads}. The bond breaking in $CO_2^{\cdot-}$ is more facile due to its bent structure compared to the linear geometry of CO_2. CO_2H_{ads} formed thereafter gets reduced to CO, or may undergo successive reactions with e$^-$ or H$^+$ to give other value-added products like CH_3OH, CH_4, *etc.*[286] Hence effective photoconversion efficiency is highly required for effective PEC reduction of CO_2 due to the large consumption of electrons and holes. Henceforth, various strategies are conducted to modify the photoelectrodes, *viz.*, engineering of the band gap for effective light-harvesting, construction of hierarchical nanostructures, control of catalyst morphology, utilization of multi-functionalized homojunctions or heterojunctions, and co-catalyst loadings.[287–291] Most of the PEC electrodes are prone to photo-corrosion which results in short-term usability. In most cases, catalytic layers of TiO_2 and noble metals like Pt, or Ir, usually fabricated by atomic layer deposition (ALD), are often complex and expensive for deployment.

4.5.1. Fundamentals of photoelectrochemical reduction. PEC CO_2 fixation can be treated as an artificial photosynthesis strategy because it imitates the natural photosynthesis reaction.[25] Photosensitizers such as chlorophyll harness solar radiation and perform CO_2 fixation in natural photosynthesis, whereas in PEC CO_2 reduction, light radiation and electricity are used to drive the CO_2 transformation forward.[292,293]

A schematic representation of a PEC cell having two compartments separated by a proton exchange membrane for CO_2 reduction is given in Fig. 17. In general, p-type semiconductors are used as photocathodes in a PEC system, and n-type semiconductors function as anodes.[294] Upon light irradiation, electron–hole pairs are generated in the photocathode. The band bending phenomenon observed at the electrode–electrolyte interface is responsible for separating photogenerated electrons and holes. The application of an external potential to the system intensifies

the band bending and increases the electron–hole separation. The photogenerated electrons participate in the CO_2 reduction process at the electrode–electrolyte interface.[295]

The solar-to-fuel (STF) conversion efficiency of the PEC system is calculated as

$$\text{STF} = \frac{r_{\text{fuel}} \ (\text{mmol of fuel per s}) \times \Delta G^{\circ} \ (\text{kJ mol}^{-1})}{P_{\text{solar}}(\text{mW cm}^{-2}) \times \text{area} \ (\text{cm}^2)}$$

where r_{fuel} is the quantity of chemical fuel produced per second, and ΔG° is the Gibbs free energy associated with the conversion of CO_2 to fuels. P_{solar} is the power density of the light source used, and the area represents the photoelectrode area under light irradiation.[296]

4.5.2. 2D materials in the PEC reduction of CO_2. 2D materials can be effectively employed for the construction of stable, cost-effective, highly efficient catalytic layers. As a 2D material for photoelectrodes, graphene has received considerable attention for PEC reduction of CO_2 due to its π–π conjugation that promotes e$^-$ transfer and enhances CO_2 adsorption. A remarkably strong π–π interaction of CO_2 or $CO_2^{\cdot-}$ is established with graphene, as CO_2 contains a delocalized π–π conjugation, while graphene has an extensive 2D network of π conjugation.[297] This synergistic interaction shows the more significant adsorption of CO_2 over the photoelectrode surface. Moreover, graphene has a large surface area of 2630 m^2 g^{-1}, thus providing many active sites for CO_2 adsorption and reduction.[298,299] The availability of un-adsorbed $CO_2^{\cdot-}$ is reduced in the presence of the graphene photoelectrode, which would otherwise lead to the formation of formate ions by the action of the nucleophilic carbon atom of $CO_2^{\cdot-}$ as a Lewis base.[300] The hydrophobic nature also makes the graphene surface more controllable to facilitate CO_2 reduction rather than transferring electrons to the H_2O molecule.[301] When a strongly coupled host–guest rGO/GO nanohybrid is fabricated by stacking the layers one above the other, the bandgap is lowered to 2.58 eV, enhancing the PEC performance.[302] While administering graphene to the electrode, usually using a polymeric binder, it often undergoes agglomeration due to the van der Waals forces acting between the layers.[303] Recently, the self-agglomerating nature of graphene has been demonstrated to be suppressed by the design of a 3D flower-like reduced graphene oxide (f-rGO) modified with Cu NPs and deposited on Cu foam (Fig. 18).[304] The so-formed CuNP/f-rGO/CF fabricated by electrochemical methods acted as a dual-role photoanode for PEC conversion of CO_2 to CO, C_2H_4, HCOOH, CH_3COOH, and C_2H_5OH. Decomposition of water at the photoanode delivers e$^-$ and H$^+$, simultaneously with the anode's photovoltage compensation, which is reflected with a more negative cathode potential desirable for the conversion of CO_2. Due to its characteristic physicochemical properties, graphene, when integrated with other semiconductors such as TiO_2, Si, $BiWO_6$, Cu_2O, and other metal NPs, may form a Schottky barrier, leading to effective separation of charge carriers.[305–307]

This journal is © The Royal Society of Chemistry 2021

React. Chem. Eng., 2021, **6**, 1701–1738 | 1723

Replacing noble metal catalysts, 2D TMDCs such as MoS_2, $MoSe_2$, and WS_2 have gained considerable attention as PEC electrodes, due to their robust stability in acidic electrolytes, layered structure with basal planes being less permeable, and edges acting as active sites of PEC reductions.[308] Also, monolayer and bulk MoS_2 have a bandgap of 1.88 eV and 1.29 eV, respectively,[309] with the conduction band minimum higher than the redox potentials of most CO_2 conversions. Different defect sites of MoS_2 were analysed, and compared with the grain boundaries, edges and S vacancies (7–10% optimal density of vacancies) are the most catalytically active centers.[310] Simultaneously, Mo-terminated edges of layer-stacked vertically aligned bulk MoS_2 exhibited the highest rate of CO_2 reduction while as demonstrated for 1-ethyl-3-methylimidazolium tetrafluoroborate (EMIM-BF_4), the IL is more selective for CO formation than water splitting.[311] Due to significant variance in work functions, the deposition of n-type MoS_2 onto p-type semiconductors like Si results in high induced electric fields, thereby enhancing the charge transfer between the p-type semiconductor through MoS_2 and the solid/electrolyte interface.[308] In addition to being an effective PEC catalyst, MoS_2 can also act as a protective layer stabilizing the photoelectrode. However, thin-film fabrication over the semiconductor electrode is rather tricky. It is usually achieved by the ALD technique, where the thickness/morphology is engineered by the number of cycles and deposition conditions. Jang *et al.* successfully introduced thermolysis as a fabrication method for developing thin films of MoS_2 over a Si substrate, using a precursor solution of $(NH_4)_2MoS_4$. The film thickness over the range of 5–29 nm was tuned by changing the precursor solution concentration. Moreover, among the different phases of 2D TMDCs, the 1T metallic phase usually exhibits enhanced PEC performance compared to 2H or 3R phases.[312]

Inspired by graphene and various graphene analogs, the fabrication of photoelectrodes using 2D ultrathin van der Waals (vdW) heterostructures forming an ensemble of heterojunctions is also interesting and gaining attention. Such 2D vdW heterostructures have ultrafast transfer of charge carriers and robust carrier mobility. The MoS_2/graphene photoelectrode can have improved PEC performance when compared individually to MoS_2 or graphene.[313] Promoted PEC reactions due to enhanced charge transfer by reducing the potential barrier are observed when a heterojunction photoelectrode of MoS_2/monolayer O-g-C_3N_4 was developed.[314] An increase in the intrinsic activity with the enhancement in PEC active sites was reported through the formation of the graphene/h-BN heterostructure.[315] Furthermore, these 2D nanostructures can be combined with other 1D or 3D nanomaterials forming complex heterostructures, and accordingly can engineer the structural and functional designs for PEC cells and other optoelectronic devices.

Only a few reports have been focused on 2D materials for the PEC reduction of CO_2. The endless number of untested 2D nanomaterials and their heterojunctions, or functionalized 2D materials, infers that absolute materials are still waiting to be explored for PEC CO_2 conversion. An in-depth understanding of the adsorption of CO_2 at the active sites of the photoelectrode, the activity of these active surface sites to convert CO_2, and the effective transfer and utilization of charge carriers at the electrode interfaces is required to realize state-of-the-art PEC-based energy conversion systems. Even though there are such theoretical studies on 2D nanomaterials for PEC conversion of solar energy, they have usually employed ultrathin single-layer models, of which large-scale synthesis is highly challenging. MXenes, the new upcoming family of 2D transition metal carbides, nitrides, or carbonitrides, are the future two-dimensional materials for the PEC reduction of CO_2. Besides, until now, the PEC of CO_2 is still far from the requirements of being commercialized.
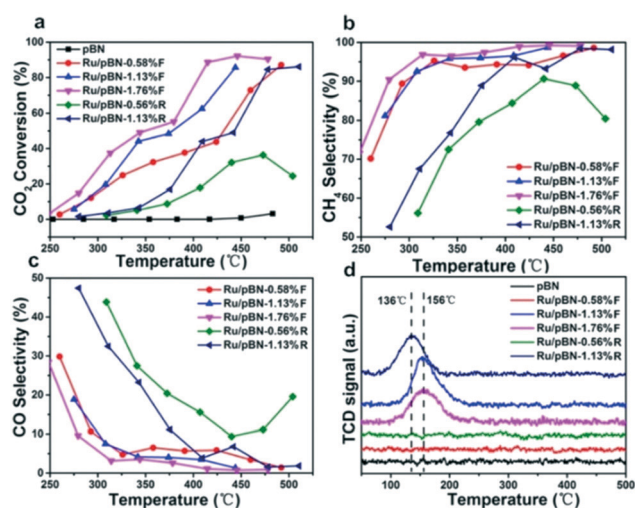

Fig. 19 Trend in CO_2 hydrogenation by Ru/pBN-*x*F and -*x*R (a); effect of temperature on CO_2 conversion (b); CO selectivity at varied temperatures (c); H_2-temperature-programmed reduction of all the samples (d). "Reproduced from ref. 330 with the permission from American Chemical Society, copyright 2019".
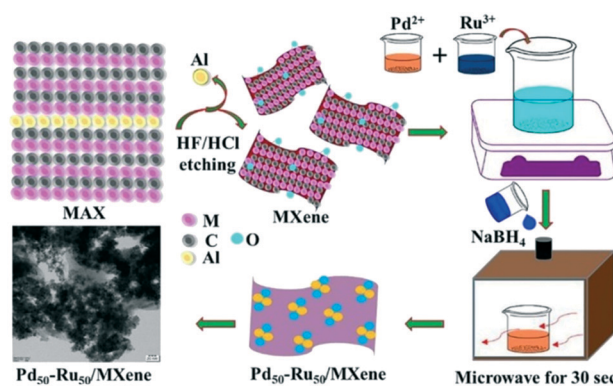

Fig. 20 Schematic illustration for the preparation of MXene from MAX and synthesis of Pd_{50}–Ru_{50}/MXene *via* a microwave process for 30 min. "Reproduced from ref. 331 with permission from Elsevier, copyright 2021".

1724 | *React. Chem. Eng.*, 2021, **6**, 1701–1738

This journal is © The Royal Society of Chemistry 2021

4.6 Thermal conversion of CO_2

Catalytic molecules can activate the unreactive CO_2 molecules and transform CO_2 into valuable chemicals by reducing the energy barrier for the reaction. In general, a thermocatalytic CO_2 conversion strategy involves the passing of a mixture of gases (CO_2, H_2 etc.) over the catalytic surface at higher temperatures and pressure to convert CO_2 into valuable products.[316] The CO_2 to CO conversion is achieved via a reversible water gas shift reaction. Fischer–Tropsch synthesis performs the conversion of CO to hydrocarbon fuels via the water gas shift reaction. CO_2 reduction to CO in the presence of hydrogen is relatively easier to achieve with high selectivity and significant conversion efficiency. But the further conversion of CO to long-chain hydrocarbon fuels and alcohols with required selectivity is a challenging task.[317] To perform the thermocatalytic CO_2 conversion reaction, the active sites on the catalyst should be capable of injecting the

Table 3 Summary of different 2D nano-materials used for CO_2 conversion

Method	Catalyst/device structure	Reaction conditions	Products	Yield	Ref.
Photochemical conversion of CO_2	ZnO:g-C_3N_4 heterostructures	Cylindrical steel reactor, CO_2 purge time:20 min, rate: 20 mL min^{-1}, lamp: 5WUVC (254 nm)	CO, CH_4	CO: 12.73 µmol g^{-1} CH_4: 3.99 µmol g^{-1}	332
	Z-Scheme ZnO/g-C_3N_4 photocatalyst	UV irradiation at 0.4 MPa, 25 °C	CO, CH_4	CO: 70 µmol g^{-1} CH_4: 50 µmol g^{-1}	333
	NH2-MIL-101(Fe)/g-C_3N_4	300 W xenon arc lamp; circular glass fiber membrane activated at 120 °C for 12 h	CO	132.8 µmol g^{-1}	203
	Z-Scheme g-C_3N_4/FeWO$_4$	Stainless steel photoreactor, Xe lamp of 300 W, He purging (20 mL min^{-1} for 1 h)	CO	6 µmol g^{-1} h^{-1}	334
	Ti^{3+} defective SnS_2/TiO_2 photocatalyst	270 mL Pyrex reactor, simulated solar light irradiation for 4 h	CO	58 µmol g^{-1} h^{-1}	335
	Ultrafine CeO_2-decorated layered double hydroxide nanosheets	50 mL closed stainless reactor, 300 W Xe lamp	Syn gas	CO: 85 µmol g^{-1} h^{-1}	336
Electrochemical conversion of CO_2	Copper immobilized MXene	Catalyst coated glass carbon electrode as working electrode, Ag/AgCl electrode as reference electrode and carbon rod electrode as counter electrode	CH_3OH	59.1% CO_2 conversion	337
	Mo_2C and Ti_3C_2 MXenes	Ionic liquid 1-ethyl-2-methylimidazolium tetrafluoroborate electrolyte, catalyst coated glassy carbon working electrode & Ag/Ag$^+$ reference electrode	CO	90% CO_2 conversion	338
Photoelectrochemical conversion of CO_2	g-C_3N_4/ZnTe heterojunction	Recorded in 2 mM $K_4Fe(CN)_6$ with a scan rate of 50 mV s^{-1}	C_2H_5OH	Generation rate of 7.1 µmol cm^{-2} h^{-1} at −1.1 V	339
	Cu NPs modified rGO flowers deposited on Cu foam (CuNP/f-rGO/CF)	Photoelectrode separated by Nafion membrane, 0.1 m H_2SO_4 and 0.1 m NaHCO$_3$ solutions were electrolytes, light source at 365 nm with intensity ≈100 mW cm^{-2}	CO, CH_4, C_2H_4, HCOOH, CH_3COOH, C_2H_5OH	Generation rate of HCOOH highest with ~12 µmol h^{-1}	304
	Defect h-BN	—	CH_3OH	TOF of 1.52×10^{-2} S^{-1}	340
	Vertically aligned MoS_2 in EMIM-BF$_4$	Voltage swept between +1.0 and −0.764 V vs. RHE with a 15 mV s^{-1} scan rate	CO	CO_2 reduction current density of 130 mA cm^{-2}	311
	$MoSe_2$ thin films over Si substrate ($MoSe_2$/Si)	Scan rate of 10 mV s^{-1} from +0.2 V to −1.0 V voltage sweep, light irradiation with white LED USB flashlight (400–700 nm)	—	CO_2 reduction activity (0.127 mA cm^{-2}) increased by 9.3 times on light irradiation	341
Thermal conversion of CO_2	Cu–Zn supported on rGO	250 °C, 15 bar	CH_3OH	Space time yield: 424 mg g$_{cat}^{-1}$ h^{-1}; 26% CO_2 conversion	322
	Ni/rGO	240 °C, 10 bar	CH_4	Space time yield: 24.9 g kg$_{cat}^{-1}$ h^{-1}; 55.3% CO_2 conversion	323
	Ni–SiO_2/GO-Ni-foam catalyst	470 °C, 1 bar	CH_4	TOF of 0.3041 s^{-1}; 83.7% CO_2 conversion	324
	MoS_2/graphene hybrid	300 °C, 10 bar	CH_4	33% CO_2 conversion	326
	Pt/MoS_2	210 °C, 30 bar	CH_3OH	TOF: 162.5 h^{-1}	328
	MoS_2 modified with porous activated carbon	200 °C, 20 bar	HCOOH	TOF: 510 h^{-1}	329
	Ru/pBN	400 °C, 10 bar	CH_4	81.1% CO_2 conversion	330
	Pt loaded Ti_3-xC_2T_y MXene	Ambient conditions	Amides	~100% conversion	321
	Pd$_{50}$–Ru$_{50}$/MXene	150 °C, 10 bar	CH_3OH	78% CO_2 conversion with TON 2932	331

This journal is © The Royal Society of Chemistry 2021

React. Chem. Eng., 2021, **6**, 1701–1738 | 1725

electrons to the antibonding orbital of CO_2. In a thermocatalytic CO_2 conversion reaction, hydrogen is supplied as the reducing agent. The ability of the catalytic surface in dissociating the hydrogen molecule to atomic hydrogen (H*) is a critical parameter in evaluating the hydrogenation capacity of the catalyst.[318]

4.6.1. Role of 2D materials in the thermocatalysis of CO_2. Thermocatalytic conversion of CO_2 to valuable chemicals has received much attention because of its suitability for large-scale industrial applications.[319] The common thermocatalysis of CO_2 is based on the hydrogenation reaction to produce CO, CH_3OH, and CH_4. Due to the high thermodynamic and chemical stability of CO_2, a co-reactant such as H_2 with higher Gibbs free energy has been used for the facile progress of the reaction.[320] Further, suitable catalysts can reduce the activation energy and make the bond cleavage easier during the hydrogenation process to yield selective products. In this context, the relevance of single-atom catalysts is significantly high due to their atomic dispersion and unsaturated coordination. However, due to the high surface energy, they tend to form aggregates. This can be remedied by using a suitable catalyst support and creating a good interaction between a single atom and the support.[321] The role of Cu–Zn supported on rGO in the catalytic hydrogenation of CO_2 to methanol was analysed. Zn oxide was used for the better dispersion of Cu particles, and the electron transfer from Zn oxide to Cu metal creates Cu^0 and Cu^+ species, promoting the hydrogenation process. Reduced graphene oxide was used as a support material to achieve better metal dispersion with an improved surface area. The effect of reaction temperature and percentage loading of Cu–Zn on rGO was analysed to optimize the reaction conditions to maximize methanol production. The hydrogenation was carried out in a tubular stainless steel fixed bed reactor after the *in situ* reduction of the catalyst at 350 °C for 2 h followed by treatment with the CO_2/H_2 mixture for the hydrogenation process. The Cu–Zn loading of 10 wt% at a temperature of 250 °C and 15 bar pressure was identified as the optimum condition for 26% CO_2 conversion with 424 (mg g_{cat}^{-1} h^{-1}) space time yield (STY) of methanol.[322] Similarly, a Ni/rGO hybrid was used for the catalytic hydrogenation of CO_2 to methane. Transition metal catalyst Ni was selected for the selective hydrogenation of CO_2 to methane and a Ni loading of 15% on rGO results in a 55.3% conversion of CO_2 to methane with 24.9 (g kg_{cat}^{-1} h^{-1}) STY[323] at 240 °C and 10 bar pressure. In another study, a Ni–SiO$_2$/GO-Ni-foam catalyst was used for the hydrogenation of CO_2 to methane. The change in the electronic structures of Ni due to the presence of graphene or other metals could terminate the side reactions and avoid the formation of carbon deposition. Also, the incorporation of Ni into macro-mesoporous materials like silica was conducted to stabilize Ni by avoiding sintering during the process. By catalytic vapour deposition (CVD) followed by oxygen plasma treatment, GO was coated over

Ni foam, and on the top, this Ni–SiO$_2$ was deposited *via* sol–gel and hydrothermal methods. The intercalated GO layer could strengthen the interaction between Ni species and Ni-foam in the catalyst, and this helps Ni species to eliminate sintering on Ni foam. The intercalated GO layer could strengthen the interaction between Ni species and Ni-foam in the catalyst, and this helps Ni species to eliminate sintering on Ni foam. Ni–SiO$_2$/GO-Ni-foam with a surface area of 10.07 m^2 g^{-1} showed a CO_2 conversion of 83.7% with a TOF of 0.3041 s^{-1} at 470 °C and 0.1 MPa which was higher when compared to Ni–SiO$_2$/Ni-foam, GO-Ni-foam and Ni-foam.[324] In another study, g-C$_3$N$_4$ was used as a single-atom catalyst supported for the hydrogenation of CO_2 to formic acid. The use of non-noble metal atoms such as Fe, Co, Ni, and Cu supported on g-C$_3$N$_4$ was highlighted using DFT calculations. The DFT calculations reveal that the reduction of CO_2 is a two-step reaction that consists of forming a formate (HCOO) intermediate and its subsequent transformation into a formic acid product. Based on activation barriers on the rate-determining steps, the catalytic activity for the CO_2 reduction to formic acid is found to be in the order of Fe-g-C$_3$N$_4$ > Co-g-C$_3$N$_4$ > Cu-g-C$_3$N$_4$ > Ni-g-C$_3$N$_4$.[136] Ag nanoparticle (NP) decorated porous C$_3$N$_4$ frameworks (PCNFs) prepared *via* the direct carbonization of the covalent triazine frameworks (CTFs) at different pyrolysis temperatures and used for carboxylation of CO_2 and terminal alkynes under mild conditions were reported. The catalyst Ag/PCNF-700, which was carbonized at 700 °C, showed better catalytic performance due to the presence of N atoms, porosity and the presence of well-dispersed Ag NPs in the catalyst.[325]

The potential of graphene as a support material for MoS$_2$ during the hydrogenation of CO_2 was examined using experimental and DFT calculations. Graphene grafted MoS$_2$ platelets were prepared by pyrolysis of natural polysaccharides containing the (NH$_4$)$_2$MoS$_4$ precursor at 900 °C for 2 h. Graphene grafted MoS$_2$ showed better catalytic activity than bare MoS$_2$ and the catalytic activity was analysed from the 300–600 °C temperature range. Carbon monoxide (CO) and methane were the two products detected in experiments carried out with different catalysts. CO was the major product when the catalyst used was pristine graphene or MoS$_2$, whereas methane was the major product while using MoS$_2$/graphene hybrid catalysts with more than 95% selectivity. However, desulfuration of MoS$_2$ and formation of less catalytically active MoO$_3$ were evidenced under the reaction conditions.[326] In another study, the CO_2 reduction reaction of a Co atom supported on a MoS$_2$ monolayer was analysed by first principles simulation, and the preferred dispersion of Co on MoS$_2$ was evidenced. DFT calculations reveal that the CO_2 conversion to methanol proceeds through reverse water gas conversion with hydrogenation of CO to HCO as the rate limiting step. The predicted pathway for the methanol production is *CO$_2$ → *CO → *CHO → *CH$_2$O → *CH$_2$OH and *CH$_3$O → CH$_3$OH.[327] Li *et al.* have studied the effect of neighbouring Pt on the hydrogenation of CO_2 in the

1726 | *React. Chem. Eng.*, 2021, **6**, 1701–1738

This journal is © The Royal Society of Chemistry 2021

Pt anchored MoS_2 catalyst (Pt/MoS_2). The catalytic hydrogenation was carried out using Pt doped MoS_2 in 30 mL of DMF under a pressure of 30 bar. The effect of temperature on the yield and selectivity to the product was evidenced; for instance, the hydrogenation of CO_2 using the 7.5% Pt/MoS_2 catalyst yielded 0.2 mmol of HCOOH and 0.8 mmol of methanol at 150 °C, whereas 2.3 mmol of formic acid and 7.3 mmol of methanol were produced at 210 °C. The methanol selectivity got reduced during the reaction period from 95.4% to 81.3% at 150 °C and from 93.0% to 76.0% at 210 °C. Due to the quick drop in selectivity to formic acid from 70% to 30% during the initial time of the catalysis, formic acid was regarded as an intermediate product before the formation of methanol. Also, from DFT studies, it was observed that when compared to isolated Pt, neighbouring Pt monomers showed better catalytic activity due to their lower activation energy. By using isolated Pt, direct formation of methanol takes place making it the hydrogenation product; however, with the use of the neighbouring Pt monomer, methanol is generated *via* the formation of formic acid. Therefore, the study concludes that the catalyst (7.5% Pt/MoS_2) with a turnover frequency of 162.5 h^{-1} and activation energy of 124.7 kJ mol^{-1} can be an ideal candidate for catalytic hydrogenation reactions.[328] Recently, Bharath *et al.* have reported formic acid production from CO_2 hydrogenation using an economical and highly efficient MoS_2 modified with porous date seed derived activated carbon (MoS_2/f-DSAC). A turnover frequency of 510 h^{-1} was achieved by the MoS_2/f-DSAC catalyst at 200 °C and 20 bar for 15 h during the formation of formic acid.[329]

In 2D h-BN, B and N atoms can act as ligands to the metals and so for the coordination of metals to the surface of h-BN, defect engineering can be adopted for creating B and N vacancies. The immobilisation of metal atoms on the surface of h-BN for effective hydrogenation of CO_2 was first reported in the year 2019 by Fan *et al.*[330] The presence of numerous OH functional groups at the edges of h-BN (or in the porous pBN) facilitated the anchoring of Ru atoms due to electrostatic interactions.

The fixation of the Ru precursor on pBN was achieved by simple vacuum filtration of the mixture of the solution containing pBN and $[Ru(NH_3)_6]Cl_3$. Further, the immobilization of Ru on pBN was carried out by annealing at 750 °C in a 50:50 Ar/NH_3 atmosphere for 1 h. The effect of Ru loading on pBN was analysed and Ru/pBN 1.76% F with 81.1% CO_2 conversion efficiency and 98.8% CH_4 selectivity at 400 °C was obtained (Fig. 19a and b). The higher Ru loading leads to better catalytic performance like CO_2 conversion efficiency and CH_4 selectivity due to the availability of active sites in the catalyst. On the other hand, Ru/pBN-*x*R samples prepared *via* rotary evaporation showed decreased catalytic activity when compared to Ru/pBN-*x*F prepared by the filtration process due to the formation of large metal particles and showed better selectivity towards CO (Fig. 19c). The reduction temperature

measured for Ru/pBN-*x*F is ~156 °C, and that for the Ru/pBN-*x*R catalyst is ~136 °C (Fig. 19d), which indicates the presence of RuOx in Ru/pBN-*x*R. Apart from this, DFT calculations hint that the presence of low valence Ru atoms on pBN can selectively hydrogenate CO_2 to methane.[330]

Another type of 2D material used as a catalytic support for single metal atoms is MXenes. Due to their surface defects and significantly high reducing ability, $Ti_{3-x}C_2T_y$ MXenes are supposed to be an ideal choice as a support for single-atom catalysts.[321] Pt loaded $Ti_{3-x}C_2T_y$ MXene ($Pt_1/Ti_{3-x}C_2T_y$) was synthesized through a room temperature self-reduction and stabilization process. In the Pt anchored MXene sheets, the strong bond between Pt and C has been achieved due to the occupancy of Pt atoms in Ti-deficit defect sites in the MXene. The as-prepared Pt/MXene catalyst could catalyse the formylation reaction of amine in the presence of CO_2 at room temperature and ambient pressure to yield amides with a higher turnover number and high selectivity towards amides as compared to Pt particles alone as the catalyst.[321] Very recently a bimetallic Pd_{50}–Ru_{50} loaded 2D MXene was synthesized *via* a microwave process for the selective catalytic hydrogenation of CO_2 to form methanol. The scheme for the preparation of Pd_{50}–Ru_{50}/MXene is shown in Fig. 20. By removing the interlayered Al from MAX (Ti_3AlC_2) through etching with HF, MXenes ($Ti_3C_2T_x$) were prepared, and the etching process provides the sites for Pd_{50}–Ru_{50} alloy nanoparticles to get anchored on the MXene surface. The nanoparticle precursors ($RuCl_3$ and $PdCl_2$ in 1:1 ratio) were introduced to the system, and the released Pd^{2+} and Ru^{3+} ions electrostatically anchored on the MXene surface. The reduced nanoparticle alloy can prevent the re-stacking of MXene layers and lead to a high surface area system formation. The hydrogenation process involved the hydrolysis of $NaBH_4$ for facilitating hydrogen with ethylene glycol solution as the capture agent. The higher product selectivity and total turnover number (TON) were observed for Pd_{50}–Ru_{50}/MXene (99%, 2932) when compared to unmodified MXene (88%, 120) and Pd_{50}–Ru_{50} (87%, 1810) catalysts under the reaction conditions of 150 °C and 10 bar pressure for 12 h. The high TON (2932), product selectivity (99%), CO_2 conversion efficiency (78%) and methanol production efficiency (76%) of the Pd_{50}–Ru_{50}/MXene catalyst are due to the adequate amount of highly dense basic sites with a good surface area which in turn can enhance the hydrogenation of CO_2. Even after several cycles of hydrogenation, the good stability and intact morphology hint at the practical utility of the proposed catalyst.[331] To conclude, the usage of single atom catalysts is more significant in the case of thermo-catalysis and the major role of 2D materials is to act as catalyst supports and to improve the conversion rate by enhancing the surface area and availability of reactive sites of the catalyst. The 2D catalysts used for the various catalytic conversions of CO_2 are summarized in Table 3.

This journal is © The Royal Society of Chemistry 2021

React. Chem. Eng., 2021, **6**, 1701–1738 | **1727**

4.7 Defect engineering in 2D catalysts for effective CO_2 conversion

Defect engineering has been claimed to be an effective tactic that enriches photocatalytic surfaces of 2D materials with exposed active sites that align every photoinduced charge carrier into the photoreduction process directly without leaving any room for exciton recombination. Defect engineering at both the surface and at the atomic level, such as creating anion/cation vacancies, crystal distortions, pits and pores, grain boundaries, stacking faults, *etc.* directly influences the optoelectronic properties of 2D nanomaterials. Moreover, the active sites optimize the reaction rate of adsorption, activation and conversion of CO_2 to corresponding products. Recently, defect concocted 2D atomic level materials including TMDCs, LDHs, *etc.* have drawn much attention in the arena of photocatalytic CO_2 reduction. In a recent study, Li *et al.* have fabricated $CuIn_5S_8$ ultrathin photocatalysts covered with sulfur defects that excelled with nearly 100% methane selectivity owing to the active sites that surfaced on Cu and In.[342] Substantially, simple metal sulfides configured into special morphologies including hierarchical, hollow or other dimensional structures which offer more specific surface areas and pore size have proved to contribute to the augmentation of active site formation.[343] Wang's group exploited this possibility to achieve 100% CO selectivity without any cocatalyst support, by means of a hollow multi-shelled system of SnS_2/SnO_2 composed of lattice distortions. The hollow structure, apart from enabling an efficient light harvest despite the absence of any sensitizers, apparently promotes CO_2 adsorption.[344] Moreover, introduction of a non-metallic dopant and defect engineering bring about a bridge between photoinduced charge carriers and surface reactions owing to the modulation of the electronic structure. Sun *et al.* addressed the fundamental challenges in photocatalysis including poor efficiency, weak charge carrier transport, *etc.* by establishing phosphate and oxygen vacancies in the Bi_2WO_6 atomic layer and explored the fine connection between the electronic structures and output of the engineered atomic layered photocatalyst which realised a better methanol formation rate.[345] Furthermore, Xie *et al.* unveiled the facts behind the bond between defect sites and CO_2 photoreduction by designing a freestanding single-unit-cell o-$BiVO_4$ layer enriched with vanadium vacancies which created more new defect levels, resulting in the highest methanol production rate of 398.3 μmol^{-1} h^{-1} *via* defective layered photocatalysts.[346] Nevertheless, introduction of active sites is important in the case of LDH photocatalysts. Besides the possibility of tuning the catalytic electronic structure in accordance with the given metal cations, thickness reduction of LDHs can result in the formation of more surface-active sites. The work put forward by Zhang and co-workers confirmed the versatile path to enhance the photocatalytic performance by thinning ZnAl-LDH nanosheets to less than 5 nm to harvest CO in the presence of water vapour at a rate of 7.6 μmol g^{-1} h^{-1} on account of the abundant oxygen vacancies and unsaturated Zn^+ cation sites which also enabled the activation of adsorbed CO_2 molecules.[347]

Chemically stable electrocatalysts with good performance are necessary to improve the CO_2 reduction efficiency. Defect engineering in 2D materials is an obvious way to enhance the ECR process. For the first time, in 2020 Chen *et al.* employed DFT calculations for thorough analysis of defect engineering in 16 different types of O-terminated MXenes. They found that Hf_2NO_2 with Hf vacancies is the most promising defective MXene showing a low overpotential of 0.45 V. A significant change in the Fermi level created upon generation of vacancies shows a linear relationship with the binding energy change of ECR intermediates.[265] Defective graphene act as an excellent electrocatalyst in the ECR process. Han *et al.* synthesised defective graphene by the N-removal method.[348] They first synthesised N-doped graphene by annealing of pristine graphene under NH_3. The obtained N-doped graphene is again annealed at 1150 °C to get the defective graphene. They observed that the catalytic activity of the graphene was enhanced with the increase in defect concentration. The presence of defects also helps to create abundant catalytic sites and facilitates the strong adsorption of CO_2. The defect engineering in graphene improves the affinity for the reaction of intermediates by distributing local charge density uniformly. Defect engineering of 2D materials for electrolytes can also show enhanced performance for photoelectrochemical reduction of CO_2. Similar works were developed in many other fields such as water splitting and N_2 fixation, following innovative tracks on CO_2 photoreduction. However, an insightful study is yet to be carried out to expose the obscure facts on the influence of defects on photophysical properties like carrier lifetime, diffusion length, and PL intensity; photocatalytic activity and selectivity; interaction of electrolytes on the defects, to identify and quantify the exact defect among many if present, which contributes to the catalytic conversion, *etc.*

5. Challenges and prospects

5.1 Challenges and future prospects

In general, the CO_2 adsorption capacities of adsorbents are evaluated gravimetrically, which is based on the mass of the adsorbate per unit mass of the adsorbent. However, for more precise evaluation, the volumetric CO_2 adsorption capacities should be reported. Physisorption of CO_2 on an adsorbent with weak van der Waals interactions is not enough to hold the adsorbed gases due to the possibility of desorption by a minimal thermal distortion. However, very strong chemisorption of CO_2 can reduce the reusability of the material because of the requirement of tedious gas removal procedures of the sorbed gas. Therefore, materials with suitable adsorption–desorption characteristics should be developed. Even though the chemisorption or physisorption of CO_2 on 2D materials has been identified *via* spectral techniques (FTIR), detailed kinetic studies on the adsorption

1728 | *React. Chem. Eng.,* 2021, **6**, 1701–1738

This journal is © The Royal Society of Chemistry 2021

and desorption of CO_2 on 2D adsorbent surfaces are rare. Hence the parameters such as the rate of adsorption, adsorption half time, adsorption isotherms, *etc.* are yet to be identified in various systems. Even though theoretical correlations supported many experimental studies, the analysis of CO_2 adsorbed samples *via* nuclear resonance spectroscopy, Raman spectroscopy, X-ray photoelectron spectroscopy, *etc.* can deliver more information related to the species formed on the adsorbent. Since these studies are meagre, the molecular level understanding of adsorbent–adsorbate interactions is limited. Another major challenge is the inadequacy of direct capture of CO_2 from the atmosphere. This is due to low partial pressure of CO_2 in the atmosphere compared to post and pre-combustion capture processes. Hence the development of an ideal sorbent to be used under different reaction conditions is still a concern. Therefore, to commercialize these promising 2D nanomaterials, researchers should pay immense attention to filling the research gaps and rectifying the technical challenges.

Although enormous efforts have been dedicated in developing a better photocatalyst, the key to ultimate stability and durability, a cure to photodecomposition, *etc.* are still unknown. The production of low-cost earth-abundant elements and their mechanistic insight as co-photocatalysts for forming an efficient 2D photocatalyst are also among the many challenges, including poor yield, photoexcited charge carrier kinetics, active sites, recyclability, *etc.* The implementation of advanced tailoring strategies for the development of electronic and chemical structures, for instance, homogeneous doping in 2D material semiconductor photocatalysts, has been among the few successful attempts in the long run.[349,350] However, it is still difficult to track the particular dopant-induced electronic states in the system. Moreover, the effects of these dopants on photocatalyst stability during the reaction process remain a puzzle. Therefore, a novel doping policy should be assigned to steer its distribution, homogeneity, and composition which goes along with the surface state traits of photocatalysts so as to realize a functional design. Furthermore, the role of inherent or intrinsic defects, structural design, number of 2D layers, and lateral interface dimensions in the output catalytic performance, particularly in a composite photocatalyst, is yet to be investigated. A comprehensive study regarding the charge transfer process and pathways, charge carrier migration diffusivity, and fast recombination reasons should be conducted while considering practical issues regarding recyclability and device design for the establishment of an advanced ideal photocatalyst.[351]

For commercial CO_2 electrocatalysis applications, researchers still face some challenges. Firstly, it is difficult to produce 2D nanomaterials on a large scale while maintaining well-controlled uniform structures due to their electrostatic interaction, strong in-plane bonds and π–π stacking within the atomic layers, resulting in agglomeration and low yield.

Another problem is the analysis of the 2D structures at the atomic level to optimise the catalytic factors such as catalytic activity, selectivity, and stability which further leads to enhanced CO_2 ECR current density, reduction of CO_2 to C_2 and C_{2+} chemicals, and large cyclability for industrial application. The in-depth understanding of the reaction mechanisms limits the future commercialisation of the ECR process.

The major challenge of PEC conversion of CO_2 is its large scale production. Even though electrocatalytic conversion is commercialized, PEC conversion of CO_2 is still at the laboratory scale and needs to be developed and upgraded for pilot-scale production. One of the most challenging tasks in PEC conversion is its high consumption of energy and its meager product yield. The cost of electricity for biasing the photoelectrodes may sometimes be greater than the cost of products yielded. The research on PEC conversion without external bias should be developed and investigated for practical viability. PEC cells are still ambiguous for their long-term usability. Also, the present photoelectrode materials exhibit high overpotential with low product selectivity. Moreover, theoretical studies should surpass the present gap between kinetic and thermodynamic factors for CO_2 binding and bond-breakage by different photocatalytic materials for their bandgap engineering and tuning of reduction potentials to enhance CO_2 affinity and conversion.

Industrially, the thermocatalytic conversion of CO_2 to value-added products is possible under the influence of medium to high pressure, using liquid and gas phase reactors. The requirements of pure CO_2 gas, high temperature and pressure, and the lack of utility of direct intake of atmospheric CO_2 make thermocatalysis uninteresting compared to other catalytic conversion techniques. In most of the studies, 2D materials have been used as supporting materials for single-atom catalysts. The properties of 2D materials such as high electrical conductivity, high surface area, photogeneration of charge carriers, *etc.* make them attractive in photoreduction, electroreduction and photoelectroreduction of CO_2. However, these properties of 2D materials do not contribute to the thermal reduction of CO_2; therefore, the studies focused on the thermocatalysis of CO_2 by 2D materials are generally rare.

5.2 Techno-economic analysis

Along with developing laboratory-scale techniques for capturing and converting CO_2, performing techno-economic analysis of those methodologies is inevitable in identifying the economically viable technologies. Among the different strategies for CO_2 conversion to valuable products, electrochemical CO_2 reduction is close to commercialisation by companies such as Mitsui Chemical and Carbon Recycling International.[352–354] Economic analysis performed on electrocatalytic CO_2 reduction to produce carbon monoxide and formic acid (100 tons per day) revealed end-of-life net present values (NPV) of \$13.5 million and \$39.4 million,

This journal is © The Royal Society of Chemistry 2021

React. Chem. Eng., 2021, **6**, 1701–1738 | **1729**

respectively.[355] Because of the market potential associated with higher-order alcohols such as ethanol and *n*-propanol, the profitability analysis for producing these liquid fuels is also indispensable. The techno-economic model mentions that reaching a target of 70% faradaic efficiency at 0.5 V overpotential can achieve profitable ethanol and propanol production *via* electrocatalytic CO_2 reduction. In a similar study, researchers analyse the possibility of cost-effective production of ethylene glycol by CO_2 reduction.[354] By performing various cost analyses, the study concluded that ethylene glycol is an economically viable target if the electrocatalytic system can be coupled with a cheap renewable source of electricity.

Integrating the methodologies for CO_2 capture and conversion is projected to be a cost-effective strategy. When the captured CO_2 is directly utilised for a conversion reaction, an extra step of desorption can be eliminated. A recent study showed that an integrated CO_2 capture conversion process could save 8% cost while converting a mixture of CO_2 and methanol to methyl formate.[356] Further studies on economic analysis are required to identify and explore the economically viable CO_2 capture and conversion strategies.

6. Conclusions

2D nanomaterials with a good surface area, porosity, and unique and tuneable topography, or textures can be widely used for CO_2 adsorption and conversion. The analysis of various 2D nanomaterials for CO_2 adsorption reveals that a substantial improvement in CO_2 adsorption was observed using nitrogen-doped or nitrogen functionality incorporating adsorbents. The chemisorption of the adsorbate along with physisorption leads to enhanced CO_2 uptake in the N doped systems. In comparison to other gases such N_2 or H_2, CO_2 molecules with a high EQM value would get adsorbed, leading to the selective adsorption of CO_2. On the other hand, with the help of computational tools, many researchers could accelerate the research on CO_2 adsorption on 2D nanomaterials. Though theoretical studies have proven the importance of defect engineering towards enhanced CO_2 adsorption in 2D materials, more experimental analyses in the area are to be explored for developing highly efficient CO_2 adsorbents. Through the current examination, we can understand that N doped (PPy or PANI) aerogels or porous adsorbents based on 2D materials, especially graphene or MXenes, are promising towards CO_2 adsorption applications.

In the photocatalytic reduction of CO_2, the thermodynamic hindrance of the stable CO_2 molecule was remedied by a semiconducting photocatalyst with light energy driving force under ambient conditions. Several 2D materials based on graphene, g-C_3N_4, metal oxides in thin atomic layers, LDHs, TMDCs, h-BN, *etc.* have been utilised for photocatalytic conversion of CO_2 to value added products. A deeper understanding of the mechanism in 2D materials is still unclear, and this is due to the unawareness of contributions from photoinduced carriers generated under light irradiation. By finding suitable remedies to the issues mentioned above, the future developments of photocatalytic CO_2 reduction *via* 2D materials are expected to be tremendous. With the help of an electrochemically active catalyst and external potential, the stable chemical environment of CO_2 can be disturbed for the ECR of CO_2. The design of electrolytes and potential play a vital role in the process of electro-reduction. The high CO_2 conversion efficiency, selectivity, and high TON and TOF make them more attractive for CO_2 reduction. Recently, a wide variety of 2D nanostructures were designed as efficient electrocatalysts for the CO_2 ECR process. The presence of edge sites or edge dopants and the high surface area of 2D structures enable the generation of abundant reactive sites, promoting selective CO_2 reduction with high faradaic efficiency. Most of the research works are supported by theoretical calculations to understand the mechanism of reduction and product selectivity. The tuning of surface, electronic, and structural properties of 2D materials could lead to a suitable electrocatalyst for producing high hydrocarbon value-added fuels in the near future.

The studies on the PEC of CO_2 are in their beginning stage, and significant number of 2D nanomaterials need to be explored for PEC CO_2 conversion. A deeper understanding of the PEC conversion process mechanism is to be accomplished or research in this field should be pursued. The thermocatalytic conversion of CO_2 requires thermal energy and suitable catalysts to disrupt the stable molecular state of carbon dioxide to form products. Facile implementation for scaled-up production, versatility in the products, easy recovery of the catalyst, and high CO_2 conversion rate are the significant advantages. However, in the thermal reduction of CO_2, 2D nanomaterials are widely used as catalyst supports, especially for single-atom catalysts.

Conflicts of interest

There are no conflicts to declare.

Acknowledgements

Notes and references

1 X. Wang, T. He, J. Hu and M. Liu, *Environ. Sci.: Nano*, 2021, **8**, 890–912.

2 A. I. Osman, M. Hefny, M. I. A. Abdel Maksoud, A. M. Elgarahy and D. W. Rooney, *Environ. Chem. Lett.*, 2020, 797–849.

3 A. A. Abd, S. Z. Naji, A. S. Hashim and M. R. Othman, *J. Environ. Chem. Eng.*, 2020, **8**, 104142.

4 M. Bui, C. S. Adjiman, A. Bardow, E. J. Anthony, A. Boston, S. Brown, P. S. Fennell, S. Fuss, A. Galindo, L. A. Hackett, J. P. Hallett, H. J. Herzog, G. Jackson, J. Kemper, S. Krevor,

1730 | *React. Chem. Eng.*, 2021, **6**, 1701–1738

This journal is © The Royal Society of Chemistry 2021

G. C. Maitland, M. Matuszewski, I. S. Metcalfe, C. Petit, G. Puxty, J. Reimer, D. M. Reiner, E. S. Rubin, S. A. Scott, N. Shah, B. Smit, J. P. M. Trusler, P. Webley, J. Wilcox and N. Mac Dowell, *Energy Environ. Sci.*, 2018, **11**, 1062–1176.

5 R. M. Cuellar-Franca and A. Azapagic, *J. CO2 Util.*, 2015, **9**, 82–102.

6 S. Samanta and R. Srivastava, *Mater. Adv.*, 2020, **1**, 1506–1545.

7 Y. Zhao, G. I. N. Waterhouse, G. Chen, X. Xiong, L.-Z. Wu, C.-H. Tung and T. Zhang, *Chem. Soc. Rev.*, 2019, **48**, 1972–2010.

8 N. Huang, X. Chen, R. Krishna and D. Jiang, *Angew. Chem., Int. Ed.*, 2015, **54**, 2986–2990.

9 A. Hasani, M. Tekalgne, Q. V. Le, H. W. Jang and S. Y. Kim, *J. Mater. Chem. A*, 2019, **7**, 430–454.

10 H. Cui, Y. Guo, W. Ma and Z. Zhou, *ChemSusChem*, 2020, **13**, 1155–1171.

11 Z. Sun, T. Ma, H. Tao, Q. Fan and B. Han, *Chem*, 2017, **3**, 560–587.

12 Y.-S. Bae and R. Q. Snurr, *Angew. Chem., Int. Ed.*, 2011, **50**, 11586–11596.

13 F. A. Rahman, M. M. A. Aziz, R. Saidur, W. A. W. A. Bakar, M. R. Hainin, R. Putrajaya and N. A. Hassan, *Renewable Sustainable Energy Rev.*, 2017, **71**, 112–126.

14 P. Wienchol, A. Szlęk and M. Ditaranto, *Energy*, 2020, **198**, 117352.

15 A. H. Alami, A. Abu Hawili, M. Tawalbeh, R. Hasan, L. Al Mahmoud, S. Chibib, A. Mahmood, K. Aokal and P. Rattanapanya, *Sci. Total Environ.*, 2020, **717**, 137221.

16 A. Sharma, J. Jindal, A. Mittal, K. Kumari, S. Maken and N. Kumar, *Environ. Chem. Lett.*, 2021, **19**, 875–910.

17 Y. Zhou, Z. Wang, L. Huang, S. Zaman, K. Lei, T. Yue, Z. A. Li, B. You and B. Y. Xia, *Adv. Energy Mater.*, 2021, **11**, 2003159.

18 C.-M. Fung, J.-Y. Tang, L.-L. Tan, A. R. Mohamed and S.-P. Chai, *Mater. Today Sustain.*, 2020, **9**, 100037.

19 Y. Chen, G. Jia, Y. Hu, G. Fan, Y. H. Tsang, Z. Li and Z. Zou, *Sustainable Energy Fuels*, 2017, **1**, 1875–1898.

20 W.-J. Ong, L. K. Putri and A. R. Mohamed, *Chem. – Eur. J.*, 2020, **26**, 9710–9748.

21 M. A. Tekalgne, H. H. Do, A. Hasani, Q. Van Le, H. W. Jang, S. H. Ahn and S. Y. Kim, *Mater. Today Adv.*, 2020, **5**, 100038.

22 J. Gandara-Loe, L. Pastor-Perez, L. F. Bobadilla, J. A. Odriozola and T. R. Reina, *React. Chem. Eng.*, 2021, **6**, 787–814.

23 S. B. Torrisi, A. K. Singh, J. H. Montoya, T. Biswas and K. A. Persson, *npj 2D Mater. Appl.*, 2019, **4**, 24.

24 H. Cui, Y. Guo, L. Guo, L. Wang, Z. Zhou and Z. Peng, *J. Mater. Chem. A*, 2018, **6**, 18782–18793.

25 V. Kumaravel, J. Bartlett and S. C. Pillai, *ACS Energy Lett.*, 2020, **5**, 486–519.

26 A. Mishra and R. Sundara, *AIP Adv.*, 2011, **1**, 032152.

27 J. Xiao, Y. Wang, T. C. Zhang and S. Yuan, *J. Alloys Compd.*, 2021, **857**, 157534.

28 A. K. Mishra and S. Ramaprabhu, *J. Appl. Phys.*, 2014, **116**, 064306.

29 S. RodrÃguez-GarcÃa, R. Santiago, D. LÃpez-DÃaz, M. D. MerchÃn, M. M. VelÃizquez, J. L. G. Fierro and J. Palomar, *ACS Sustainable Chem. Eng.*, 2019, **7**, 12464–12473.

30 B. Szczęśniak, Ł. Osuchowski, J. Choma and M. Jaroniec, *J. Porous Mater.*, 2018, **25**, 621–627.

31 S. Marchesini, C. M. McGilvery, J. Bailey and C. Petit, *ACS Nano*, 2017, **11**, 10003–10011.

32 S. Chen, P. Li, S. Xu, X. Pan, Q. Fu and X. Bao, *J. Mater. Chem. A*, 2017, **6**, 1832–1839.

33 A. Morales-García, A. A. Ferńandez-Ferńandez, F. Viñes and F. Illas, *J. Mater. Chem. A*, 2018, **6**, 3381–3385.

34 B. Wang, A. Zhou, F. Liu, J. Cao, L. Wang and Q. Hu, *J. Adv. Ceram.*, 2018, **7**, 237–245.

35 S. Ghosh and S. Ramaprabhu, *J. CO2 Util.*, 2017, **21**, 89–99.

36 M. Atilhan, S. Atilhan, R. Ullah, B. Anaya, T. Cagin, C. T. Yavuz and S. Aparicio, *J. Chem. Eng. Data*, 2016, **61**, 2749–2760.

37 Q. Al-Naddaf, A. A. Rownaghi and F. Rezaei, *Chem. Eng. J.*, 2020, **384**, 123251.

38 M. Xu, S. Chen, D.-K. Seo and S. Deng, *Chem. Eng. J.*, 2019, **371**, 693–705.

39 R. Kodasma, J. Fermoso and A. Sanna, *Chem. Eng. J.*, 2019, **358**, 1351–1362.

40 M. R. Hudson, W. L. Queen, J. A. Mason, D. W. Fickel, R. F. Lobo and C. M. Brown, *J. Am. Chem. Soc.*, 2012, **134**, 1970–1973.

41 C. Xu, C.-Q. Ruan, Y. Li, J. Lindh and M. Strømme, *Adv. Sustainable Syst.*, 2018, **2**, 1700147.

42 L. Yue, Q. Xia, L. Wang, L. Wang, H. DaCosta, J. Yang and X. Hu, *J. Colloid Interface Sci.*, 2018, **511**, 259–267.

43 L. Wang, F. Sun, F. Hao, Z. Qu, J. Gao, M. Liu, K. Wang, G. Zhao and Y. Qin, *Chem. Eng. J.*, 2020, **383**, 123205.

44 B. González and J. J. Manyà, *Chem. Eng. Process.*, 2020, **149**, 107830.

45 A. S. González, M. G. Plaza, F. Rubiera and C. Pevida, *Chem. Eng. J.*, 2013, **230**, 456–465.

46 Q. Xu, L. Fang, Y. Fu, Q. Xiao, F. Zhang and W. Zhu, *Mater. Lett.*, 2020, **264**, 127402.

47 X.-t. Lu, Y.-f. Pu, L. Li, N. Zhao, F. Wang and F.-k. Xiao, *J. Fuel Chem. Technol.*, 2019, **47**, 338–343.

48 H. R. Abid, Z. H. Rada, Y. Li, H. A. Mohammed, Y. Wang, S. Wang, H. Arandiyan, X. Tan and S. Liu, *RSC Adv.*, 2020, **10**, 8130–8139.

49 I. Bratsos, C. Tampaxis, I. Spanopoulos, N. Demitri, G. Charalambopoulou, D. Vourloumis, T. A. Steriotis and P. N. Trikalitis, *Inorg. Chem.*, 2018, **57**, 7244–7251.

50 L. Asgharnejad, A. Abbasi and A. Shakeri, *Microporous Mesoporous Mater.*, 2018, **262**, 227–234.

51 J. de O. N. Ribeiro, E. H. M. Nunes, D. C. L. Vasconcelos, W. L. Vasconcelos, J. F. Nascimento, W. M. Grava and P. W. J. Derks, *J. Porous Mater.*, 2019, **26**, 1581–1591.

52 J. Fernandes, A. C. Fernandes, J. C. Echeverría, P. Moriones, J. J. Garrido and J. Pires, *Colloids Surf., A*, 2019, **561**, 128–135.

53 M. Yao, M. Dong, X. Feng, X. Hu, A. Jia, G. Xie, G. Hu, J. Lu, M. Luo and M. Fan, *Fuel*, 2014, **123**, 66–72.

This journal is © The Royal Society of Chemistry 2021

React. Chem. Eng., 2021, **6**, 1701–1738 | **1731**

54 D. Jansen, M. Gazzani, G. Manzolini, E. v. Dijk and M. Carbo, *Int. J. Greenhouse Gas Control*, 2015, **40**, 167–187.

55 A. I. Osman, J. K. Abu-Dahrieh, N. Cherkasov, J. Fernandez-Garcia, D. Walker, R. I. Walton, D. W. Rooney and E. Rebrov, *Mol. Catal.*, 2018, **455**, 38–47.

56 A. Pettinau, F. Ferrara, V. Tola and G. Cau, *Appl. Energy*, 2017, **193**, 426–439.

57 S. Krishnamurthy, A. Lind, A. Bouzga, J. Pierchala and R. Blom, *Chem. Eng. J.*, 2021, **406**, 127121.

58 W. Choi, J. Park, C. Kim and M. Choi, *Chem. Eng. J.*, 2020, **408**, 127289.

59 C. Shi, L. Li and Y. Li, *J. CO2 Util.*, 2020, **42**, 101346.

60 A. Rehman, Y.-J. Heo, G. Nazir and S.-J. Park, *Carbon*, 2021, **172**, 71–82.

61 A. Pal, K. A. Rocky and B. B. Saha, *J. CO2 Util.*, 2021, **46**, 101457.

62 X. Liu, K. O. Kirlikovali, Z. Chen, K. Ma, K. B. Idrees, R. Cao, X. Zhang, T. Islamoglu, Y. Liu and O. K. Farha, *Chem. Mater.*, 2021, **33**, 1444–1454.

63 R. Belgamwar, A. Maity, T. Das, S. Chakraborty, C. P. Vinod and V. Polshettiwar, *Chem. Sci.*, 2021, **12**, 4825–4835.

64 Y. Yang, S. Yao, Y. Hu, J. Sun, Q. Li, Z. Li, S. Zhou and W. Liu, *Chem. Eng. J.*, 2021, **410**, 128346.

65 L. Keller, B. Ohs, J. Lenhart, L. Abduly, P. Blanke and M. Wessling, *Carbon*, 2018, **126**, 338–345.

66 Q. Liu, Y. Shi, S. Zheng, L. Ning, Q. Ye, M. Tao and Y. He, *J. Energy Chem.*, 2014, **23**, 111–118.

67 N. Politakos, I. Barbarin, L. S. Cantador, J. A. Cecilia, E. Mehravar and R. Tomovska, *Ind. Eng. Chem. Res.*, 2020, **59**, 8612–8621.

68 G. M. Meconi and R. Zangi, *Phys. Chem. Chem. Phys.*, 2020, **22**, 21031–21041.

69 A. Pruna, A. C. CÃircel, A. Benedito and E. Gimenez, *Appl. Surf. Sci.*, 2019, **487**, 228–235.

70 A. Ali, R. Pothu, S. H. Siyal, S. Phulpoto, M. Sajjad and K. H. Thebo, *Mater. Sci. Energy Technol.*, 2019, **2**, 83–88.

71 K. Takeuchi, S. Yamamoto, Y. Hamamoto, Y. Shiozawa, K. Tashima, H. Fukidome, T. Koitaya, K. Mukai, S. Yoshimoto, M. Suemitsu, Y. Morikawa, J. Yoshinobu and I. Matsuda, *J. Phys. Chem. C*, 2017, **121**, 2807–2814.

72 K. Xia, X. Tian, S. Fei and K. You, *Int. J. Hydrogen Energy*, 2014, **39**, 11047–11054.

73 F. M. Enujekwu, Y. Zhang, C. I. Ezeh, H. Zhao, M. Xu, E. Besley, M. W. George, N. A. Besley, H. Do and T. Wu, *Appl. Surf. Sci.*, 2021, **542**, 148556.

74 Y. Xie, X. Li, Y. Wang, B. Li, L. Yang, N. Zhao, M. Liu, X. Wang, Y. Yu and J. M. Liu, *Appl. Surf. Sci.*, 2020, **499**, 143964.

75 X. Mu, S. Liu, Y. Chen, U. K. Cheang, M. W. George and T. Wu, *Ind. Eng. Chem. Res.*, 2020, **59**, 5808–5817.

76 N. Aguilar and S. Aparicio, *J. Phys. Chem. C*, 2019, **123**, 26338–26350.

77 S. Rozas, R. Alcalde, M. Atilhan and S. Aparicio, *Appl. Surf. Sci.*, 2019, **480**, 83–95.

78 P. S. Owuor, O.-K. Park, C. F. Woellner, A. S. Jalilov, S. Susarla, J. Joyner, S. Ozden, L. Duy, R. Villegas Salvatierra, R. Vajtai, J. M. Tour, J. Lou, D. S. Galvão, C. S. Tiwary and P. M. Ajayan, *ACS Nano*, 2017, **11**, 8944–8952.

79 X. Lu, M. Zhang, D. Jin, Y. Dang, S. Zhou, S. Wei, H. Zhu and L. Zhao, *Mater. Lett.*, 2015, **161**, 545–548.

80 H. Guo, W. Zhang, N. Lu, Z. Zhuo, X. C. Zeng, X. Wu and J. Yang, *J. Phys. Chem. C*, 2015, **119**, 6912–6917.

81 Q. Sun, Z. Li, D. J. Searles, Y. Chen, G. Lu and A. Du, *J. Am. Chem. Soc.*, 2013, **135**, 8246–8253.

82 A. n. Morales-GarcÍa, M. Mayans-Llorach, F. Viñes and F. Illas, *Phys. Chem. Chem. Phys.*, 2019, **21**, 23136–23142.

83 S. Yang, Z. Wang, X. Dai, J. Xiao, M. Long and T. Chen, *Coatings*, 2019, **9**, 763.

84 Y. Zhang, C. Liu, F. Hao, H. Xiao, S. Zhang and X. Chen, *Appl. Surf. Sci.*, 2017, **397**, 206–212.

85 H.-L. Peng, F.-Y. Zhong, J.-B. Zhang, J.-Y. Zhang, P.-K. Wu, K. Huang, J.-P. Fan and L.-L. Jiang, *Ind. Eng. Chem. Res.*, 2018, **57**, 11031–11038.

86 X. Tang, A. Du and L. Kou, *Wiley Interdiscip. Rev.: Comput. Mol. Sci.*, 2018, **8**, e1361.

87 D. E. Sheehy and J. Schmalian, *Phys. Rev. B: Condens. Matter Mater. Phys.*, 2009, **80**, 193411.

88 K. S. Novoselov, A. K. Geim, S. V. Morozov, D. Jiang, Y. Zhang, S. V. Dubonos, I. V. Grigorieva and A. A. Firsov, *Science*, 2004, **306**, 666–669.

89 R. S. Shishir and D. K. Ferry, *J. Phys.: Condens. Matter*, 2009, **21**, 232204.

90 S. Debroy, S. Sivasubramani, G. Vaidya, S. G. Acharyya and A. Acharyya, *Sci. Rep.*, 2020, **10**, 6240.

91 C. Lee, X. Wei, J. W. Kysar and J. Hone, *Science*, 2008, **321**, 385–388.

92 S. Ghosh, I. Calizo, D. Teweldebrhan, E. P. Pokatilov, D. L. Nika, A. A. Balandin, W. Bao, F. Miao and C. N. Lau, *Appl. Phys. Lett.*, 2008, **92**, 151911.

93 R. Balasubramanian and S. Chowdhury, *J. Mater. Chem. A*, 2015, **3**, 21968–21989.

94 A. Ganesan and M. M. Shaijumon, *Microporous Mesoporous Mater.*, 2016, **220**, 21–27.

95 S. Acevedo, L. Giraldo and J. C. Moreno-Piraján, *ACS Omega*, 2020, **5**, 10423–10432.

96 M. Saleh, V. Chandra, K. Christian Kemp and K. S. Kim, *Nanotechnology*, 2013, **24**, 255702.

97 B. Szczęśniak, J. Choma and M. Jaroniec, *Adv. Colloid Interface Sci.*, 2017, **243**, 46–59.

98 W. Yuan, J. Chen and G. Shi, *Mater. Today*, 2014, **17**, 77–85.

99 A. Ghosh, K. S. Subrahmanyam, K. S. Krishna, S. Datta, A. Govindaraj, S. K. Pati and C. N. R. Rao, *J. Phys. Chem. C*, 2008, **112**, 15704–15707.

100 J. Li, W. Zhang and A. Bao, *Ind. Eng. Chem. Res.*, 2021, **60**, 2710–2718.

101 X. Ma, C. Su, B. Liu, Q. Wu, K. Zhou, Z. Zeng and L. Li, *Sep. Purif. Technol.*, 2021, **259**, 118065.

102 J. Li, C. Shi and A. Bao, *J. Environ. Chem. Eng.*, 2021, **9**, 105250.

103 J. Oh, Y.-H. Mo, V.-D. Le, S. Lee, J. Han, G. Park, Y.-H. Kim, S.-E. Park and S. Park, *Carbon*, 2014, **79**, 450–456.

104 J. Li, M. Hou, Y. Chen, W. Cen, Y. Chu and S. Yin, *Appl. Surf. Sci.*, 2017, **399**, 420–425.

105 S. Shrivastava, S. Thomas, C. B. Sobhan and G. P. Peterson, *Int. J. Refrig.*, 2018, **96**, 179–190.

106 T.-C. Huang, Y.-C. Liu, G.-S. Lin, C.-H. Lin, W.-R. Liu and K.-L. Tung, *J. Membr. Sci.*, 2020, **602**, 117946.

107 H. Chen, Y. Guo, Y. Du, X. Xu, C. Su, Z. Zeng and L. Li, *Chem. Eng. J.*, 2021, **415**, 128824.

108 D. Xia, H. Li, J. Mannering, P. Huang, X. Zheng, A. Kulak, D. Baker, D. Iruretagoyena and R. Menzel, *Adv. Funct. Mater.*, 2020, **30**, 2002788.

109 H. Ning, Z. Yang, D. Wang, Z. Meng, Y. Li, X. Ju and C. Wang, *Microporous Mesoporous Mater.*, 2021, **311**, 110700.

110 Z.-Y. Sui, Y. Cui, J.-H. Zhu and B.-H. Han, *ACS Appl. Mater. Interfaces*, 2013, **5**, 9172–9179.

111 Y. Liu, M. Xiang and L. Hong, *RSC Adv.*, 2017, **7**, 6467–6473.

112 A. K. Mishra and S. Ramaprabhu, *J. Mater. Chem.*, 2012, **22**, 3708–3712.

113 V. Chandra, S. U. Yu, S. H. Kim, Y. S. Yoon, D. Y. Kim, A. H. Kwon, M. Meyyappan and K. S. Kim, *Chem. Commun.*, 2012, **48**, 735–737.

114 S. Manzeli, D. Ovchinnikov, D. Pasquier, O. V. Yazyev and A. Kis, *Nat. Rev. Mater.*, 2017, **2**, 17033.

115 H. Nan, R. Zhou, X. Gu, S. Xiao and K. Ostrikov, *Nanoscale*, 2019, **11**, 19202–19213.

116 S.-J. An, Y. H. Kim, C. Lee, D. Y. Park and M. S. Jeong, *Sci. Rep.*, 2018, **8**, 12957.

117 E. D. Grayfer, M. N. Kozlova and V. E. Fedorov, *Adv. Colloid Interface Sci.*, 2017, **245**, 40–61.

118 G. W. Shim, W. Hong, S. Y. Yang and S.-Y. Choi, *J. Mater. Chem. A*, 2017, **5**, 14950–14968.

119 Y. Shen, H. Wang, X. Zhang and Y. Zhang, *ACS Appl. Mater. Interfaces*, 2016, **8**, 23371–23378.

120 Y.-C. Liu, C.-Y. Chen, G.-S. Lin, C.-H. Chen, K. C. W. Wu, C.-H. Lin and K.-L. Tung, *J. Membr. Sci.*, 2019, **582**, 358–366.

121 Q. Sun, G. Qin, Y. Ma, W. Wang, P. Li, A. Du and Z. Li, *Nanoscale*, 2017, **9**, 19–24.

122 G. Shi, L. Yu, X. Ba, X. Zhang, J. Zhou and Y. Yu, *Dalton Trans.*, 2017, **46**, 10569–10577.

123 S.-Y. Cho, S. J. Kim, Y. Lee, J.-S. Kim, W.-B. Jung, H.-W. Yoo, J. Kim and H.-T. Jung, *ACS Nano*, 2015, **9**, 9314–9321.

124 W. Ai, L. Kou, X. Hu, Y. Wang, A. V. Krasheninnikov, L. Sun and X. Shen, *J. Phys.: Condens. Matter*, 2019, **31**, 445301.

125 A. Nag, K. Raidongia, K. P. S. S. Hembram, R. Datta, U. V. Waghmare and C. N. R. Rao, *ACS Nano*, 2010, **4**, 1539–1544.

126 F. Xiao, Z. Chen, G. Casillas, C. Richardson, H. Li and Z. Huang, *Chem. Commun.*, 2016, **52**, 3911–3914.

127 M. Naguib, V. N. Mochalin, M. W. Barsoum and Y. Gogotsi, *Adv. Mater.*, 2013, **26**, 992–1005.

128 T. Li, T. Yao, Q. Liu, J. Gu, R. Luo, J. Li, X. Yan, W. Wang, P. Liu, B. Chen, W. Zhang, W. Abbas, R. Naz and D. Zhang, *Angew. Chem., Int. Ed.*, 2018, **57**, 6115–6119.

129 W. Sun, S. A. Shah, Y. Chen, Z. Tan, H. Gao, T. Habib, M. Radovic and M. J. Green, *J. Mater. Chem. A*, 2017, **5**, 21663–21668.

130 Y. Li, H. Shao, Z. Lin, J. Lu, L. Liu, B. Duployer, P. O. Å. Persson, P. Eklund, L. Hultman, M. Li, K. Chen, X.-H. Zha, S. Du, P. Rozier, Z. Chai, E. Raymundo-Piñero, P.-L. Taberna, P. Simon and Q. Huang, *Nat. Mater.*, 2020, **19**, 894–899.

131 Z. Guo, Y. Li, B. Sa, Y. Fang, J. Lin, Y. Huang, C. Tang, J. Zhou, N. Miao and Z. Sun, *Appl. Surf. Sci.*, 2020, **521**, 146436.

132 R. Morales-Salvador, Á. Morales-García, F. Viñes and F. Illas, *Phys. Chem. Chem. Phys.*, 2018, **20**, 17117–17124.

133 I. Persson, J. Halim, H. Lind, T. W. Hansen, J. B. Wagner, L.-Å. Näslund, V. Darakchieva, J. Palisaitis, J. Rosen and P. O. Å. Persson, *Adv. Mater.*, 2019, **31**, 1805472.

134 F. Shi, J. Sun, J. Wang, M. Liu, Z. Yan, B. Zhu, Y. Li and X. Cao, *J. Membr. Sci.*, 2021, **620**, 118850.

135 Y. Oh, V.-D. Le, U. N. Maiti, J. O. Hwang, W. J. Park, J. Lim, K. E. Lee, Y.-S. Bae, Y.-H. Kim and S. O. Kim, *ACS Nano*, 2015, **9**, 9148–9157.

136 K. Homlamai, T. Maihom, S. Choomwattana, M. Sawangphruk and J. Limtrakul, *Appl. Surf. Sci.*, 2020, **499**, 143928.

137 Y. Cheng, X. Wang, C. Jia, Y. Wang, L. Zhai, Q. Wang and D. Zhao, *J. Membr. Sci.*, 2017, **539**, 213–223.

138 Y. B. Apriliyanto, N. Darmawan, N. Faginas-Lago and A. Lombardi, *Phys. Chem. Chem. Phys.*, 2020, **22**, 25918–25929.

139 S. Das, T. Ben, S. Qiu and V. Valtchev, *ACS Appl. Mater. Interfaces*, 2020, **12**, 52899–52907.

140 Z. Kang, Y. Peng, Y. Qian, D. Yuan, M. A. Addicoat, T. Heine, Z. Hu, L. Tee, Z. Guo and D. Zhao, *Chem. Mater.*, 2016, **28**, 1277–1285.

141 Y. Ying, M. Tong, S. Ning, S. K. Ravi, S. B. Peh, S. C. Tan, S. J. Pennycook and D. Zhao, *J. Am. Chem. Soc.*, 2020, **142**, 4472–4480.

142 Z.-Q. Wang, T.-Y. Lü, H.-Q. Wang, Y. P. Feng and J.-C. Zheng, *Front. Phys.*, 2019, **14**, 33403.

143 X. Tan, H. A. Tahini and S. C. Smith, *ACS Appl. Mater. Interfaces*, 2017, **9**, 19825–19830.

144 S. Kumar, M. Singh, D. K. Sharma and S. Auluck, *Comput. Condens. Matter*, 2020, **22**, e00436.

145 T. Liu, Y. Chen, M. Zhang, L. Yuan, C. Zhang, J. Wang and J. Fan, *AIP Adv.*, 2017, **7**, 125007.

146 T. Kaewmaraya, L. Ngamwongwan, P. Moontragoon, W. Jarernboon, D. Singh, R. Ahuja, A. Karton and T. Hussain, *J. Hazard. Mater.*, 2021, **401**, 123340.

147 S. Zhou, M. Wang, S. Wei, S. Cao, Z. Wang, S. Liu, D. Sun and X. Lu, *Mater. Today Phys.*, 2021, **16**, 100301.

148 M. Khajeh and A. Ghaemi, *J. Chin. Chem. Soc.*, 2020, **67**, 253–266.

149 M. Khajeh and A. Ghaemi, *J. Environ. Chem. Eng.*, 2020, **8**, 103663.

150 S. Stanly, E. J. Jelmy, C. P. R. Nair and H. John, *J. Environ. Chem. Eng.*, 2019, **7**, 103344.

151 P. Bollini, S. A. Didas and C. W. Jones, *J. Mater. Chem.*, 2011, **21**, 15100–15120.

152 D. Dutta, B. C. Wood, S. Y. Bhide, K. G. Ayappa and S. Narasimhan, *J. Phys. Chem. C*, 2014, **118**, 7741–7750.

153 P. Cabrera-Sanfelix, *J. Phys. Chem. A*, 2009, **113**, 493–498.

154 Z. Fang, B. Bueken, D. E. De Vos and R. A. Fischer, *Angew. Chem., Int. Ed.*, 2015, **54**, 7234–7254.

This journal is © The Royal Society of Chemistry 2021

React. Chem. Eng., 2021, **6**, 1701–1738 | **1733**

155 M. Ghashghaee and M. Ghambarian, *Int. J. Quantum Chem.*, 2020, **120**, e26265.

156 Z. Cui, C. Xiao, Y. Lv, Q. Li, R. Sa and Z. Ma, *Appl. Surf. Sci.*, 2020, **527**, 146894.

157 Y. Zhao, G. I. N. Waterhouse, G. Chen, X. Xiong, L. Z. Wu, C. H. Tung and T. Zhang, *Chem. Soc. Rev.*, 2019, **48**, 1972–2010.

158 M. A. Tekalgne, H. H. Do, A. Hasani, Q. Van Le, H. W. Jang, S. H. Ahn and S. Y. Kim, *Mater. Today Adv.*, 2020, **5**, 100038.

159 M. Mikkelsen, M. Jørgensen and F. C. Krebs, *Energy Environ. Sci.*, 2010, **3**, 43–81.

160 B. A. Rosen, A. Salehi-khojin, M. R. Thorson, W. Zhu, D. T. Whipple, P. J. A. Kenis and R. I. Masel, *Science*, 2011, 643–644.

161 J. Schneider, H. Jia, J. T. Muckerman and E. Fujita, *Chem. Soc. Rev.*, 2012, **41**, 2036–2051.

162 T. Inoue, A. F. Shima, K. Sa Toshi and K. Honda, *Nature*, 1979, **277**, 637–637.

163 C. Costentin, M. Robert and J. M. Savéant, *Chem. Soc. Rev.*, 2013, **42**, 2423–2436.

164 M. H. V. Huynh and T. J. Meyer, *Chem. Rev.*, 2007, 5004–5064.

165 W. H. Wang, Y. Himeda, J. T. Muckerman, G. F. Manbeck and E. Fujita, *Chem. Rev.*, 2015, **115**, 12936–12973.

166 Q. Liu, D. Wu, Y. Zhou, H. Su, R. Wang, C. Zhang, S. Yan, M. Xiao and Z. Zou, *ACS Appl. Mater. Interfaces*, 2014, **6**, 2356–2361.

167 W. Tu, Y. Zhou and Z. Zou, *Adv. Mater.*, 2014, **26**, 4607–4626.

168 S. N. Habisreutinger, L. Schmidt-Mende and J. K. Stolarczyk, *Angew. Chem., Int. Ed.*, 2013, **52**, 7372–7408.

169 J. L. White, M. F. Baruch, J. E. Pander, Y. Hu, I. C. Fortmeyer, J. E. Park, T. Zhang, K. Liao, J. Gu, Y. Yan, T. W. Shaw, E. Abelev and A. B. Bocarsly, *Chem. Rev.*, 2015, **115**, 12888–12935.

170 J. M. Barlow and J. Y. Yang, *ACS Cent. Sci.*, 2019, **5**, 580–588.

171 G. Gao, Y. Jiao, E. R. Waclawik and A. Du, *J. Am. Chem. Soc.*, 2016, **138**, 6292–6297.

172 S. Chen, H. Wang, Z. Kang, S. Jin, X. Zhang, X. Zheng, Z. Qi, J. Zhu, B. Pan and Y. Xie, *Nat. Commun.*, 2019, **10**, 788–788.

173 X. Jiao, X. Li, X. Jin, Y. Sun, J. Xu, L. Liang, H. Ju, J. Zhu, Y. Pan, W. Yan, Y. Lin and Y. Xie, *J. Am. Chem. Soc.*, 2017, **139**, 18044–18051.

174 B. Han, X. Ou, Z. Deng, Y. Song, C. Tian, H. Deng, Y.-j. Xu and Z. Lin, *Angew. Chem., Int. Ed.*, 2018, 16811–16815.

175 G. Gao, Y. Jiao, E. R. Waclawik and A. Du, *J. Am. Chem. Soc.*, 2016, **138**, 6292–6297.

176 M. Ye, X. Wang, E. Liu, J. Ye and D. Wang, *ChemSusChem*, 2018, **11**, 1606–1611.

177 J. Ren, S. Ouyang, H. Xu, X. Meng, T. Wang, D. Wang and J. Ye, *Adv. Energy Mater.*, 2017, **7**, 1601657.

178 N. S. Lewis and D. G. Nocera, *Proc. Natl. Acad. Sci. U. S. A.*, 2006, **103**, 15729–15735.

179 Y.-J. Yuan, H.-W. Lu, Z.-T. Yu and Z.-G. Zou, *ChemSusChem*, 2015, **8**, 4113–4127.

180 J.-M. Lehn and R. Ziessel, *Proc. Natl. Acad. Sci. U. S. A.*, 1982, **79**, 701.

181 Y. Hori, A. Murata and R. Takahashi, *J. Chem. Soc., Faraday Trans. 1*, 1989, **85**, 2309–2326.

182 J. Low, J. Yu and W. Ho, *J. Phys. Chem. Lett.*, 2015, **6**, 4244–4251.

183 X. Chang, T. Wang and J. Gong, *Energy Environ. Sci.*, 2016, **9**, 2177–2196.

184 V. P. Indrakanti, J. D. Kubicki and H. H. Schobert, *Energy Environ. Sci.*, 2009, **2**, 745–758.

185 W. Taifan, J. F. Boily and J. Baltrusaitis, *Surf. Sci. Rep.*, 2016, **71**, 595–671.

186 J. Low, B. Cheng and J. Yu, *Appl. Surf. Sci.*, 2017, **392**, 658–686.

187 Y. Ma, B. Qiu, J. Zhang and M. Xing, *ChemNanoMat*, 2021, 368–379, DOI: 10.1002/cnma.202100051.

188 N. Shehzad, M. Tahir, K. Johari, T. Murugesan and M. Hussain, *J. CO2 Util.*, 2018, **26**, 98–122.

189 J. Low, S. Cao, J. Yu and S. Wageh, *Chem. Commun.*, 2014, **50**, 10768–10777.

190 S. Ali, A. Razzaq and S.-l. In, *Catal. Today*, 2019, **335**, 39–54.

191 W. Yu, D. Xu and T. Peng, *J. Mater. Chem. A*, 2015, **3**, 19936–19947.

192 J. Chen, X. J. Wu, L. Yin, B. Li, X. Hong, Z. Fan, B. Chen, C. Xue and H. Zhang, *Am. Ethnol.*, 2015, **127**, 1226–1230.

193 X. Zhang, Z. Ai, F. Jia and L. Zhang, *J. Phys. Chem. C*, 2008, **112**, 747–753.

194 A. Razzaq, S. Ali, M. Asif and S.-l. In, *Catalysts*, 2020, **10**, 1185.

195 X. Zhang, Z. Zhang, J. Li, X. Zhao, D. Wu and Z. Zhou, *J. Mater. Chem. A*, 2017, **5**, 12899–12903.

196 Y. Cao, R. Zhang, T. Zhou, S. Jin, J. Huang, L. Ye, Z. Huang, F. Wang and Y. Zhou, *ACS Appl. Mater. Interfaces*, 2020, **12**, 9935–9943.

197 Y. Matsumoto, M. Koinuma, S. Ida, S. Hayami, T. Taniguchi, K. Hatakeyama, H. Tateishi, Y. Watanabe and S. Amano, *J. Phys. Chem. C*, 2011, **115**, 19280.

198 Y. T. Liang, B. K. Vijayan, K. A. Gray and M. C. Hersam, *Nano Lett.*, 2011, **11**, 2865–2870.

199 X. An, K. Li and J. Tang, *ChemSusChem*, 2014, **7**, 1086–1093.

200 S. Sun, M. Watanabe, P. Wang and T. Ishihara, *ACS Appl. Energy Mater.*, 2019, **2**, 2104–2112.

201 J. Mao, T. Peng, X. Zhang, K. Li, L. Ye and L. Zan, *Catal. Sci. Technol.*, 2013, **3**, 1253–1260.

202 R. Liu, Z. Chen, Y. Yao, Y. Li, W. A. Cheema, D. Wang and S. Zhu, *RSC Adv.*, 2020, **10**, 29408–29418.

203 X.-Y. Dao, X.-F. Xie, J.-H. Guo, X.-Y. Zhang, Y.-S. Kang and W.-Y. Sun, *ACS Appl. Energy Mater.*, 2020, **3**, 3946–3954.

204 H. Feng, Q. Guo, Y. Xu, T. Chen, Y. Zhou, Y. Wang, M. Wang and D. Shen, *ChemSusChem*, 2018, **11**, 4256–4261.

205 Y. Li, H. Xu, S. Ouyang and J. Ye, *Phys. Chem. Chem. Phys.*, 2016, **18**, 7563–7572.

206 Z. Hu, X. Xiao, H. Jin, T. Li, M. Chen, Z. Liang, Z. Guo, J. Li, J. Wan, L. Huang, Y. Zhang, G. Feng and J. Zhou, *Nat. Commun.*, 2017, **8**, 15630.

207 L. Lei, Z. Wu, H. Liu, H. Qin, C. Chen, L. Luo, G. Wang, W. Fan and J. Wang, *J. Mater. Chem. A*, 2018, **6**, 9948–9961.

1734 | *React. Chem. Eng.*, 2021, **6**, 1701–1738

This journal is © The Royal Society of Chemistry 2021

208 Y. Zhao, N. Liu, S. Zhou and J. Zhao, *J. Mater. Chem. A*, 2019, **7**, 16294–16303.

209 F. He, B. Zhu, B. Cheng, J. Yu, W. Ho and W. Macyk, *Appl. Catal., A*, 2020, **272**, 119006.

210 Y. Zhao, M. Que, J. Chen and C. Yang, *J. Mater. Chem. C*, 2020, **8**, 16258–16281.

211 J. Liu, C. Guo, A. Vasileff and S. Qiao, *Small Methods*, 2017, **1**, 1600006.

212 X. Hong, K. Chan, C. Tsai and J. K. Nørskov, *ACS Catal.*, 2016, **6**, 4428–4437.

213 F. Xu, B. Zhu, B. Cheng, J. Yu and J. Xu, *Adv. Opt. Mater.*, 2018, **6**, 1800911.

214 M. R. U. D. Biswas, A. Ali, K. Y. Cho and W.-C. Oh, *Ultrason. Sonochem.*, 2018, **42**, 738–746.

215 H. She, H. Zhou, L. Li, Z. Zhao, M. Jiang, J. Huang, L. Wang and Q. Wang, *ACS Sustainable Chem. Eng.*, 2019, **7**, 650–659.

216 G. B. B. Varadwaj and V. O. Nyamori, *Nano Res.*, 2016, **9**, 3598–3621.

217 N. Ahmed, Y. Shibata and T. Taniguchi, *J. Catal.*, 2011, **279**, 123–135.

218 S. Tonda, S. Kumar, M. Bhardwaj, P. Yadav and S. Ogale, *ACS Appl. Mater. Interfaces*, 2018, **10**, 2667–2678.

219 K. Wang, L.-M. Yang, X. Wang, L. Guo, G. Cheng, C. Zhang, S. Jin, B. Tan and A. Cooper, *Angew. Chem., Int. Ed.*, 2017, **56**, 14149–14153.

220 M. Liu, Q. Huang, S. Wang, Z. Li, B. Li, S. Jin and B. Tan, *Angew. Chem., Int. Ed.*, 2018, **57**, 11968–11972.

221 Y. Zheng, Z. Yu, H. Ou, A. M. Asiri, Y. Chen and X. Wang, *Adv. Funct. Mater.*, 2018, **28**, 1705407.

222 J. Li, P. Liu, H. Huang, Y. Li, Y. Tang, D. Mei and C. Zhong, *ACS Sustainable Chem. Eng.*, 2020, **8**, 5175–5183.

223 G. Glockler, *J. Phys. Chem.*, 1958, **62**, 1049–1054.

224 Y.-J. Zhang, V. Sethuraman, R. Michalsky and A. A. Peterson, *ACS Catal.*, 2014, **4**, 3742–3748.

225 S.-T. Gao, S.-Q. Xiang, J.-L. Shi, W. Zhang and L.-B. Zhao, *Phys. Chem. Chem. Phys.*, 2020, **22**, 9607–9615.

226 H.-J. Yang, H. Yang, Y.-H. Hong, P.-Y. Zhang, T. Wang, L.-N. Chen, F.-Y. Zhang, Q.-H. Wu, N. Tian, Z.-Y. Zhou and S.-G. Sun, *ChemSusChem*, 2018, **11**, 881–887.

227 W. Ni, Y. Xue, X. Zang, C. Li, H. Wang, Z. Yang and Y.-M. Yan, *ACS Nano*, 2020, **14**, 2014–2023.

228 J. Medina-Ramos, J. L. DiMeglio and J. Rosenthal, *J. Am. Chem. Soc.*, 2014, **136**, 8361–8367.

229 C. E. Creissen and M. Fontecave, *Adv. Energy Mater.*, 2020, **2002652**, 1–12.

230 J. P. Jones, G. K. S. Prakash and G. A. Olah, *Isr. J. Chem.*, 2014, **54**, 1451–1466.

231 S. Nitopi, E. Bertheussen, S. B. Scott, X. Liu, A. K. Engstfeld, S. Horch, B. Seger, I. E. L. Stephens, K. Chan, C. Hahn, J. K. Nørskov, T. F. Jaramillo and I. Chorkendorff, *Chem. Rev.*, 2019, **119**, 7610–7672.

232 W. Zhang, Y. Hu, L. Ma, G. Zhu, Y. Wang, X. Xue, R. Chen, S. Yang and Z. Jin, *Adv. Sci.*, 2018, **5**, 1700275.

233 Y. A. Lyon, A. A. Roberts and D. R. McMillin, *J. Chem. Educ.*, 2015, **92**, 2130–2133.

234 R. Kortlever, I. Peters, S. Koper and M. T. M. Koper, *ACS Catal.*, 2015, **5**, 3916–3923.

235 X. Cui, Z. Pan, L. Zhang, H. Peng and G. Zheng, *Adv. Energy Mater.*, 2017, **7**, 1–6.

236 L. Han, S. Song, M. Liu, S. Yao, Z. Liang, H. Cheng, Z. Ren, W. Liu, R. Lin, G. Qi, X. Liu, Q. Wu, J. Luo and H. L. Xin, *J. Am. Chem. Soc.*, 2020, **142**, 12563–12567.

237 S. Yao, L. Lin, W. Liao, N. Rui, N. Li, Z. Liu, J. Cen, F. Zhang, X. Li, L. Song, L. Betancourt De Leon, D. Su, S. D. Senanayake, P. Liu, D. Ma, J. G. Chen and J. A. Rodriguez, *ACS Catal.*, 2019, **9**, 9087–9097.

238 J. Wu, R. M. Yadav, M. Liu, P. P. Sharma, C. S. Tiwary, L. Ma, X. Zou, X.-D. Zhou, B. I. Yakobson, J. Lou and P. M. Ajayan, *ACS Nano*, 2015, **9**, 5364–5371.

239 Y. Ji, J. K. Nørskov and K. Chan, *J. Phys. Chem. C*, 2019, **123**, 4256–4261.

240 S. Kang, S. Ju, S. Han and Y. Kang, *J. Phys. Chem. C*, 2020, **124**, 25812–25820.

241 A. D. Handoko, K. H. Khoo, T. L. Tan, H. Jin and Z. W. Seh, *J. Mater. Chem. A*, 2018, **6**, 21885–21890.

242 J. Wu, T. Sharifi, Y. Gao, T. Zhang and P. M. Ajayan, *Adv. Mater.*, 2019, **31**, 1804257.

243 P. Shao, L. Yi, S. Chen, T. Zhou and J. Zhang, *J. Energy Chem.*, 2020, **40**, 156–170.

244 X. Tan, C. Yu, C. Zhao, H. Huang, X. Yao, X. Han, W. Guo, S. Cui, H. Huang and J. Qiu, *ACS Appl. Mater. Interfaces*, 2019, **11**, 9904–9910.

245 W. Zhang, Q. Qin, L. Dai, R. Qin, X. Zhao, X. Chen, D. Ou, J. Chen, T. T. Chuong, B. Wu and N. Zheng, *Angew. Chem., Int. Ed.*, 2018, **57**, 9475–9479.

246 J.-H. Liu, L.-M. Yang and E. Ganz, *J. Mater. Chem. A*, 2019, **7**, 3805–3814.

247 S. Zhang, Q. Fan, R. Xia and T. J. Meyer, *Acc. Chem. Res.*, 2020, **53**, 255–264.

248 F. J. Fernández-Alvarez and L. A. Oro, *ChemCatChem*, 2018, **10**, 4783–4796.

249 L. Zhang, Z.-J. Zhao and J. Gong, *Angew. Chem., Int. Ed.*, 2017, **56**, 11326–11353.

250 C. B. Hiragond, H. Kim, J. Lee, S. Sorcar, C. Erkey and S.-I. In, *Catalysts*, 2020, **10**, 98.

251 G. G. Naumis, S. Barraza-Lopez, M. Oliva-Leyva and H. Terrones, *Rep. Prog. Phys.*, 2017, **80**, 096501.

252 D. L. T. Nguyen, C. W. Lee, J. Na, M.-C. Kim, N. D. K. Tu, S. Y. Lee, Y. J. Sa, D. H. Won, H.-S. Oh, H. Kim, B. K. Min, S. S. Han, U. Lee and Y. J. Hwang, *ACS Catal.*, 2020, **10**, 3222–3231.

253 X. Zhang, W. Wang and Z. Yang, *ACS Sustainable Chem. Eng.*, 2020, **8**, 6134–6141.

254 Y. Li, C. Chen, R. Cao, Z. Pan, H. He and K. Zhou, *Appl. Catal., B*, 2020, **268**, 118747.

255 W. Bi, X. Li, R. You, M. Chen, R. Yuan, W. Huang, X. Wu, W. Chu, C. Wu and Y. Xie, *Adv. Mater.*, 2018, **30**, 1706617.

256 D. Wu, W. Chen, X. Wang, X.-Z. Fu and J.-L. Luo, *J. CO2 Util.*, 2020, **37**, 353–359.

257 Q. Wang, Y. Lei, Y. Wang, Y. Liu, C. Song, J. Zeng, Y. Song, X. Duan, D. Wang and Y. Li, *Energy Environ. Sci.*, 2020, **13**, 1593–1616.

This journal is © The Royal Society of Chemistry 2021

React. Chem. Eng., 2021, **6**, 1701–1738 | **1735**

258 M. Asadi, K. Kim, C. Liu, A. V. Addepalli, P. Abbasi, P. Yasaei, P. Phillips, A. Behranginia, J. M. Cerrato, R. Haasch, P. Zapol, B. Kumar, R. F. Klie, J. Abiade, L. A. Curtiss and A. Salehi-Khojin, *Science*, 2016, **353**, 467.

259 X. Liu, H. Yang, J. He, H. Liu, L. Song, L. Li and J. Luo, *Small*, 2018, **14**, 1704049.

260 P. Abbasi, M. Asadi, C. Liu, S. Sharifi-Asl, B. Sayahpour, A. Behranginia, P. Zapol, R. Shahbazian-Yassar, L. A. Curtiss and A. Salehi-Khojin, *ACS Nano*, 2017, **11**, 453–460.

261 X. Mao, L. Wang, Y. Xu and Y. Li, *J. Phys. Chem. C*, 2020, **124**, 10523–10529.

262 M. Naguib, M. Kurtoglu, V. Presser, J. Lu, J. Niu, M. Heon, L. Hultman, Y. Gogotsi and M. W. Barsoum, *Adv. Mater.*, 2011, **23**, 4248–4253.

263 C. Yang, H. Huang, H. He, L. Yang, Q. Jiang and W. Li, *Coord. Chem. Rev.*, 2021, **435**, 213806.

264 A. D. Handoko, H. Chen, Y. Lum, Q. Zhang, B. Anasori and Z. W. Seh, *iScience*, 2020, **23**, 101181.

265 H. Chen, A. D. Handoko, T. Wang, J. Qu, J. Xiao, X. Liu, D. Legut, Z. Wei Seh and Q. Zhang, *ChemSusChem*, 2020, **13**, 5690–5698.

266 X. Li and Q.-L. Zhu, *EnergyChem*, 2020, **2**, 100033.

267 M. Tang, H. Shen and Q. Sun, *J. Phys. Chem. C*, 2019, **123**, 26460–26466.

268 P. Lamagni, M. Miola, J. Catalano, M. S. Hvid, M. A. H. Mamakhel, M. Christensen, M. R. Madsen, H. S. Jeppesen, X.-M. Hu, K. Daasbjerg, T. Skrydstrup and N. Lock, *Adv. Funct. Mater.*, 2020, **30**, 1910408.

269 S. Dou, J. Song, S. Xi, Y. Du, J. Wang, Z.-F. Huang, Z. J. Xu and X. Wang, *Angew. Chem., Int. Ed.*, 2019, **58**, 4041–4045.

270 X.-D. Zhang, S.-Z. Hou, J.-X. Wu and Z.-Y. Gu, *Chem. – Eur. J.*, 2020, **26**, 1604–1611.

271 H. Zhong, M. Ghorbani-Asl, K. H. Ly, J. Zhang, J. Ge, M. Wang, Z. Liao, D. Makarov, E. Zschech, E. Brunner, I. M. Weidinger, J. Zhang, A. V. Krasheninnikov, S. Kaskel, R. Dong and X. Feng, *Nat. Commun.*, 2020, **11**, 1409.

272 H.-J. Zhu, M. Lu, Y.-R. Wang, S.-J. Yao, M. Zhang, Y.-H. Kan, J. Liu, Y. Chen, S.-L. Li and Y.-Q. Lan, *Nat. Commun.*, 2020, **11**, 497.

273 F. P. García de Arquer, O. S. Bushuyev, P. De Luna, C.-T. Dinh, A. Seifitokaldani, M. I. Saidaminov, C.-S. Tan, L. N. Quan, A. Proppe, M. G. Kibria, S. O. Kelley, D. Sinton and E. H. Sargent, *Adv. Mater.*, 2018, **30**, 1802858.

274 F. Yang, A. O. Elnabawy, R. Schimmenti, P. Song, J. Wang, Z. Peng, S. Yao, R. Deng, S. Song, Y. Lin, M. Mavrikakis and W. Xu, *Nat. Commun.*, 2020, **11**, 1088.

275 J. Huang, X. Guo, J. Yang and L. Wang, *J. CO2 Util.*, 2020, **38**, 32–38.

276 S. Tang, X. Zhou, S. Zhang, X. Li, T. Yang, W. Hu, J. Jiang and Y. Luo, *ACS Appl. Mater. Interfaces*, 2019, **11**, 906–915.

277 X. Sun, Q. Zhu, X. Kang, H. Liu, Q. Qian, J. Ma, Z. Zhang, G. Yang and B. Han, *Green Chem.*, 2017, **19**, 2086–2091.

278 Y. Zhao, X. Tan, W. Yang, C. Jia, X. Chen, W. Ren, S. C. Smith and C. Zhao, *Angew. Chem.*, 2020, **59**, 21493–21498.

279 T. Yuan, Z. Hu, Y. Zhao, J. Fang, J. Lv, Q. Zhang, Z. Zhuang, L. Gu and S. Hu, *Nano Lett.*, 2020, **20**, 2916–2922.

280 K. J. P. Schouten, Y. Kwon, C. J. M. van der Ham, Z. Qin and M. T. M. Koper, *Chem. Sci.*, 2011, **2**, 1902–1909.

281 T. Inoue, A. Fujishima, S. Konishi and K. Honda, *Nature*, 1979, **277**, 637–638.

282 N. Ulagappan and H. Frei, *J. Phys. Chem. A*, 2000, **104**, 7834–7839.

283 M. Anpo, H. Yamashita, Y. Ichihashi and S. Ehara, *J. Electroanal. Chem.*, 1995, **396**, 21–26.

284 S. Xu and E. A. Carter, *Chem. Rev.*, 2019, **119**, 6631–6669.

285 H.-Y. Kang, D.-H. Nam, K. D. Yang, W. Joo, H. Kwak, H.-H. Kim, S.-H. Hong, K. T. Nam and Y.-C. Joo, *ACS Nano*, 2018, **12**, 8187–8196.

286 A. Jangam, S. Das, N. Dewangan, P. Hongmanorom, W. M. Hui and S. Kawi, *Catal. Today*, 2020, **358**, 3–29.

287 P. Ding, T. Jiang, N. Han and Y. Li, *Mater. Today Nano*, 2020, **10**, 100077.

288 X. Chang, T. Wang, P. Yang, G. Zhang and J. Gong, *Adv. Mater.*, 2019, **31**, 1804710.

289 B. Paul, N. Manwar, P. Bhanja, S. Sellaiyan, S. K. Sharma, R. Khatun, S. Jain and R. Bal, *J. CO2 Util.*, 2020, **41**, 101284.

290 B. Han, J. Wang, C. Yan, Y. Dong, Y. Xu, R. Nie and H. Jing, *Electrochim. Acta*, 2018, **285**, 23–29.

291 Y. He, P. Wang, J. Zhu, Y. Yang, M. Chen, D. Cao and X. Yan, *ACS Appl. Mater. Interfaces*, 2019, **11**, 37322–37329.

292 R. K. Yadav, J.-o. Baeg, G. H. Oh, N.-j. Park, K.-j. Kong, J. Kim, D. W. Hwang and S. K. Biswas, *J. Am. Chem. Soc.*, 2012, **134**, 11455–11461.

293 Y. J. Jang, I. Jeong, J. Lee, J. Lee, M. J. Ko and J. S. Lee, *ACS Nano*, 2016, **10**, 6980–6987.

294 A. U. Pawar, C. W. Kim, M. T. Nguyen-Le and Y. S. Kang, *ACS Sustainable Chem. Eng.*, 2019, **7**, 7431–7455.

295 H. Pang, T. Masuda and J. Ye, *Chem. – Asian J.*, 2018, **13**, 127–142.

296 S. Xie, Q. Zhang, G. Liu and Y. Wang, *Chem. Commun.*, 2016, **52**, 35–59.

297 Q. Quan, S.-J. Xie, Y. Wang and Y.-J. Xu, *Acta Phys.-Chim. Sin.*, 2017, **33**, 2404–2423.

298 K. S. Novoselov, A. K. Geim, S. V. Morozov, D. Jiang, M. I. Katsnelson, I. V. Grigorieva, S. V. Dubonos and A. A. Firsov, *Nature*, 2005, **438**, 197–200.

299 A. Hasani, M. A. Teklagne, H. H. Do, S. H. Hong, Q. Van Le, S. H. Ahn and S. Y. Kim, *Carbon Energy*, 2020, **2**, 158–175.

300 S. Sato, in *Encyclopedia of Applied Electrochemistry*, ed. G. Kreysa, K.-i. Ota and R. F. Savinell, Springer New York, New York, NY, 2014, pp. 1535–1538, DOI: 10.1007/978-1-4419-6996-5_491.

301 T. Wu, L. Zou, D. Han, F. Li, Q. Zhang and L. Niu, *Green Chem.*, 2014, **16**, 2142–2146.

302 B. A. Aragaw, *J. Nanostruct. Chem.*, 2020, **10**, 9–18.

303 S. Guo and S. Dong, *Chem. Soc. Rev.*, 2011, **40**, 2644–2672.

304 M. Zhang, X. Xuan, W. Wang, C. Ma and Z. Lin, *Adv. Funct. Mater.*, 2020, **30**, 2005983.

1736 | *React. Chem. Eng.*, 2021, **6**, 1701–1738

This journal is © The Royal Society of Chemistry 2021

305 H. Wang, Y. Liang, L. Liu, J. Hu and W. Cui, *Appl. Surf. Sci.*, 2017, **392**, 51–60.

306 L. Yang, Z. Li, H. Jiang, W. Jiang, R. Su, S. Luo and Y. Luo, *Appl. Catal., B*, 2016, **183**, 75–85.

307 K. Sun, S. Shen, Y. Liang, P. E. Burrows, S. S. Mao and D. Wang, *Chem. Rev.*, 2014, **114**, 8662–8719.

308 C. Li, Q. Cao, F. Wang, Y. Xiao, Y. Li, J.-J. Delaunay and H. Zhu, *Chem. Soc. Rev.*, 2018, **47**, 4981–5037.

309 C. Gong, H. Zhang, W. Wang, L. Colombo, R. M. Wallace and K. Cho, *Appl. Phys. Lett.*, 2013, **103**, 053513.

310 G. Li, D. Zhang, Q. Qiao, Y. Yu, D. Peterson, A. Zafar, R. Kumar, S. Curtarolo, F. Hunte, S. Shannon, Y. Zhu, W. Yang and L. Cao, *J. Am. Chem. Soc.*, 2016, **138**, 16632–16638.

311 M. Asadi, B. Kumar, A. Behranginia, B. A. Rosen, A. Baskin, N. Repnin, D. Pisasale, P. Phillips, W. Zhu, R. Haasch, R. F. Klie, P. Král, J. Abiade and A. Salehi-Khojin, *Nat. Commun.*, 2014, **5**, 4470.

312 H. Wang, Z. Lu, S. Xu, D. Kong, J. J. Cha, G. Zheng, P.-C. Hsu, K. Yan, D. Bradshaw, F. B. Prinz and Y. Cui, *Proc. Natl. Acad. Sci. U. S. A.*, 2013, **110**, 19701–19706.

313 M. Huang, Y. Zhou, Y. Guo, H. Wang, X. Hu, X. Xu and Z. J. J. o. M. S. Ren, *J. Mater. Sci.*, 2018, **53**, 7744–7754.

314 X. Hui, J. Yi, X. She, Q. Liu, L. Song, S. Chen, Y. Yang, Y. Song, R. Vajtai, J. Lou, H. Li, S. Yuan, J. Wu and P. Ajayan, *Appl. Catal., B*, 2017, **220**, 379–385.

315 S. Bawari, N. M. Kaley, S. Pal, T. V. Vineesh, S. Ghosh, J. Mondal and T. N. Narayanan, *Phys. Chem. Chem. Phys.*, 2018, **20**, 15007–15014.

316 B. M. Tackett, E. Gomez and J. G. Chen, *Nat. Catal.*, 2019, **2**, 381–386.

317 T. Aregawi, T. Yoon, P. Seongho and C.-j. Lee, *J. CO2 Util.*, 2021, **44**, 101413–101413.

318 Y. Li, S. H. Chan and Q. Sun, *Nanoscale*, 2015, **7**, 8663–8683.

319 J. Zhang, Z. Li, Z. Zhang, K. Feng and B. Yan, *Appl. Energy*, 2021, **281**, 116076.

320 L. Xu, Y. Xiu, F. Liu, Y. Liang and S. Wang, *Molecules*, 2020, **25**, 3653.

321 D. Zhao, Z. Chen, W. Yang, S. Liu, X. Zhang, Y. Yu, W.-C. Cheong, L. Zheng, F. Ren, G. Ying, X. Cao, D. Wang, Q. Peng, G. Wang and C. Chen, *J. Am. Chem. Soc.*, 2019, **141**, 4086–4093.

322 V. Deerattrakul, P. Dittanet, M. Sawangphruk and P. Kongkachuichay, *J. CO2 Util.*, 2016, **16**, 104–113.

323 N. D. Mohd Ridzuan, M. S. Shaharun, K. M. Lee, I. Ud Din and P. Puspitasari, *Catalysts*, 2020, **10**, 471.

324 H. Ma, K. Ma, J. Ji, S. Tang, C. Liu, W. Jiang, H. Yue and B. Liang, *Chem. Eng. Sci.*, 2019, **194**, 10–21.

325 X. Lan, Y. Li, C. Du, T. She, Q. Li and G. Bai, *Chem. – Eur. J.*, 2019, **25**, 8560–8569.

326 A. Primo, J. He, B. Jurca, B. Cojocaru, C. Bucur, V. I. Parvulescu and H. Garcia, *Appl. Catal., A*, 2019, **245**, 351–359.

327 Z. Lu, Y. Cheng, S. Li, Z. Yang and R. Wu, *Appl. Surf. Sci.*, 2020, **528**, 147047.

328 H. Li, L. Wang, Y. Dai, Z. Pu, Z. Lao, Y. Chen, M. Wang, X. Zheng, J. Zhu, W. Zhang, R. Si, C. Ma and J. Zeng, *Nat. Nanotechnol.*, 2018, **13**, 411–417.

329 G. Bharath, K. Rambabu, P. P. Morajkar, R. Jayaraman, J. Theerthagiri, S. J. Lee, M. Y. Choi and F. Banat, *J. Hazard. Mater.*, 2021, **409**, 124980.

330 M. Fan, J. D. Jimenez, S. N. Shirodkar, J. Wu, S. Chen, L. Song, M. M. Royko, J. Zhang, H. Guo, J. Cui, K. Zuo, W. Wang, C. Zhang, F. Yuan, R. Vajtai, J. Qian, J. Yang, B. I. Yakobson, J. M. Tour, J. Lauterbach, D. Sun and P. M. Ajayan, *ACS Catal.*, 2019, **9**, 10077–10086.

331 G. Bharath, K. Rambabu, A. Hai, I. Othman, N. Ponpandian, F. Banat and P. Loke Show, *Chem. Eng. J.*, 2021, **414**, 128869.

332 N. de Jesus Martins, I. C. H. Gomes, G. T. S. T. da Silva, J. A. Torres, W. Avansi, C. Ribeiro, A. R. Malagutti and H. A. J. L. Mourão, *J. Alloys Compd.*, 2021, **856**, 156798.

333 D. Shen, X. Li, C. Ma, Y. Zhou, L. Sun, S. Yin, P. Huo and H. Wang, *New J. Chem.*, 2020, **44**, 16390–16399.

334 R. Bhosale, S. Jain, C. P. Vinod, S. Kumar and S. Ogale, *ACS Appl. Mater. Interfaces*, 2019, **11**, 6174–6183.

335 A. Han, M. Li, S. Zhang, X. Zhu, J. Han, Q. Ge and H. Wang, *Catalysts*, 2019, **9**, 927.

336 L. Tan, K. Peter, J. Ren, B. Du, X. Hao, Y. Zhao and Y.-F. Song, *Front. Chem. Sci. Eng.*, 2021, **15**, 99–108.

337 Q. Zhao, C. Zhang, R. Hu, Z. Du, J. Gu, Y. Cui, X. Chen, W. Xu, Z. Cheng, S. Li, B. Li, Y. Liu, W. Chen, C. Liu, J. Shang, L. Song and S. Yang, *ACS Nano*, 2021, **15**, 4927–4936.

338 N. H. Attanayake, H. R. Banjade, A. C. Thenuwara, B. Anasori, Q. Yan and D. R. Strongin, *Chem. Commun.*, 2021, **57**, 1675–1678.

339 Q. Wang, X. Wang, Z. Yu, X. Jiang, J. Chen, L. Tao, M. Wang and Y. Shen, *Nano Energy*, 2019, **60**, 827–835.

340 K. L. Chagoya, D. J. Nash, T. Jiang, D. Le, S. Alayoglu, K. B. Idrees, X. Zhang, O. K. Farha, J. K. Harper, T. S. Rahman and R. G. Blair, *ACS Sustainable Chem. Eng.*, 2021, **9**, 2447–2455.

341 S. Hong, C. K. Rhee and Y. Sohn, *Catalysts*, 2019, **9**, 494.

342 X. Li, Y. Sun, J. Xu, Y. Shao, J. Wu, X. Xu, Y. Pan, H. Ju, J. Zhu and Y. Xie, *Nat. Energy*, 2019, **4**, 690–699.

343 H. Li, B. Sun, Y. Xu, P. Qiao, J. Wu, K. Pan, G. Tian, L. Wang and W. Zhou, *J. Colloid Interface Sci.*, 2018, **531**, 664–671.

344 F. You, J. Wan, J. Qi, D. Mao, N. Yang, Q. Zhang, L. Gu and D. Wang, *Angew. Chem., Int. Ed.*, 2020, **59**, 721–724.

345 J. Hou, S. Cao, Y. Wu, F. Liang, Y. Sun, Z. Lin and L. Sun, *Nano Energy*, 2017, **32**, 359–366.

346 S. Gao, B. Gu, X. Jiao, Y. Sun, X. Zu, F. Yang, W. Zhu, C. Wang, Z. Feng, B. Ye and Y. Xie, *J. Am. Chem. Soc.*, 2017, **139**, 3438–3445.

347 Y. Zhao, G. Chen, T. Bian, C. Zhou, G. I. N. Waterhouse, L.-Z. Wu, C.-H. Tung, L. J. Smith, D. O'Hare and T. Zhang, *Adv. Mater.*, 2015, **27**, 7824–7831.

348 P. Han, X. Yu, D. Yuan, M. Kuang, Y. Wang, A. M. Al-Enizi and G. Zheng, *J. Colloid Interface Sci.*, 2019, **534**, 332–337.

349 F. K. Meng, J. T. Li, Z. L. Hong, M. J. Zhi, A. Sakla, C. C. Xiang and N. Q. Wu, *Catal. Today*, 2013, **199**, 48.

350 F. Meng, Z. Hong, J. Arndt, M. Li, M. Zhi, F. Yang and N. Wu, *Nano Res.*, 2012, **5**, 213–221.

351 X. Yang, D. Singh and R. Ahuja, *Catalysts*, 2020, **10**, 1111.

352 A. ElMekawy, H. M. Hegab, G. Mohanakrishna, A. F. Elbaz, M. Bulut and D. Pant, *Bioresour. Technol.*, 2016, **215**, 357–370.

353 I. Ganesh, *Renewable Sustainable Energy Rev.*, 2016, **59**, 1269–1297.

354 O. S. Bushuyev, P. De Luna, C. T. Dinh, L. Tao, G. Saur, J. van de Lagemaat, S. O. Kelley and E. H. Sargent, *Joule*, 2018, **2**, 825–832.

355 M. Jouny, W. Luc and F. Jiao, *Ind. Eng. Chem. Res.*, 2018, **57**, 2165–2177.

356 C. M. Jens, L. Müller, K. Leonhard and A. Bardow, *ACS Sustainable Chem. Eng.*, 2019, **7**, 12270–12280.